

INVESTIGATION OF PIEZOELECTRIC SOFTENING MECHANISMS IN LEAD
ZIRCONATE TITANATE USING DIFFRACTION AND PROPERTY MEASUREMENTS

By

SHRUTI B. SESHADRI

A DISSERTATION PRESENTED TO THE GRADUATE SCHOOL
OF THE UNIVERSITY OF FLORIDA IN PARTIAL FULFILLMENT
OF THE REQUIREMENTS FOR THE DEGREE OF
DOCTOR OF PHILOSOPHY

UNIVERSITY OF FLORIDA

2012

© 2012 Shruti B. Seshadri

To my family

ACKNOWLEDGMENTS

I am very grateful to my adviser, Prof. Jacob Jones, for giving me the opportunity to do this work and for guiding me through my PhD. I thank Prof. Henry Hess for his guidance through my MS studies. I owe both Prof. Jones and Prof. Hess an intellectual debt for equipping me with the skills necessary to be a researcher. My approach to scientific problems is influenced by them to a great degree.

I thank my committee members, Prof. Jennifer Andrew, Prof. Henry Hess, Prof. Rolf Hummel, and Prof. Toshikazu Nishida for their support and interest in my work.

Many thanks to the wonderful people in the academic advising office: Martha McDonald, Meisha Wade, Doris Harlow and Jennifer Horton for their help.

During my PhD, I had the opportunity to collaborate with Prof. Dragan Damjanovic from the Laboratory of Ceramics, Institute of Materials, Swiss Federal Institute of Technology - EPFL, Prof. Pam Thomas from the Department of Physics, University of Warwick, Dr. Andrew Studer from the Bragg Institute, Australian Nuclear Science and Technology Organisation (ANSTO), and Prof. Juan Nino from the Department of Materials Science and Engineering, University of Florida. I thank Prof. Damjanovic for allowing me to spend three weeks doing experiments in his laboratory. I am also grateful for the patience with which he was always willing to discuss my data and ferroelectrics with me at a time when I was new to the field. I thank Prof. Thomas for the excellent, stimulating discussions on interpreting crystallographic data. I am thankful to Dr. Studer for showing me how to play with neutrons and for all the expertise he provided during the neutron diffraction experiments at ANSTO. Special thanks to Prof. Nino for giving me full access to his laboratory and above all, for never turning me away when I had questions or wanted to discuss ideas.

I am thankful to Prof. Moudgil for the excellence with which he taught the Interfacial Phenomena courses. I also thank him for the enthusiasm he showed in my work and for taking the time and effort to mentor me.

I am much obliged to Gautam Kini for encouraging me to apply to the Materials Science and Engineering program at the University of Florida and to Elena Aksel for encouraging me to join Prof. Jones' research group.

I thank the organizers of the 12th National School on Neutron and X-ray scattering for the great introduction to the powerful characterization technique of diffraction.

I wish to express my utmost gratitude to Rajnish Sinha for helpful discussions on a variety of subjects. I also thank Sonalika Goyal, Satyajit Phadke, Christopher Turner, Luping Li, Donald Moore, Hyuksu Han and Roberto Esquivel for discussions and equipment help.

I am grateful for the chance to have worked with the following undergraduate students: Michelle Nolan, Bruna Bregadiolli, Cassandra Ilano, Alexandra Henriques, Natasha Woodruff, David Lynch and Krystal Acosta. This work would not have progressed as quickly without them. Michelle also measured the temperature dependent piezoelectric coefficients shown in this work at Prof. Jürgen Rödel's laboratory in the Technische Universität Darmstadt. Special thanks to her for sticking with me from beginning to end.

For their friendship, counsel, support, knowledge and for being incredible lab mates, I thank the members of the JJones group: Abhijit, Anderson, Jenny, Goknur Dipankar, Krishna, Akito, Tedi-Marie, Sungwook, Bas, Elena, Giovanni, Brienne,

Tarielle, Jared, Chris Dosch, Lyndsey, Katherine, Clay, Michelle, Bruna, Ali, Natasha, David, Krystal, Michael, Peishi, Henry, Claudia, Daniel, Zach, Humby, Isaac, Patrick and Zhi. I especially thank Krishna for his guidance during my graduation semester, Dipankar for the discussions that made graduate school that much more awesome and Jenny for reviewing my dissertation, and help with the Rietveld refinements presented in this work.

I deeply appreciate the support of my friends. I cannot thank my family enough for always doing everything possible to encourage and support me.

I acknowledge the Bragg Institute at the Australian Nuclear Science and Technology Organisation (ANSTO) for providing neutron diffraction facilities through program proposal number PP911. Use of the Advanced Photon Source at Argonne National Laboratory was supported by the U. S. Department of Energy, Office of Science, Office of Basic Energy Sciences, under Contract No. DE-AC02-06CH11357 and DOE under contract no. W-31-109-ENG-38. I thank Dr. Yang Ren and Dr. Guy Jennings for their help with the usage of beamlines 11-ID-C and Dr. Matthew Suchomel for his help with the usage of beamline 11-BM.

I gratefully acknowledge the following funding sources: Tatachem Golden Jubilee Foundation Trust for the funds to travel to the USA from India to start graduate school; M.K.Tata Trust for the funds to cover my expenditures in the first month of graduate school; The National Science Foundation (NSF) award numbers DMR-0746902 and OISE-0755170 for the stipend and travel funds that enabled this work.

TABLE OF CONTENTS

	<u>page</u>
ACKNOWLEDGMENTS.....	4
LIST OF TABLES.....	9
LIST OF FIGURES.....	10
LIST OF ABBREVIATIONS.....	12
ABSTRACT.....	13
CHAPTER	
1 INTRODUCTION.....	15
1.1 Motivation and Problem Statement.....	15
1.2 Piezoelectricity.....	16
1.3 Dielectric Permittivity.....	17
1.4 Ferroelectricity and Ferroelectric Domain Structure.....	17
1.5 Polycrystalline Ferroelectrics.....	21
1.6 Lead Zirconate Titanate.....	22
1.7 Intrinsic and Extrinsic Contributions to the Piezoelectric Response.....	24
1.8 Morphotropic Phase Boundary and Enhanced Piezoelectric Response.....	24
1.8.1 Increased Ease of Polarization Reorientation during Poling.....	25
1.8.2 Displacement of Domain Walls and Phase Boundaries, and their Contribution to Electro-Mechanical Properties.....	26
1.8.3 Role of the Monoclinic Phase and Polarization Rotation.....	28
1.9 Hard and Soft PZT.....	29
1.10 Organization of the Dissertation.....	30
2 EXPERIMENTAL METHODS.....	39
2.1 Synthesis of PZT Based Ceramics.....	39
2.2 Temperature Dependent Dielectric Property Measurements.....	40
2.3 Temperature Dependent Piezoelectric Property Measurements.....	40
2.4 Characterization of Electric Field induced Structural Changes using High Energy X-ray Diffraction from a Synchrotron Source.....	41
2.4.1 Experimental Setup.....	41
2.4.2 Binning of Diffraction Data.....	42
2.5 Characterization of Temperature Dependent Structural Changes using High Resolution XRD from a Synchrotron Source.....	42
3 A STRUCTURAL INSIGHT INTO THE SOFTENING MECHANISMS IN LEAD ZIRCONATE TITANATE.....	49

3.1 Softening in Donor Substituted PZT.....	49
3.2 Experimental.....	50
3.2.1 Sample Preparation.....	50
3.2.2 Diffraction Measurements.....	51
3.2.3 Coercive Field and Piezoelectric Coefficient Measurements.....	52
3.3 Results.....	52
3.4 Discussion.....	56
3.4.1 90° Domain Wall Motion.....	57
3.4.2 Coexistence of mixed ferroelectric phases.....	57
3.4.3 Interphase Boundary Motion During Subcoercive Electric Field Application.....	58
3.4.4 Strain in the Rhombohedral (200) Lattice Plane.....	58
3.5 Conclusions.....	59
4 COOPERATIVE STRAIN ACCOMMODATION AND HIGH temperature PIEZOELECTRIC coefficients IN Soft DOPED PZT.....	70
4.1 High Piezoelectric Coefficients in PZT.....	70
4.2 Experimental.....	71
4.2 Variation of Piezoelectric and Dielectric Properties as a Function of Temperature in Sm, La and Nb doped PZT.....	72
4.3 Temperature Dependent Structural Changes in Sm, La and Nb doped PZT....	74
4.4 Discussion.....	76
4.5 Conclusions.....	82
5 SUMMARY.....	94
6 FUTURE WORK.....	97
6.1 Measurement of the Temperature Dependent Crystallographic Response During the In Situ Application of Electric Fields.....	97
6.2 Frequency Dependence of the Piezoelectric Response.....	97
6.3 Effect of Dopant Homogeneity.....	98
6.4 Measurements on Undoped PZT Compositions.....	98
6.5 Effect of the Ionic Radius of the Dopant on the Ferroelectric-Paraelectric Phase Transition.....	98
APPENDIX: DETERMINATION OF THE CONTRIBUTION OF 90° DOMAIN WALL MOTION TO LONGITUDINAL STRAIN.....	99
LIST OF REFERENCES.....	106
BIOGRAPHICAL SKETCH.....	114

LIST OF TABLES

<u>Table</u>		<u>page</u>
3-1	Lattice parameters, phases present and coercive fields of the various doped PZT 50:50 compositions.	62
3-2	Strain mechanisms in soft doped PZT 50:50 compositions.	63
4-1	Summary of Rietveld refinement results.	89
4-2	Ratio of the slopes of the linear fits to the left and right regions of inverse susceptibility at the point of divergence.	93

LIST OF FIGURES

<u>Figure</u>	<u>page</u>
1-3	Illustration of a) 180°, and b) 90° domains and domain wall regions in a ferroelectric tetragonal perovskite..... 33
2-1	Processing steps for $\text{PbZr}_{1-x}\text{Ti}_x\text{O}_3$ based ceramic synthesis..... 44
2-2	Schematic diagram of the measurement apparatus used to determine the <i>in situ</i> temperature dependent longitudinal relative permittivity. 45
2-4	Experimental arrangement for time-resolved high energy X-ray diffraction.. 47
2-5	Schematic of a 2D diffraction image showing the Debye-Scherrer ring as measured when a) no electric field is b) an electric field is applied to the sample..... 48
3-1	Diffraction patterns showing the (002) and (200) reflections of 2 at. % Sm, Nd, La and Nb doped PZT 50:50 before the application of an electric field..... 61
3-2	Time resolved diffraction patterns measured <i>in situ</i> during the application of the first strong bipolar electric field. 64
3-3	Time resolved diffraction patterns measured <i>in situ</i> during the application of the third strong bipolar electric field. 65
3-4	Selected region of the diffraction patterns showing the {002} type reflections of a) Sm b) Nd c) La and d) Nb doped PZT 50:50 before and after poling. 66
3-5	Time resolved diffraction patterns measured <i>in situ</i> during the application of weak subcoercive electric fields. 67
3-6	Selected region of the diffraction pattern showing the {002} type reflections for a) Sm b) Nd c) La and d) Nb doped PZT 50:50..... 68
3-7	Gaussian fits to the {002} reflections in Nb-doped PZT..... 69
4-1	Variation of d_{33} and $\epsilon_{r,33}$ as a function of temperature for various PZT compositions..... 84
4-2	Behavior of d_{33} as a function of temperature during the first, second and third thermal cycles for 2 at% Sm PZT 50:50. 85
4-3	Selected regions of high resolution synchrotron XRD patterns showing the (002) and (200) type reflections for Sm, La and Nb-doped PZT 50:50..... 86
4-4	Magnified view of the (002) and (200) tetragonal reflections of Sm, La and Nb-doped PZT 50:50 at 332°C..... 87

4-5	Rietveld refinements of 2 at % Sm-doped PZT 50:50 fit to a cubic model (332°C, 360°C, 500°C), tetragonal model (250°C, 290°C, 308°C, 332°C) and a mixed phase model consisting of the tetragonal <i>P4mm</i> and cubic <i>Pm3m</i> phases (308°C, 332°C).....	88
4-6	Variation of the dielectric loss tangent as a function of temperature for various PZT compositions.	90
4-7	Inverse dielectric susceptibility as a function of temperature for 2 at% Sm, La and Nb-doped PZT 50:50.	91
4-8	Linear fits to the a) left, and b) right linear regions at the point of divergence of inverse susceptibility plotted for 2 at% Sm, La and Nb PZT 50:50.	92
A-1	Experimentally determined and modeled values of $\Delta\eta_{002}$ as a function of α at two subcoercive electric field amplitudes.....	104
A-2	Variation of $\Delta\eta_{002}$ as a function of α for K350. The lines represent modeled values and the symbols represent experimentally measured data	105

LIST OF ABBREVIATIONS

EDS	Energy dispersive spectroscopy
LCR	Inductor, capacitor, resistor
LGD	Landau-Ginzburg-Devonshire
MPB	Morphotropic phase boundary
PZT	Lead zirconate titanate
SEM	Scanning electron microscopy
TEM	Transmission electron microscopy
XRD	X-ray diffraction
YSZ	Yttria stabilized zirconia

Abstract of Dissertation Presented to the Graduate School
of the University of Florida in Partial Fulfillment of the
Requirements for the Degree of Doctor of Philosophy

INVESTIGATION OF PIEZOELECTRIC SOFTENING MECHANISMS IN LEAD
ZIRCONATE TITANATE USING DIFFRACTION AND PROPERTY MEASUREMENTS

By

Shruti B. Seshadri

December 2012

Chair: Jacob L. Jones

Major: Materials Science and Engineering

Lead zirconate titanate (PZT) is a well-known piezoelectric ceramic of commercial and scientific importance. Typically, PZT is used in its doped form as doping allows its properties to be tailored for specific applications. Donor doping turns PZT into a "soft" ferroelectric. One of the characteristics of soft ferroelectrics is an increase in their longitudinal piezoelectric coefficient. Softening is currently attributed to an increase in the concentration of lead vacancies and the associated effect on the behavior of ferroelectric domain walls. However, the exact mechanism by which donor doping enhances the longitudinal piezoelectric coefficient is still not understood.

In this work, the crystallographic response of donor-doped PZT is studied *in situ* during the application of electric fields in order to deduce the strain mechanisms which contribute to ferroelectric softening. X-ray diffraction from a synchrotron source is employed for this investigation. It was found that the use of different donor dopants results in distinctive, characteristic strain mechanisms that soften PZT. Sm and Nd aid in the softening of PZT solely by enhancing 90° domain wall mobility. However, La and Nb doping results in a material with coexisting ferroelectric phases. It was further found

that Nb doping results in at least two additional strain mechanisms including interphase boundary motion and a large strain in the (200) rhombohedral lattice plane.

As piezoelectrics are also used in high temperature applications, the temperature dependence of the piezoelectric coefficient in soft doped PZT was also investigated. It was found that Sm doping leads to a high temperature ($\approx 300^\circ\text{C}$) piezoelectric coefficient that is substantially greater than that found in La and Nb-doped PZT. In some cases, the coefficient in Sm-doped PZT is greater than that of La and Nd-doped PZT by a factor of two. Conventionally, the largest piezoelectric coefficient values are obtained in soft doped PZT by using a Zr:Ti ratio close to the morphotropic phase boundary (MPB). It is shown that in Sm-doped PZT, enhanced high temperature piezoelectric coefficients can also be obtained at compositions far from the MPB due to the presence of a mixed tetragonal and cubic phase. The mixed phase is hypothesized to enable a larger extrinsic piezoelectric response in Sm doped PZT due to enhanced strain accommodation in the coexisting polymorphic phases.

In summary, it is presented that dopants yield signature, qualitative softening mechanisms, contributing differently to high piezoelectricity in PZT. The results suggest that in contrast to prior-held assumptions, an increase in Pb vacancies is not a necessary criterion for softening.

CHAPTER 1 INTRODUCTION

1.1 Motivation and Problem Statement

PZT is a piezoelectric material of commercial and scientific interest as it has very high piezoelectric coefficients. These high piezoelectric properties are obtained by the addition of soft dopants to PZT. Even though the widespread commercial application of soft doped PZT has made it one of the most studied ferroelectric systems, the mechanism by which softening occurs in PZT is not understood. This is because changes in the lattice and domain response of PZT due to the addition of soft dopants have not been measured *in situ* during the application of electric fields. Therefore, the first objective of this work is to use X-ray diffraction from a synchrotron source to study the crystallographic structure of various soft doped PZT compositions. In addition, the structural response of these compositions during the *in situ* application of electric fields is measured. The response of the various compositions is compared. From these experimental studies, the structural origin of softening mechanisms in PZT is deduced.

The piezoelectric coefficient of soft PZT is temperature dependent.¹ The second objective of this work is to establish temperature dependent structure-property relationships for select soft doped PZT materials. High resolution XRD from a synchrotron source is used for the structural studies. These studies are carried out across a range of Zr:Ti ratios in order to separate the MPB effects from other possible variables. Temperature dependent piezoelectric and dielectric properties are measured from room temperature to above the Curie temperature. This analysis also provides information regarding the dopant dependent paraelectric-ferroelectric phase transition characteristics in PZT.

1.2 Piezoelectricity

Piezoelectricity is a materials property, wherein the electric charge developed on the surface of the material is linearly coupled to the mechanical stress applied on it (Eq. 1-1).² Conversely, an applied electric field produces a linearly proportional strain in these materials (Eq. 1-2). Piezoelectric materials thus convert electrical energy into mechanical energy and vice versa.

$$D_i = d_{ijk} T_{jk} \quad (1-1)$$

$$S_{jk} = d'_{ijk} E_i \quad (1-2)$$

In Eq. 1-1 and 1-2, D_i is the electric displacement (Cm^{-2}) vector, E_i is the electric field vector (Vm^{-1}), S_{ij} is the strain tensor, T_{ij} is the stress tensor (Nm^{-2}) and d_{ijk} and d'_{ijk} are the piezoelectric charge or strain coefficient tensors. d_{ijk} and d'_{ijk} are third rank tensors and the components of this tensor are referred to as the piezoelectric coefficients. The units for these coefficients are CN^{-1} and mV^{-1} respectively. Thermodynamic considerations show that $d_{ijk} = d'_{ijk}$, namely the coefficient that connects the field and strain is equal to the one that connects stress and polarization. The electrical response to mechanical stimulation is the direct piezoelectric effect (Eq. 1-1) and the mechanical response to electrical stimulation is referred to as the converse piezoelectric effect (Eq. 1-2).

A non-centrosymmetric crystal structure is a necessary criterion for expression of piezoelectricity. Lead zirconate titanate ($\text{PbZr}_{1-x}\text{Ti}_x\text{O}_3$ or PZT), the material investigated in this dissertation, is an example of an inorganic piezoelectric material.

1.3 Dielectric Permittivity

Dielectric permittivity^{2,3,4} is a measure of the ability of a material to be polarized by an electric field. The polarization P_i (Cm^{-2}) that is induced in an insulating polarizable material (a dielectric) by an applied electric field vector E_j (Vm^{-1}) is given by:

$$P_i = \chi_{ij} E_j \quad (1-3)$$

χ_{ij} (Fm^{-1}) is a second rank tensor known as dielectric susceptibility of a material.

Relation 1-3 is valid only for linear materials or in the linear range for nonlinear materials. The total surface charge density that is induced in the material by the applied field is given by the dielectric displacement vector, D_i (Cm^{-2}):

$$D_i = \epsilon_0 E_i + P_i \quad (1-4)$$

ϵ_0 is a scalar quantity that equals $8.854 \times 10^{-12} \text{ Fm}^{-1}$. It is the dielectric permittivity of a vacuum. Eq. 1-4 can also be presented as:

$$D_i = \epsilon_{ij} E_j \quad (1-5)$$

where ϵ_{ij} is the dielectric permittivity of the material. The relative dielectric permittivity, or the dielectric constant, $\epsilon_{r,ij}$, is:

$$\epsilon_{r,ij} = \frac{\epsilon_{ij}}{\epsilon_0} \quad (1-6)$$

1.4 Ferroelectricity and Ferroelectric Domain Structure

Some piezoelectric materials, such as PZT, are ferroelectric in nature. This means that each unit cell of the material has a spontaneous polarization or dipole moment. The direction of the polar axis in ferroelectric materials can be reversed by the application of an electric field. The new direction of the polar axis is maintained upon the removal of the field.

PZT, like many other ferroelectric materials, transforms into a ferroelectric state from a high temperature paraelectric (non-polar) phase. Upon cooling, PZT undergoes a phase transition into a polar structure. The temperature at which this phase transition occurs is called the Curie temperature. The phase transition occurs by a small displacement of some ions from their centrosymmetric positions or by some other ordering process that creates a net dipole moment. Near the Curie temperature, the crystalline lattice is dielectrically compliant and can be polarized strongly by small electric fields. Therefore, the permittivity of PZT reaches a maximum at the Curie temperature as illustrated in Figure 1-1. This dielectric compliance of the lattice around the Curie temperature makes dielectric properties temperature dependent across a large span of temperatures. This is one reason why other materials properties such as the piezoelectric coefficient can also be temperature dependent.

The spontaneous polarization in a ferroelectric crystal is usually not aligned along the same direction throughout the entire crystal. PZT adopts the perovskite crystal structure as shown in Figure 1-2. PZT with a Zr:Ti ratio of 52:48, i.e. $\text{PbZr}_{0.52}\text{Ti}_{0.48}\text{O}_3$, transforms from a non-ferroelectric (paraelectric) cubic phase to a ferroelectric tetragonal phase at its Curie temperature of 386°C .⁵ Perovskite crystals have the general formula ABO_3 where the valence of the A-site and B-site cations can vary from +1 to +3 and +3 to +6 respectively. As shown in Figure 1-2, the perovskite structure may be viewed as consisting of a BO_6 octahedra surrounded by A cations. Most of the ferroelectric materials that are of practical application have perovskite structures and many are solid solutions of lead titanate, PbTiO_3 and lead zirconate, PbZrO_3 . The spontaneous polarization direction in tetragonal PZT lies along the c_T -axis of the

tetragonal unit cell and the crystal distortion is usually described in terms of shifts of the O and Ti ions relative to Pb.^{4,6,7} In the ferroelectric phase, the crystal is spontaneously strained with $a_T \leq a_C < c_T$ where a_T and a_C are the a-axes of the tetragonal and cubic unit cell, respectively.

The six directions (including positive and negative orientations) along the three a_C -axes of the cubic unit cell are equivalent. When the crystal is cooled through the Curie temperature, the probability that the spontaneous polarization may arise along any one of the a_C -axes directions is equal. The direction along which the polarization will develop depends on the local and global electrical and mechanical boundary conditions imposed on the material. Once these domains are formed, regions of the crystal with uniformly oriented spontaneous polarization directions are called ferroelectric domains. The region between two domains is the domain wall as illustrated in Figure 1-3. The walls which separate domains with oppositely oriented polarization directions are called 180° walls and those which separate regions with mutually perpendicular polarization directions are called 90° walls (Figure 1-3).^{4,7}

The driving force for the formation of 180° domain walls is the depolarizing field (E_d) that arises due to the onset of the spontaneous polarization (P_S) at the Curie temperature.⁸ E_d oriented in the opposite direction to P_S as shown in Figure 1-4. E_d develops whenever there is a non-homogenous distribution of P_S . Non-homogenous distribution of P_S can occur due to a reduction in the polarization near the surface of the ferroelectric (polarization is zero surrounding the ferroelectric material and non-zero within) or due to a change in the direction of polarization at grain boundaries. E_d may be very strong (of the order of MVm^{-1}) rendering the single domain state of the ferroelectric

unfavorable.^{4,7,8} The electrostatic energy associated with the depolarizing field may be minimized if i) the ferroelectric splits into domains with oppositely oriented polarization (Figure 1-4), or ii) the depolarizing charge is compensated for by electrical conduction through the crystal or by charges from the material surrounding (such as from the atmosphere or the electric circuit to which the material is connected). As shown in Figure 1-4 the PZT splits into 90° domains due to the influence of mechanical stresses when a part of its crystal is mechanically compressed along the (100) cubic direction as it is cooled through the Curie temperature. To minimize the elastic energy, the long c_T -axis of the tetragonal cell will develop perpendicular to the stress. In the unstressed section of the crystal, polarization may remain parallel to the direction of the stress (short a_T -axis perpendicular to the stress). The domain walls in PZT may therefore separate regions in which polarization orientation is antiparallel (180° walls) or perpendicular (90° walls) to each other.

Both 90° and 180° walls may reduce the effects of depolarizing electric fields. However, only the formation of 90° walls minimizes the elastic energy. A combination of electric and elastic boundary conditions to which a crystal is subjected as it is cooled through the ferroelectric phase transition temperature usually leads to a complex domain structure with many 90° and 180° walls.

Domain walls which differ in orientation to the spontaneous polarization vector are called ferroelectric domain walls and those which differ in orientation to the spontaneous strain are called ferroelastic domain walls. In PZT, 180° walls are purely ferroelectric because they differ only in the orientation of the polarization vector. 90°

walls are both ferroelectric and ferroelastic as they differ both in orientation of the polarization vector and the spontaneous strain.

The types of domain walls that can occur in a ferroelectric crystal depend on the symmetry of both the non-ferroelectric and ferroelectric phases of the crystal.⁹ In the rhombohedral phase of PZT, the direction of the polarization develops along the body diagonals ($\langle 111 \rangle$ direction) of the paraelectric cubic unit cell. This allows 8 possible directions of the spontaneous polarization with 180° , 71° and 109° domain walls. Criteria which may be used to derive possible types of domain walls in a ferroelectric material have been derived by Fousek and Janovec.⁹ Observations made using transmission electron microscopy show that domain walls are on the order of 1–10 nm.⁸

1.5 Polycrystalline Ferroelectrics

Due to the complex set of elastic and electric boundary conditions at each grain, ferroelectric grains in polycrystalline ceramics are always split into many domains as shown in Figure 1-5. If the direction of the spontaneous polarization throughout the material is random or distributed in such a way as to lead to zero net polarization, the piezoelectric effects of individual domains will cancel and this material is not piezoelectric at the macroscopic length scale. Polycrystalline ferroelectric materials may be brought into a polar state by applying a strong electric field ($1\text{--}10 \text{ kV mm}^{-1}$) often at elevated temperatures. This process, termed poling, cannot orient grains but can reorient domains within individual grains in the direction of the applied field. A poled polycrystalline ferroelectric exhibits piezoelectric properties, even if many domain walls remain (Figure 1-5).

The measured polarization after the removal of the field (at zero field) is called remnant polarization, P_R . The maximum remnant polarization, $(P_R)_{\text{max}}$, achievable in a

polycrystalline material depends on the available domain states. In a ferroelectric which exhibits only 180° domain walls the maximum remnant polarization in the polycrystalline state is $0.25 P_S$. In a tetragonal ferroelectric with 6 available domain states $(P_R)_{\max} = 0.83 P_S$. In a rhombohedral ferroelectric with 8 possible domain states, $(P_R)_{\max} = 0.87 P_S$. In an orthorhombic ferroelectric with 12 possible domain states, $(P_R)_{\max} = 0.91 P_S$.¹⁰ These ideal values assume reorientation of all domains along available directions dictated by the poling field. The actual polarization is in fact always lower, as many domains cannot be reoriented due to a complex set of internal stresses and electric fields in grains and because some domains switch back after the poling field is removed. In materials with non- 180° domain walls, the poling process changes the sample dimensions, because reorientation of non- 180° domains involves reorientation of the spontaneous strain (see Figures 1-3 and 1-4).

1.6 Lead Zirconate Titanate

Lead zirconate, $PbZrO_3$, is antiferroelectric (and not piezoelectric).⁸ Lead titanate ($PbTiO_3$) is of limited interest as a piezoelectric material since it is difficult to pole and has a large thermal expansion anisotropy of the tetragonal phase which causes mechanical fracture during cooling from the sintering temperature.¹¹ However, the solid solution of these two compositions, lead zirconate titanate, $Pb(Zr_{1-x}Ti_x)O_3$ or PZT, exhibits outstanding piezoelectric properties. Its widespread use in industry, science, medicine, transportation, communications and information technologies has also made PZT one of the most studied ferroelectrics.^{11,12,13,14} Despite this, many aspects of the high piezoelectric response in PZT remain unclear. Perhaps nothing attests better to the complex nature of PZT than the fact that approximately 60 years after its discovery (Shirane et al. 1952¹⁵) and numerous in depth studies (e.g. Jaffe et al. 1971¹⁶),

modifications of the composition-temperature phase diagram of this ternary system are still being proposed (Noheda et al. 1999¹⁷). In fact, newer questions are still being raised about the origins of the large piezoelectric response in this and related ferroelectric materials.¹⁸

Lead zirconate and lead titanate are mutually soluble in all proportions. The first phase diagram of $\text{Pb}(\text{Zr}_{1-x}\text{Ti}_x)\text{O}_3$ was derived by Sawaguchi¹⁹ in 1953 showing the most prominent feature of the system, the compositionally-driven structural transformation from the tetragonal ($P4mm$) to the rhombohedral phase ($R3m$) at $x \approx 0.47$ at room temperature. This work was followed by the discovery of a large piezoelectric response in compositions close to this phase boundary by Jaffe et al.²⁰ in 1954.

The composition-temperature phase diagram of Sawaguchi was refined by Jaffe and coworkers in 1971.¹⁶ A significant modification of the Jaffe et al. phase diagram was proposed by Noheda et al.¹⁷ They proposed that a monoclinic phase separates the tetragonal and rhombohedral regions. The nature of this phase is still a subject of debate and much study. The phase diagram proposed by Jaffe et al. with the modification made by Noheda et al. are shown in Figure 1-6.

In this work, PZT compositions are abbreviated by 100(1-x):100x PZT where 100(1-x):100x indicates in percent the Zr:Ti ratio in the solid solution. Zr and Ti are randomly distributed over B-sites of the perovskite structure ABO_3 (see Figure 1-2). For example, PZT 50:50 is used to denote a PZT composition with the chemical formula $\text{PbZr}_{0.5}\text{Ti}_{0.5}\text{O}_3$.

1.7 Intrinsic and Extrinsic Contributions to the Piezoelectric Response

The piezoelectric properties of polycrystalline ferroelectric ceramics are generally dependent on both intrinsic and extrinsic mechanisms.⁵ Intrinsic contributions are the result of lattice strain due to the displacement of the cations. Changes in polarization of the unit cell are accompanied by a change in the unit-cell volume. Intrinsic contributions in typical PZT compositions total less than 50% at room temperature.²¹ The remaining contributions to the piezoelectric effect are extrinsic in nature and arise due to domain wall displacement, defect dipoles, interphase boundary motion, and intergranular interactions.²² Extrinsic mechanisms are thermally activated processes that can be frozen out at low temperatures.²¹ Figure 1-7 shows the intrinsic and extrinsic mechanisms that contribute to the piezoelectric coefficient.

1.8 Morphotropic Phase Boundary and Enhanced Piezoelectric Response

A striking feature of the PZT phase diagram is the nearly temperature-independent boundary between tetragonal and rhombohedral (monoclinic) phases, called the “morphotropic phase boundary” (MPB). The term was used by Jaffe et al. to designate “an abrupt structural change within a solid solution with variation in composition” (p. 135, Jaffe et al. 1971¹⁶). The composition of the MPB is approximately PZT 52:48 at room temperature.

The MPB is considered the most interesting composition from the technological application point-of-view as the piezoelectric coefficients, electromechanical coupling coefficients, dielectric permittivity and remnant polarization measured on ceramic samples reach a peak in the region of the MPB (Figure 1-8).

The origin of the enhanced dielectric, elastic, and piezoelectric properties of PZT at the MPB has been investigated in detail by many authors and is still a topic of avid

interest.²³ Several mechanisms have been proposed to explain the enhanced piezoelectric properties of PZT at the MPB. Presently, there is no consensus in literature on this problem. The disagreement could be a mere question of the quality of samples examined by different authors but also a consequence of the scale on which the material is examined. Recent studies²⁴ suggest that local tetragonal and rhombohedral nanostructure of PZT in the MPB region may appear to X-ray diffraction as monoclinic. It is suggested that the high properties in the MPB region are then at least in part related to the high mobility of these nanodomains. The facilitated rotation of polarization (as evidenced by high transverse permittivity) is accomplished through easy reorientation of the nanodomains. Sections 1.8.1-1.8.3 outline the main points of the different proposed mechanisms.¹⁸

1.8.1 Increased Ease of Polarization Reorientation during Poling

The tetragonal phase has 6 possible orientations of polarization (along the pseudo-cubic $\langle 100 \rangle$ directions), while in the rhombohedral phase, polarization can orient along 8 possible $\langle 111 \rangle$ directions. At the MPB, the tetragonal and rhombohedral phases can coexist²³ because the free energy barrier between them are very low and switching between the phases can be accomplished by external fields (e.g., by a poling field). Therefore, in effect, polarization within each grain of a tetragonal and rhombohedral mixed phase material has effectively 14 directions along which it can orient. Better poling results in larger piezoelectric properties.^{16,23} It has been shown experimentally that remnant polarization in PZT has a maximum near the MPB.¹⁶ Recent results suggest that the MPB region contains a monoclinic phase.¹⁷ If this is the case, the number of available orientations for polarization would be further increased as polarization can adopt 24 orientations in a monoclinic phase.

1.8.2 Displacement of Domain Walls and Phase Boundaries, and their Contribution to Electro-Mechanical Properties

Displacement of domain walls and phase boundaries and their resulting contribution to the electro-mechanical properties is enhanced at the MPB.^{10,23} This argument is related to that presented in Section 1.8.1 but, here specifically relates to operation under subcoercive electric fields. With multiple domain states available in the MPB region, the energy barrier between different states should be relatively small, facilitating displacement of domain walls even by relatively weak driving fields. Similarly, the boundary between crystalline phases with degenerate energies should be easily displaced. It is known that displacement of domain walls can greatly enhance the piezoelectric and dielectric properties of ferroelectric ceramics.²⁵ Experimental results clearly show that domain wall contributions in PZT indeed increase as the MPB is approached.²⁶ Jones et al.²⁷ have shown that the displacement of phase boundaries participate in the enhanced response.

Intrinsic properties of PZT crystals at the MPB region are high. Due to the historical unavailability of PZT single crystals of MPB composition, information on the intrinsic (lattice) properties of PZT is almost exclusively available through theoretical calculations, based on the phenomenological Landau-Ginzburg-Devonshire (LGD) approach,²⁸ and more recently, ab-initio calculations.^{29,30} Using a thermodynamics based LGD approach, it was shown qualitatively that the dielectric permittivity perpendicular to the polarization direction (transverse permittivity) diverges as the MPB is approached from both the tetragonal and rhombohedral sides, while the permittivity along the polar axis (longitudinal permittivity) exhibits a comparatively weaker divergence.³¹ The reason that the transverse permittivity diverges as the tetragonal-

rhombohedral phase transition is approached can be understood intuitively in the following way: in the tetragonal phase, polarization is oriented along the [001] pseudo-cubic direction, while in the rhombohedral phase it develops along the [111] pseudo-cubic axis. In the phase transition region, the crystal dielectrically softens along directions dictated by the symmetry of the incipient crystal structure.³² Thus, on the tetragonal side of the MPB, the crystal dielectrically softens in such a way as to anticipate the new direction of the polarization along the [111] pseudo-cubic axis in the rhombohedral phase. This means that the longitudinal permittivity will increase much more than the transverse permittivity. A similar effect will occur on the rhombohedral side.

This result was confirmed in a quantitative study,²⁸ and later extended³³ to derive general conditions for the appearance of an MPB. The maximum in piezoelectric properties is thus a direct consequence of the anomaly in the permittivity. Since divergence at the MPB is stronger for the transverse than for the longitudinal component of the permittivity, the shear piezoelectric coefficient will be enhanced more strongly in all phases than the longitudinal coefficient.²⁸ This means that the propensity of crystals for polarization rotation is enhanced at the MPB. The anomalous behavior of monodomain single crystals at the MPB is reflected in ceramics through averaging of the properties over all grains and domain orientations. The ceramic samples thus exhibit a maximum of the properties at MPB, which are essentially the intrinsic, single crystal properties. Improved poling of ceramics at the MPB and facilitated domain wall displacement in ceramics add to this intrinsic mechanism. However, internal stresses in

ceramics, interactions among grains and domains, and local texture affect the overall intrinsic as well as extrinsic response of ceramics and should not be neglected.^{34,35}

1.8.3 Role of the Monoclinic Phase and Polarization Rotation

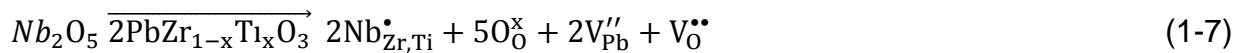
After the proposal of the monoclinic phase in PZT,¹⁷ many attempts have been made to explain MPB behavior in PZT and other ferroelectrics by enhanced piezoelectric response within this phase. It was indicated in the previous sections that the propensity of PZT crystals for polarization rotation is augmented as the MPB is approached. The field induced polarization rotation is thought to take place within the monoclinic mirror planes (Davis et al. 2006; Fu and Cohen 2000).^{36,37} It is believed that if the monoclinic phase indeed exists, it facilitates the polarization rotation and hence produces a high dielectric and piezoelectric response. However, it should be noted that the propensity of a crystal for polarization rotation is determined not by the crystal structure itself but by the value of the transverse permittivity (see section 1.7.2). Thus, LGD calculations which include the monoclinic phase suggest that property enhancement is largest at the boundary between monoclinic and tetragonal or monoclinic and rhombohedral phases, not within the monoclinic phase itself.³⁸ This also agrees with results of phenomenological simulations.³⁹ The enhancement of the properties associated with the presence of a monoclinic phase is thus likely related to pre-transitional phenomena. One such example of pre-transitional phenomena is Curie-Weiss behavior of permittivity in the cubic phase of ferroelectric material. If polarization changes direction at the MPB (e.g., tetragonal-rhombohedral), the transverse permittivity will increase in both phases around the MPB and enhance propensity of the material for polarization rotation. However, the mechanisms of enhancement of

properties via divergence of the transverse permittivity are not qualitatively different, irrespective of the presence of a monoclinic phase.⁴⁰

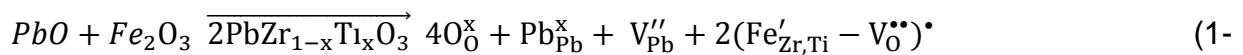
1.9 Hard and Soft PZT

In ceramic processing terminology, chemical substituents of concentrations less than 5 atomic % are referred to as "dopants".^{11,41} This terminology is adopted throughout this dissertation.

PZT ceramics are rarely used in their undoped state. Commercially available samples are synthesized with chemical additives to adjust their properties for specific applications. It was discovered that addition of donor dopants leads to materials with increased resistivity, decreased ageing, higher piezoelectric coefficients, higher losses, lower mechanical quality factor, and low coercive field; these materials are known as "soft".¹⁶ Typical donor or soft dopants are Nb⁺⁵ substituting for the B-site (denoted as Nb'_{Ti} or Nb'_{Zr} in the Kröger-Vink notation) or La⁺³ substituting for the A-site (La'_{Pb}). A plausible charge compensation scheme due to the introduction of the aliovalent soft dopant Nb, is shown in Eq. 1-7.



The addition of acceptor dopants leads to materials with lower permittivity, lower dielectric loss, lower resistivity, high mechanical quality factor, and more difficult poling and depoling.¹⁶ They are known as "hard" materials. A typical hard dopant for PZT is Fe⁺² substituting for the B-site (Fe''_{Ti} or Fe''_{Zr}). A plausible charge compensation scheme due to the introduction of the aliovalent hard dopant Fe is shown in Eq. 1-8.



8)

The mechanisms of hardening are relatively well understood,^{31,42} while many interpretations of softening are not well understood.^{10,43}

1.10 Organization of the Dissertation

Chapter 2 provides a detailed description of the experimental methods used in this dissertation. The conditions used for the solid state processing of bulk PZT ceramics are given. The measurement of temperature dependent dielectric and piezoelectric properties and the methodology used for structural characterization using high resolution and high energy XRD from a synchrotron source are also described.

In Chapter 3, the structural changes that occur in four donor doped PZT compositions are examined *in situ* during the application of both large and subcoercive electric fields. High energy X-rays from a synchrotron source are used for this purpose. These studies provide insight into the softening mechanisms in donor doped PZT.

In Chapter 4, the temperature dependent piezoelectric and dielectric response of various donor doped PZT compositions are studied. The temperature dependent structural changes that occur in these materials are also measured using high resolution XRD from a synchrotron source. These measurements are used to provide an explanation for the origin of the anomalously high piezoelectric coefficient values shown in some compositions.

Chapter 5 provides a summary of the dissertation.

Chapter 6 proposes future work that can be carried out in the investigation of strain mechanisms that contribute towards softening.

Appendix A presents method to calculate the contribution of 90° domain wall motion to longitudinal strain using a time-resolved diffraction pattern taken at only one angle (parallel to the electric field) with respect to the electric field.

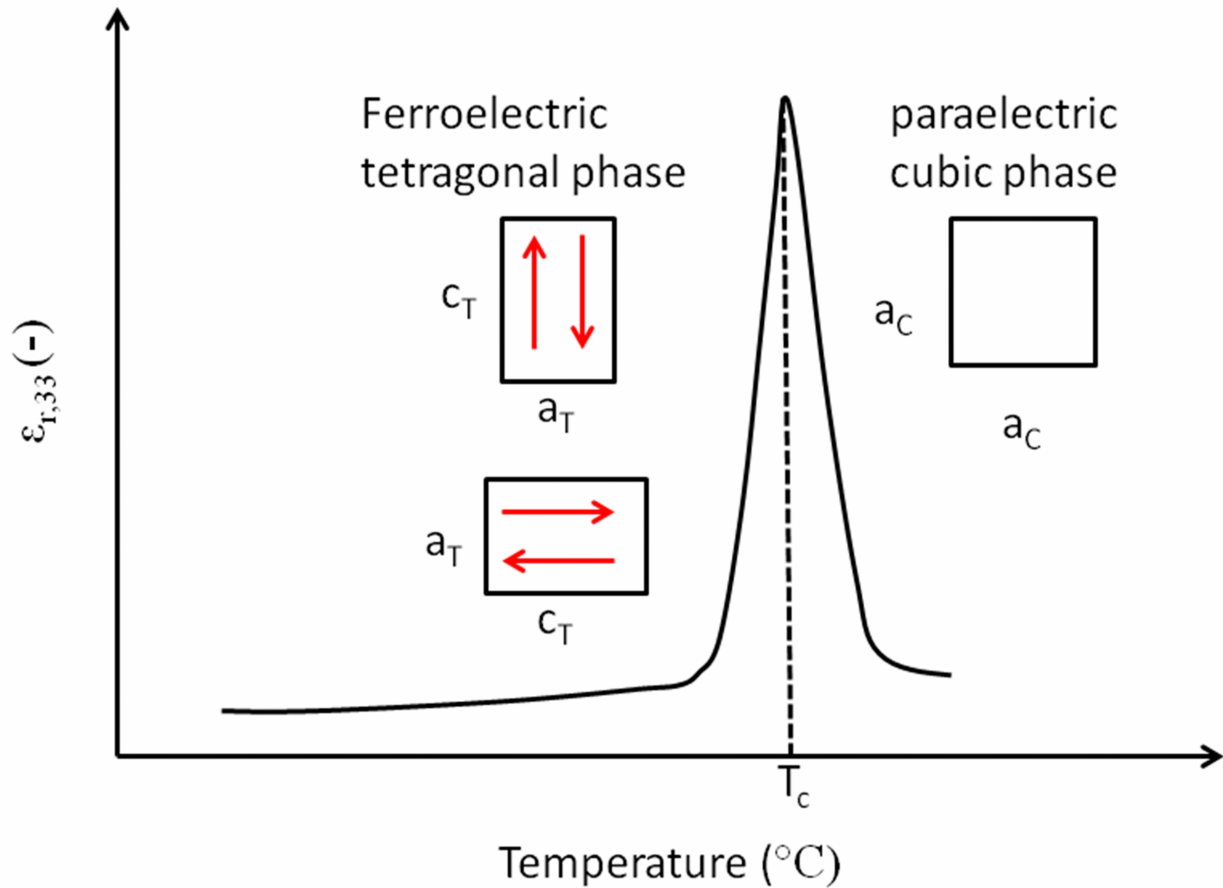


Figure 1-1. Schematic diagram showing the changes in permittivity that occur in a ferroelectric material with temperature. The permittivity curve represents data measured in a PZT ceramic. The arrows show the possible directions of spontaneous polarization (in two dimensions). The unit cell is represented by a square in the cubic phase, and a rectangle in the tetragonal phase. Adapted without permission from D. Damjanovic, "Ferroelectric, Dielectric and Piezoelectric Properties of Ferroelectric Thin Films and Ceramics," (Page 1279, Figure 3) *Rep. Prog. Phys.*, **61** [9] 1267-324 (1998).

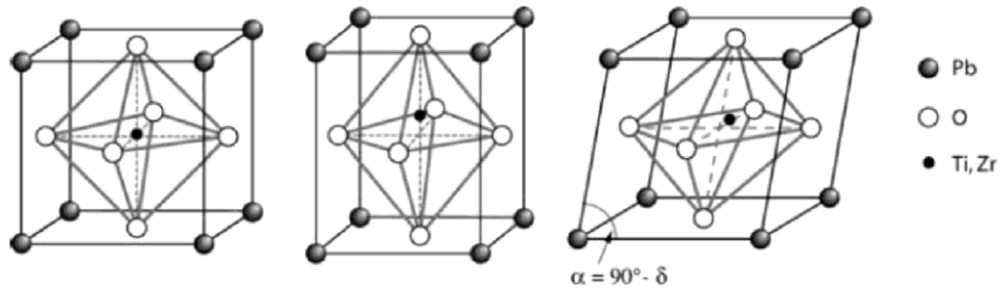


Figure 1-2. The perovskite crystal structure of PZT in its paraelectric cubic (left), ferroelectric tetragonal (center) and rhombohedral (right) states. The ferroelectric state of PZT adopts a rhombohedral crystal structure when less than approximately 47% of the B-site is occupied by Ti. When greater than 47% of the B-site atoms are occupied by Ti, PZT adopts a tetragonal crystal structure in its ferroelectric state. Reprinted without permission from G. Bertotti and I. D. Mayergoyz, *The Science of Hysteresis*. (Page 346 Figure 4.4) Academic Press, Oxford, UK, 2006.

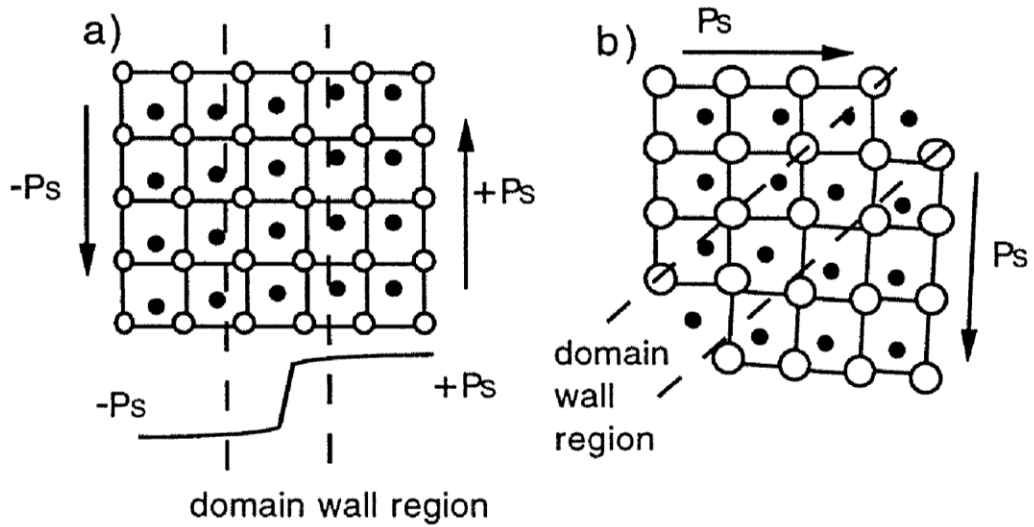


Figure 1-3. Illustration of a) 180° , and b) 90° domains and domain wall regions in a ferroelectric tetragonal perovskite. The schematic changes in polarization across the domain wall are shown for a 180° wall in a). The tetragonal distortion in b) is exaggerated. Reprinted without permission from D. Damjanovic, "Ferroelectric, Dielectric and Piezoelectric Properties of Ferroelectric Thin Films and Ceramics," (Page 1281, Figure 5) Rep. Prog. Phys., 61 [9] 1267-324 (1998).

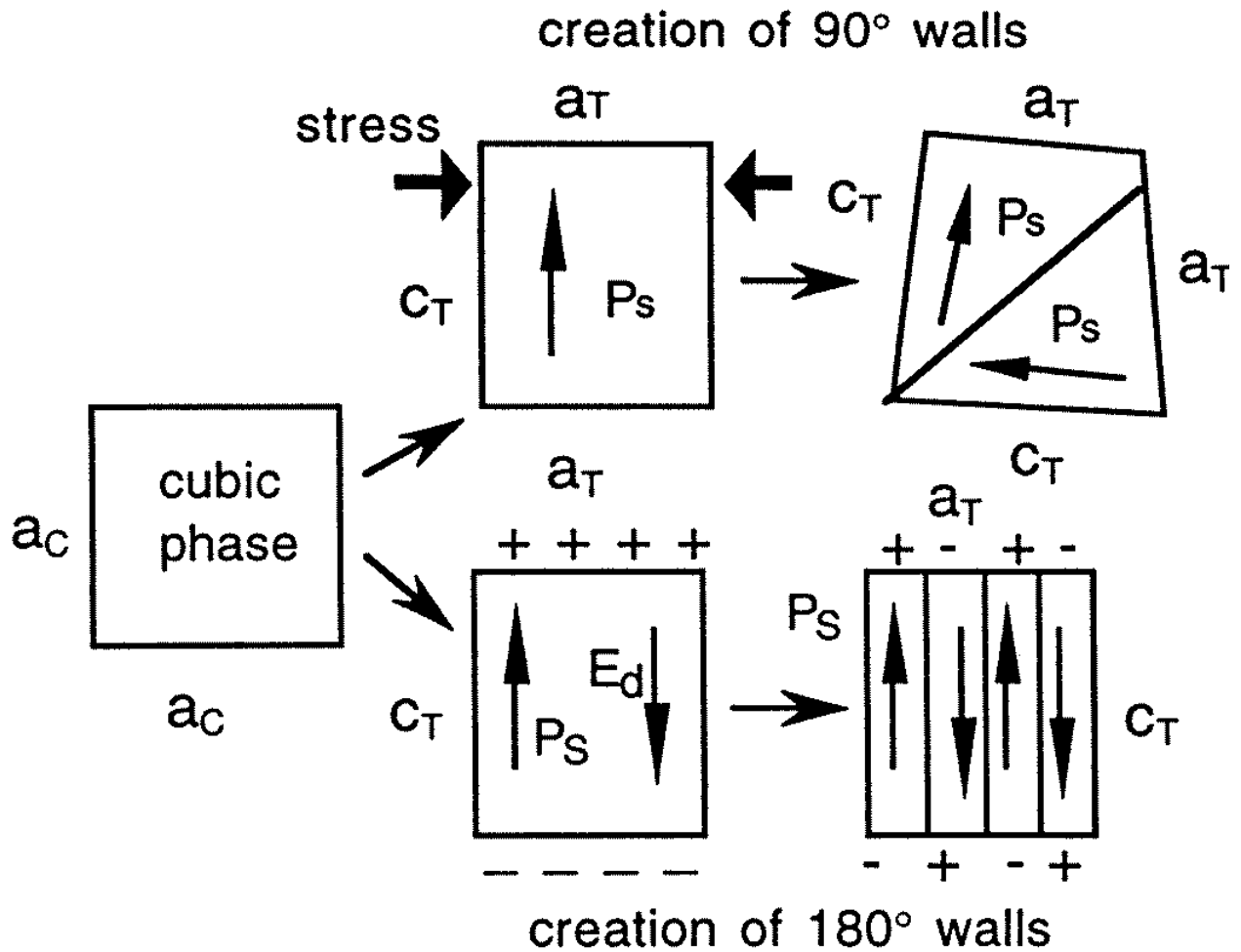


Figure 1-4. Schematic illustrating the formation of 180° and 90° ferroelectric domain walls in a ferroelectric tetragonal perovskite such as PZT. The deformation of the crystal in the domain wall region due to the formation of 90° walls is exaggerated for the sake of clarity. Symbols are explained in the text. Reprinted without permission from N. Setter, *ABC of Piezoelectricity*. (Page 5, Figure 1.1) EPFL, Lausanne, Switzerland, 2002.

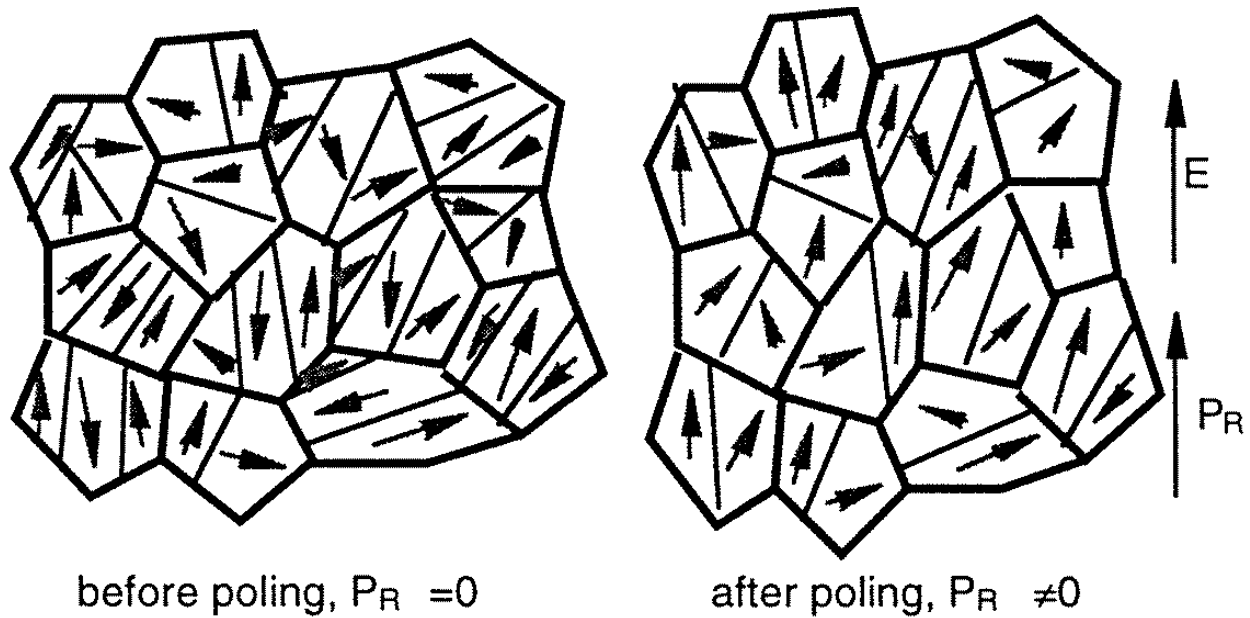


Figure 1-5. A polycrystalline ferroelectric with random orientation of grains before and after poling (reprinted from Cross). Many domain walls are present in the poled material, however the net remnant polarization is nonzero. Reprinted without permission from D. Damjanovic, "Ferroelectric, Dielectric and Piezoelectric Properties of Ferroelectric Thin Films and Ceramics," (Page 1283, Figure 7) *Rep. Prog. Phys.*, **61** [9] 1267-324 (1998).

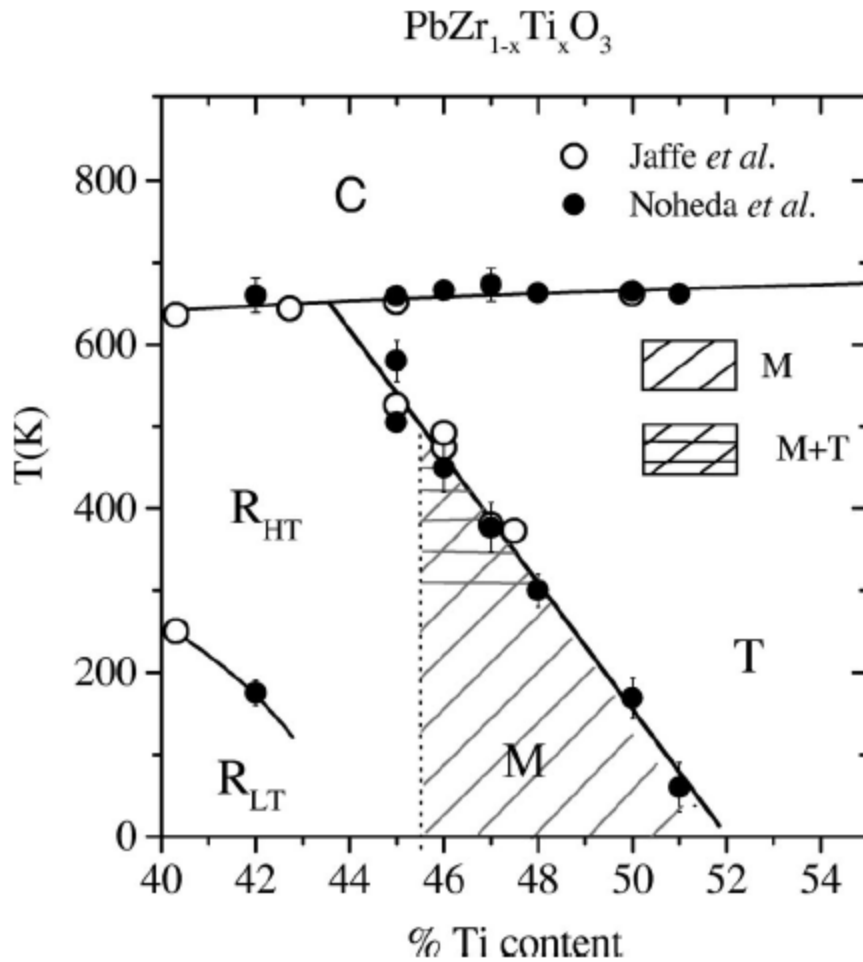


Figure 1-6. Revised PZT phase diagram proposed by Noheda et al. Data from Jaffe et al. are represented by open circles. The monoclinic region is shaded with diagonal lines. Horizontal lines are superimposed in the region of tetragonal-monoclinic phase coexistence. For $x = 0.45$, the solid symbols represent the limits of the tetragonal-rhombohedral coexistence region. Reprinted without permission from B. Noheda, D. E. Cox, G. Shirane, R. Guo, B. Jones, and L. E. Cross, "Stability of the Monoclinic Phase in the Ferroelectric Perovskite $\text{PbZr}_{1-x}\text{Ti}_x\text{O}_3$," (Page 014103-7, Figure 6) *Phys. Rev. B*, **63** [1] 014103 (2000).

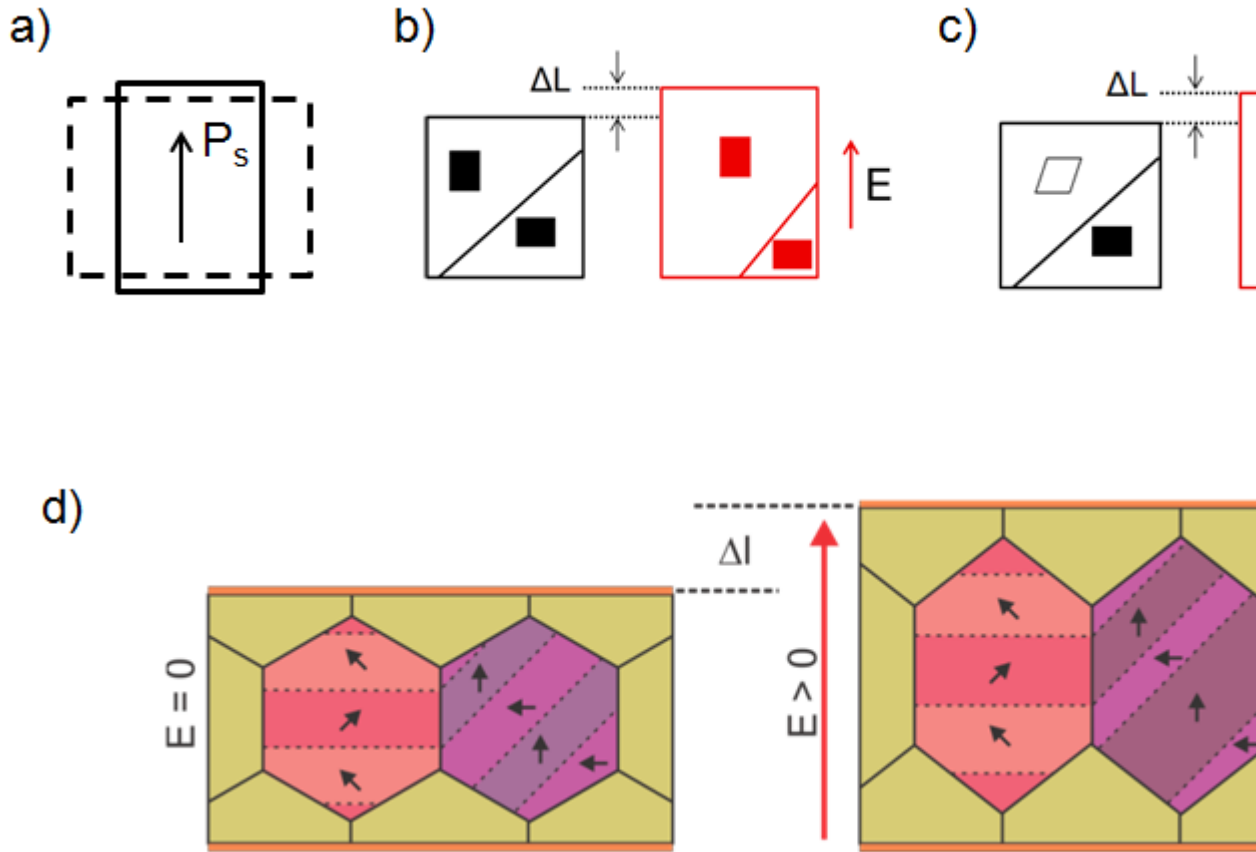


Figure 1-7. (a) Intrinsic contributions due to lattice strain and extrinsic contributions from (b) the motion of 180° domain walls, (c) the motion of a 90° domain wall (c) interphase boundary motion and (d) intergranular interaction during the application of an electric field E . The dashed lines represent the configurations before the application of the external electric field. (d) is reprinted without permission from A. Pramanick, D. Damjanovic, J. E. Daniels, J. C. Nino, and J. L. Jones, "Origins of Electro-Mechanical Coupling in Polycrystalline Ferroelectrics during Subcoercive Electrical Loading," (Page 295 Figure 1) *J. Am. Ceram. Soc.*, **94** [2] 293-309 (2011).

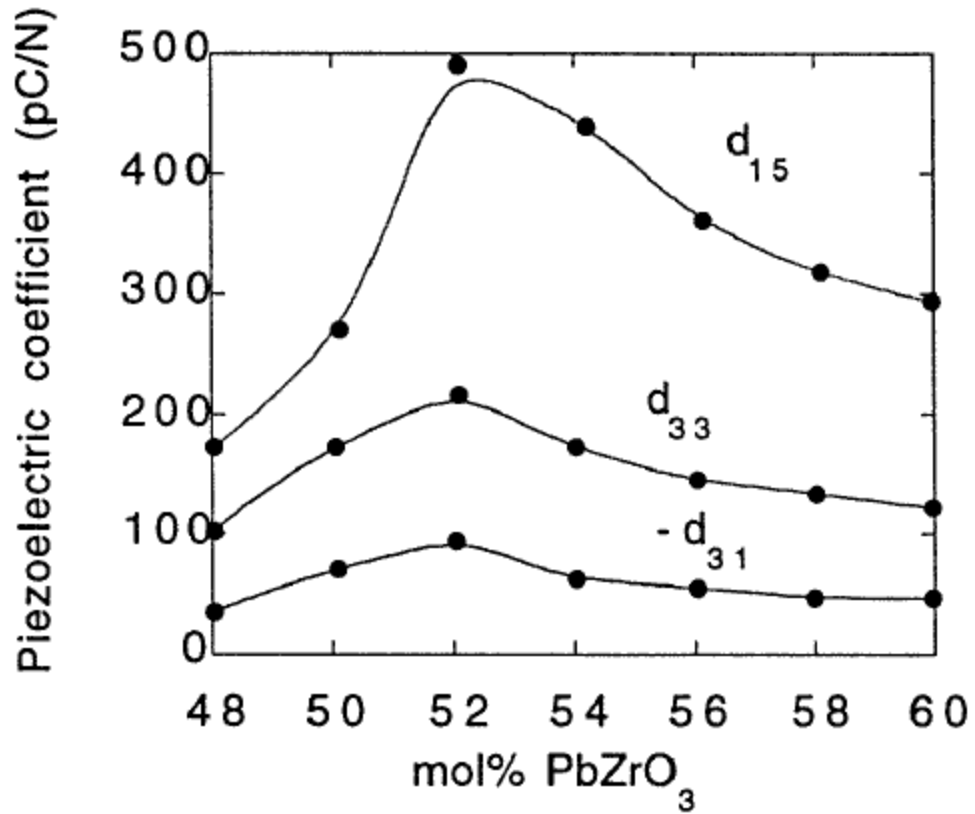
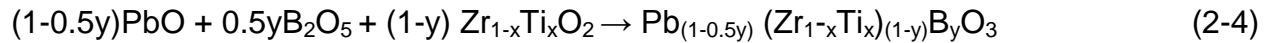
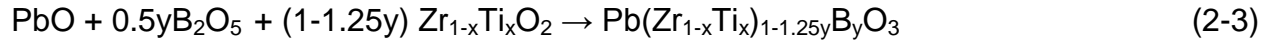


Figure 1-8. Piezoelectric coefficients of PZT ceramics as a function of composition in the vicinity of the morphotropic phase boundary. Reprinted without permission from B. Jaffe, W. Cook, and H. Jaffe, *Piezoelectric Ceramics*. (Page 143 Figure 7.9 (b)) Academic Press, San Diego, USA, 1971.

CHAPTER 2
EXPERIMENTAL METHODS

2.1 Synthesis of PZT Based Ceramics

Polycrystalline $\text{PbZr}_{1-x}\text{Ti}_x\text{O}_3$ ceramics are used in the present work. The ceramics were synthesized using a solid state processing technique.⁴⁴ A two step reaction was used. The first reaction step, given in Eq. 2-1 was common for all the compositions synthesized. For A-site donor dopants given by the general formula A_2O_3 , the second reaction step is given by Eq. 2-2. For B-site dopants given by the general formula B_2O_5 , the second reaction step is given by Eq. 2-3 and 2-4 when charge is compensated by B and A site vacancies respectively.



Steps used in the synthesis are shown in Figure 2-1. Ball milling was carried out in ethanol, using spherical yttria stabilized zirconia (YSZ) media, 3 mm in diameter. The calcination conditions for the first reaction step was 1300°C, for 4 h using a ramp rate of 4°C/min. 2 mol% above the stoichiometric quantity of PbO was used to compensate for lead volatilization in the second reaction step.¹⁶ The calcination conditions for reactions 1-2 and 1-3 is 950°C for 3 h using a ramp rate of 4°C/min. Both uniaxial and isostatic pressing were used to form dense ceramics. A PbTiO_3 powder bed was prepared using $x=1$ in Eq. 1-1. A single reaction step proved sufficient for this purpose. Sintering of the green body was carried out in the bed of PbTiO_3 . The sintering conditions used were 1200°C for 2 h using a ramp rate of 4°C /min

2.2 Temperature Dependent Dielectric Property Measurements

The temperature dependent longitudinal permittivity ($\epsilon_{r,33}$) was measured *in situ* as a function of increasing temperature using an apparatus based on an Inductance (L), Capacitance (C), Resistance (R) (LCR) meter. The sample was suspended from platinum sheathed gold leads in a quartz reactor tube using platinum electrodes. The reactor was then placed in a tube furnace. A calibrated thermocouple was used to measure the temperature. $\epsilon_{r,33}$ was measured using an LCR meter upon heating the sample from room temperature to approximately 600°C at a ramp rate of 2°C/min. The measurements were made at a frequency of 1 kHz. A schematic diagram of the experimental setup is shown in Figure 2-2.

2.3 Temperature Dependent Piezoelectric Property Measurements

The temperature dependent converse longitudinal piezoelectric coefficient (d_{33}) was measured *in situ* as a function of increasing temperature using an apparatus based on Doppler vibrometry^{45,46} shown schematically in Figure 2-3. Poled samples were placed in a furnace with two thermocouples to cross-check the uniformity of temperature around the sample. The laser from the vibrometer (Politec sensor head OFV-505 and front-end VDD-E-600) was coupled to the sample surface through a pinhole in the center of a porous alumina lid used for thermal insulation. Displacements induced in the sample due to the converse piezoelectric effect were determined by the Doppler effect with a precision of ± 1 pm,^{47,48} although the actual resolution is limited by background noise at >10 pm. A sinusoidal AC voltage of ± 10 V at a frequency of 1 kHz was used as an input signal. Data were obtained upon heating from room temperature to approximately 400°C, using a ramp rate of 2°C/min.

2.4 Characterization of Electric Field induced Structural Changes using High Energy X-ray Diffraction from a Synchrotron Source

The electric field induced structural response of piezoelectric PZT can be characterized using diffraction.⁴⁹ X-rays from a synchrotron source were chosen for this study as they have higher flux when compared to laboratory X-rays. High flux is essential for this work as subtle structural changes that occur in the material as a response to the applied electric field are measured. Due to a large penetration depth, high energy X-rays also enable greater sampling volume and less surface sensitivity than laboratory X-rays.

2.4.1 Experimental Setup

High energy X-ray diffraction experiments were carried out on beamline 11-ID-C at the Advanced Photon Source, Argonne National Laboratory. A monochromatic beam of energy 114 keV and size 500 μm \times 500 μm was used. A ceria powder pattern was measured in order to calibrate the distance and orientation of the detector relative to the sample and beam. Diffraction patterns were collected using forward scattering geometry (transmission mode) on a Perkin Elmer amorphous silicon area detector placed approximately 2.2 m from the sample. A schematic of the measurement setup is shown in Figure 2-4. *In situ* measurements were recorded during the application of an electric field. Sub-coercive electric field cycling measurements utilized stroboscopic data acquisition procedures.⁵⁰ Figure 2-5 illustrates the differences between a diffraction pattern taken with and without electric field loading of the sample. Time resolved diffraction images were collected during cyclic actuation of the sample. The stroboscopic data acquisition process was achieved by the following process. An electric field signal was applied across the sample using a function generator (FLUKE

PM5193) and a high-voltage amplifier (TREK 10/10B). A delay generator was simultaneously triggered by this signal and applied a set delay. This delayed signal was then used to trigger a detector frame, the length of which provided the time resolution of the experiments. A number of detector frames were then summed together to produce a single image, and the delay signal was adjusted. In this way, large area detector images are collected as a function of time that can be represented in a single electric field cycle.⁵¹

2.4.2 Binning of Diffraction Data

The 2-D images from the area detector were initially analyzed using the software *Fit2D Ver. 12.077*. The beam center and tilt were refined for each pattern with respect to a standard diffraction pattern of CeO₂ (standard reference material 674b from National Institute of Standards and Technology), recorded under identical collection settings. The Debye-Scherrer diffraction rings from the sample were segmented into azimuthal sectors of 15° width. The pattern within each azimuthal sector (Φ), was integrated to obtain equivalent diffracted intensities as a function of 2θ . The pattern of the hkl diffracted intensity within each azimuthal sector Φ is indicative of the structural state of grains with their hkl poles approximately parallel to an angle Φ to the applied electric field (within $\pm 5^\circ$).⁵¹

2.5 Characterization of Temperature Dependent Structural Changes using High Resolution XRD from a Synchrotron Source

In order to capture the subtle temperature dependent structural differences within various soft doped polycrystalline PZT ceramics, accurate structural information is critical. Hence, high resolution powder diffraction patterns were measured at beamline 11-BM⁵² at the Advanced Photon Source, Argonne National Laboratory. A

monochromatic X-ray beam with a wavelength of 0.412956 Å and a 2θ range of 0-20° with a step size of 0.0001° in 2θ was used. The sample powders were packed into a 0.3 mm diameter quartz capillary and spun at 60 Hz. The samples were heated from room temperature to 500°C at a ramp rate of 2°C/min using a Cyberstar hot gas blower. XRD patterns were measured for 30 min at six distinct temperatures in the following order: 500°C, 360°C, 332°C, 308°C, 290°C and 250°C. Data from this series of measurements were analyzed using the Rietveld refinement program GSAS.

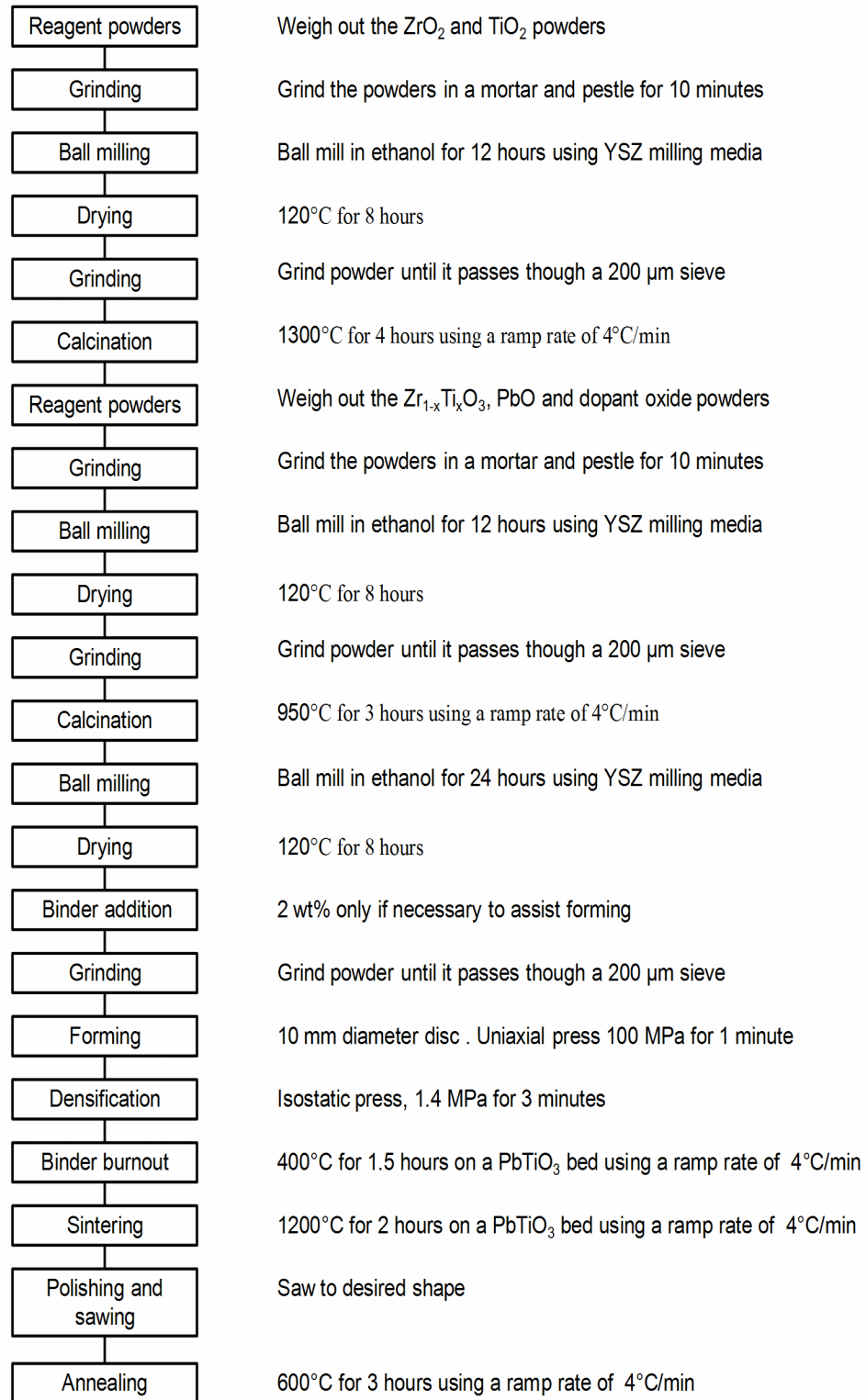


Figure 2-1. Processing steps for PbZr_{1-x}Ti_xO₃ based ceramic synthesis.

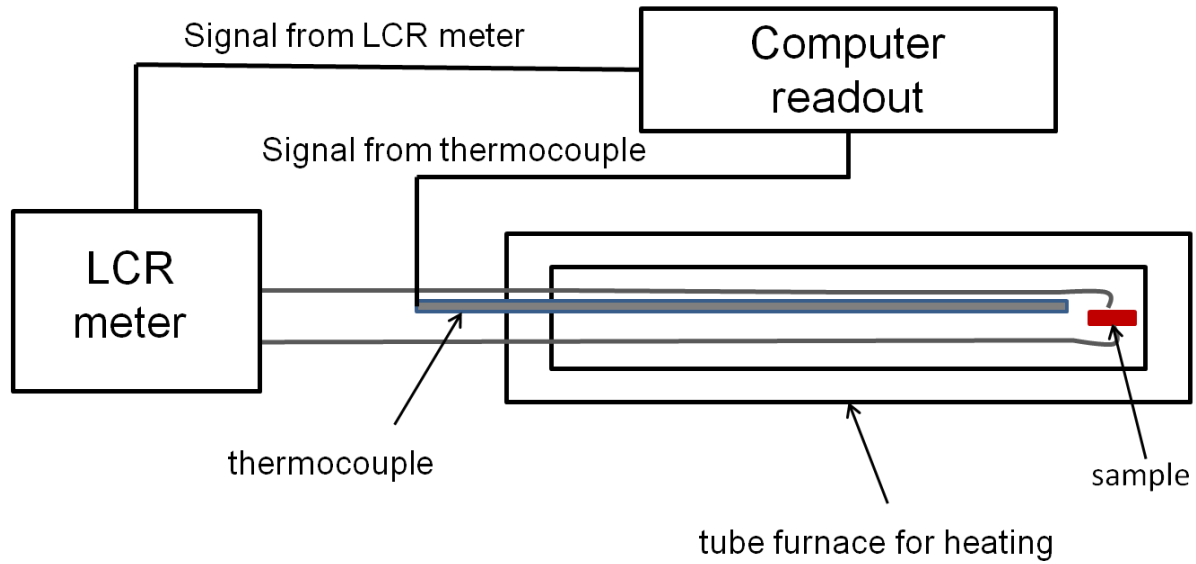


Figure 2-2. Schematic diagram of the measurement apparatus used to determine the *in situ* temperature dependent longitudinal relative permittivity.

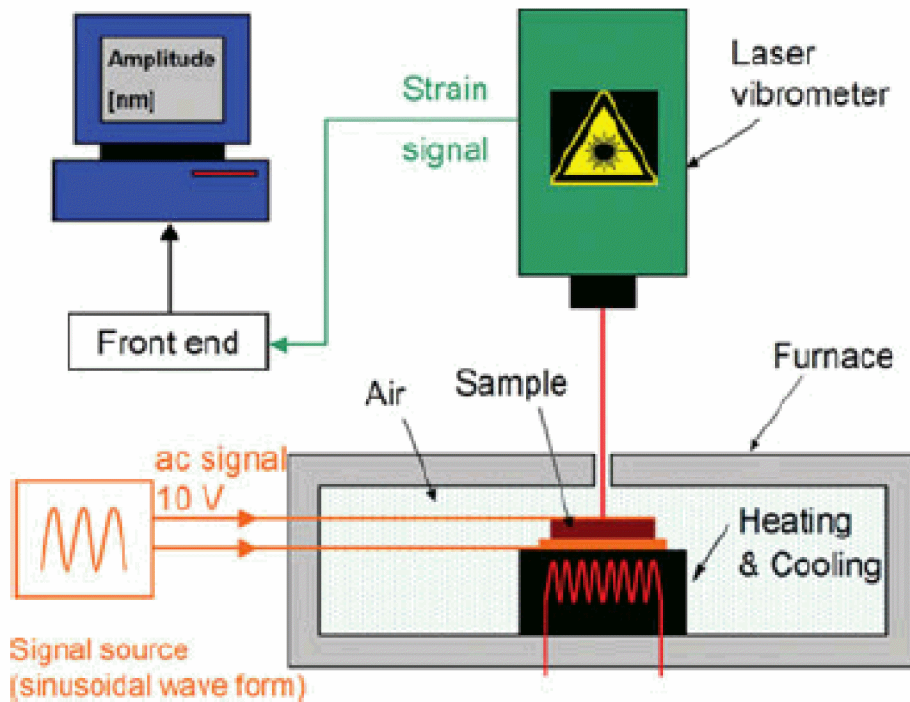


Figure 2-3. Schematic of the measurement apparatus used to determine the *in situ* temperature dependent converse longitudinal piezoelectric coefficient. Reprinted from T. Leist, J. Chen, W. Jo, E. Aulbach, J. Suffner, and J. Rödel, "Temperature Dependence of the Piezoelectric Coefficient in BiMeO₃-PbTiO₃ (Me = Fe, Sc, (Mg_{1/2}Ti_{1/2})) Ceramics," (Page 712, Figure 1) *J. Am. Ceram. Soc.*, **95** [2] 711-5 (2012).

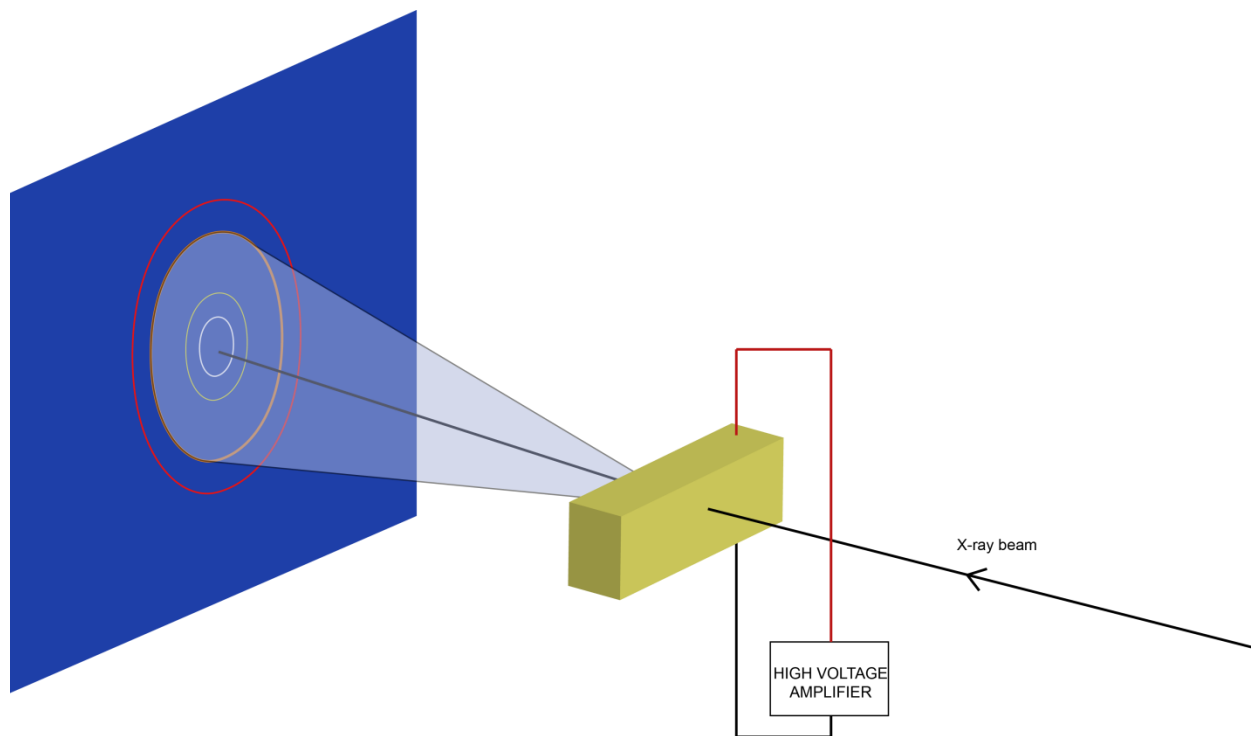


Figure 2-4. Experimental arrangement for time-resolved high energy X-ray diffraction. The X-ray beam penetrates the sample simultaneous to the application of an electric field. The 2D diffraction image shows the Debye-Scherrer rings.

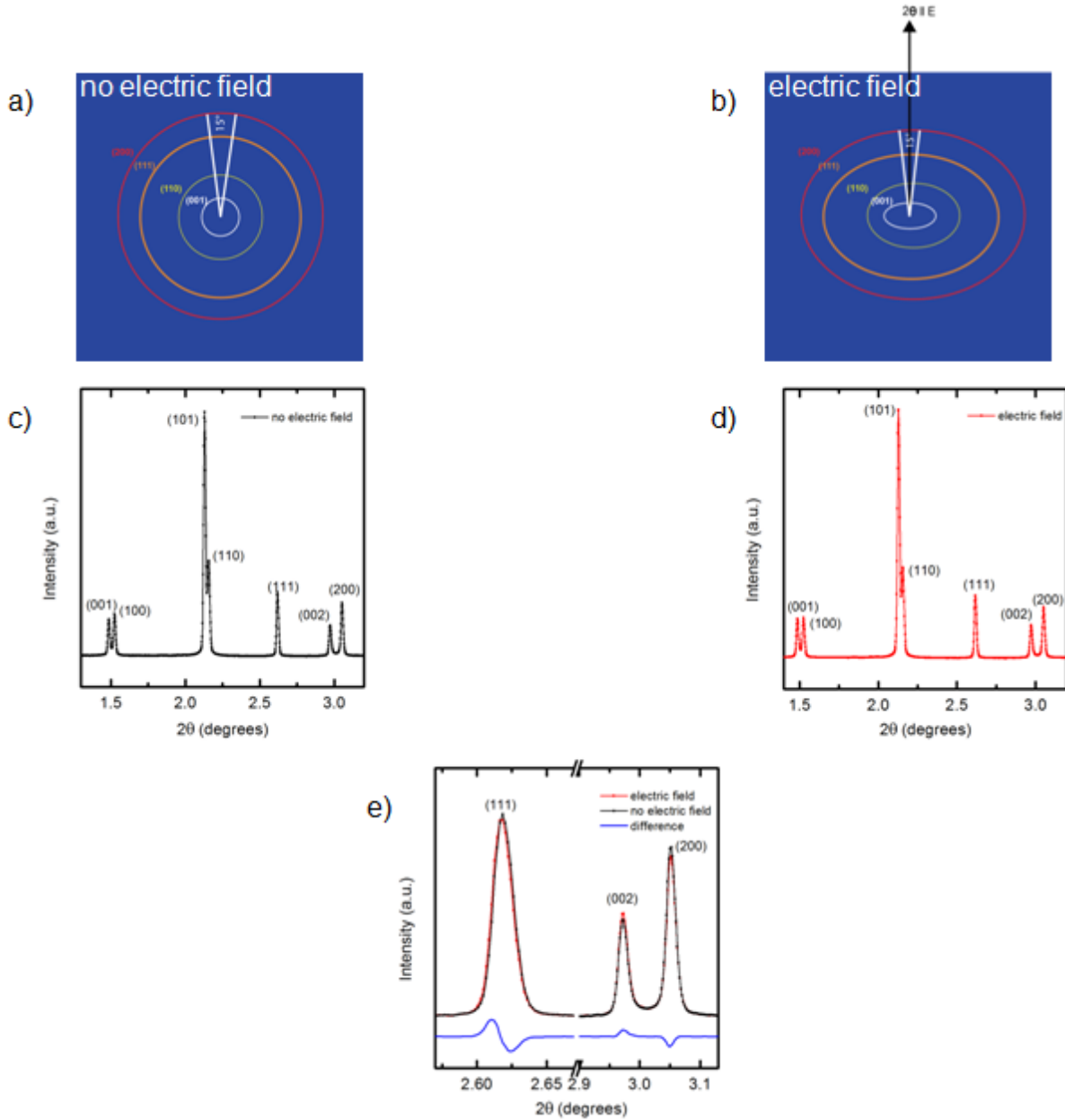


Figure 2-5. Schematic of a 2D diffraction image showing the Debye-Scherrer ring as measured when a) no electric field is b) an electric field is applied to the sample. The distortion of the Debye-Scherrer ring in b) is exaggerated. hkl peaks obtained after integrating the azimuthal sector 0° for 2 at% Sm doped 50:50 PZT when c) no electric field is applied d) an electric field is applied to the sample. e) (111) and (002) hkl peaks of Sm PZT as measured with and without the application of an electric field. The blue difference pattern emphasizes the change in d spacing of the (111) plane and interchange in intensities between the (002) and (200) planes that takes place upon the application of an electric field.

CHAPTER 3
A STRUCTURAL INSIGHT INTO THE SOFTENING MECHANISMS IN LEAD
ZIRCONATE TITANATE

3.1 Softening in Donor Substituted PZT

Lead zirconate titanate ($\text{PbZr}_{1-x}\text{Ti}_x\text{O}_3$ or PZT) based ceramics are extensively used in science, medicine, and several industries such as transportation, communications and information technologies.^{11,12,18,53,54,55,56} Typically, commercial PZT ceramics are compositionally modified with small amounts of chemical additives in order to improve, optimize or tailor their properties for specific applications.^{18,57} When a substituent whose valence is higher than the host ion (donor dopant) is used, PZT becomes a "soft" ferroelectric. A characteristic of soft ferroelectric ceramics is an increase in the longitudinal piezoelectric coefficient (d_{33}).^{4,7,16} Softening has been associated with an increase in Pb vacancies that arise to charge-compensate for aliovalent donor doping^{58,59} and their interaction with domain walls. Despite the widespread use of soft PZT, the structural origin of the variation in d_{33} brought about by donor doping remains unknown due to a lack of *in situ* characterization of the crystallographic structural response. The exact mechanism by which softening occurs is therefore still uncertain.^{60,61,62} Until now, it has been thought that there is no qualitative difference in the mechanism by which different dopants generate softening.¹⁸ For example, regardless of whether Nd^{+3} or La^{+3} is substituted for Pb^{+2} on the A-site, it is thought that the softening of the PZT material (and the corresponding increase in d_{33}), is brought about by the same qualitative mechanism that is associated with an increase in Pb vacancies. In this study, we use high energy X-rays from a synchrotron source to study the structural response of soft PZT to the application of electric fields. The structural changes occurring during the application of both strong (greater than

coercive) and weak (subcoercive) electric fields is measured *in situ* on four different soft doped PZT materials. It is shown that dopants can have different qualitative mechanisms by which they generate softening and high d_{33} . From these measurements, distinct qualitative softening mechanisms are correlated to different quantitative d_{33} values.

3.2 Experimental

3.2.1 Sample Preparation

2 at% of four donor dopants, Sm^{+3} , Nd^{+3} , La^{+3} (A-site substituents) and Nb^{+5} (B-site substituent) were used to dope PZT 50:50. Stoichiometric quantities of the reactants were chosen such that charge compensation for the A-site substituents was by Pb vacancies as given in Eq. 3-1.



The chemical reaction used for A-site substitution is given in Eq. 2-2. The chemical formula of the resultant A-site substituted PZT 50:50 compositions were $\text{Pb}_{0.97}\text{Sm}_{0.02}\text{Zr}_{0.5}\text{Ti}_{0.5}\text{O}_3$, $\text{Pb}_{0.97}\text{Nd}_{0.02}\text{Zr}_{0.5}\text{Ti}_{0.5}\text{O}_3$, and $\text{Pb}_{0.97}\text{La}_{0.02}\text{Zr}_{0.5}\text{Ti}_{0.5}\text{O}_3$.

Two types of Nb-doped PZT 50:50 compositions were synthesized. One composition was synthesized as per the chemical reaction given in Eq. 2-3. Charge compensation for the B-site dopant was by Zr and Ti vacancies as per Eq. 3-2. This composition is referred to as Zr or Ti vacancy compensated Nb-doped PZT 50:50.



The chemical formula of the resultant B-site substituted PZT 50:50 compositions was $\text{PbZr}_{0.485}\text{Ti}_{0.485}\text{Nb}_{0.02}\text{O}_3$.

Another type of B-site substituted PZT 50:50, where charge compensation due to doping was by Pb vacancies as per Eq. 3-3 was also synthesized. The chemical reaction used for the synthesis of this composition is given in Eq. 2-4. This composition is referred to as Pb vacancy compensated Nb-doped PZT 50:50.



The chemical formula of the resultant B-site substituted PZT 50:50 compositions was $Pb_{0.99}Zr_{0.49}Ti_{0.49}Nb_{0.02}O_3$.

Disc shaped pellets, 10 mm in diameter and 1 mm in thickness, of all compositions were prepared using the conventional solid state synthesis and sintering techniques described in Section 2.1. The samples were electroded with silver paste and used for the coercive field and piezoelectric coefficient measurements. Samples of dimensions 6 mm × 1 mm × 1 mm were sliced from other disc shaped pellets. The samples were annealed at 600°C for 3 h using a ramp rate of 4°C/min. The samples were then electroded with silver paste for use in the diffraction experiments. For Nb-doped PZT, diffraction experiments were performed only on the Pb vacancy compensated composition.

3.2.2 Diffraction Measurements

High energy X-ray diffraction experiments were carried out on beamline 11-ID-C at the Advanced Photon Source, Argonne National Laboratory using a monochromatic beam of energy 114 keV and size 500 μm × 500 μm. A ceria powder pattern was measured in order to calibrate the distance and orientation of the detector relative to the sample and beam. Diffraction patterns were collected using forward scattering geometry (transmission mode) on a Perkin Elmer amorphous silicon area detector placed

approximately 2.2 m from the sample. *In situ* measurements were recorded during the application of an electric field. Electric fields were applied cyclically to the samples utilizing the stroboscopic data acquisition⁵⁰ technique described in Section 2.4.1. For these stroboscopic measurements, the electric field was synchronized with the detector electronics and the material response to 20 repetitive electric field cycles were summed at particular time periods relative to the waveform. The angle between the electric field direction and scattering vectors of planes measured on the detector is $2\theta/2$. This value is approximately 1.5° for the (002) reflection. In polycrystalline ferroelectric materials, planes at these angles to the electric field direction behave equivalently to those parallel to the electric field.^{22,63}

3.2.3 Coercive Field and Piezoelectric Coefficient Measurements

The coercive field of the samples was determined from the polarization response of the materials to an applied bipolar electric field of triangular waveform and frequency 1 Hz. Polarization was measured using a 15 μF capacitor in a Sawyer-Tower circuit. The Berlincourt d_{33} of the samples was measured after the diffraction experiments.

3.3 Results

The coercive fields of the Sm, Nd, La and Nb-doped PZT compositions, were found to be 2.68, 2.40, 2.41 and 2.04 kV/mm, respectively when measured at a frequency of 1 Hz. These PZT compositions were subjected to strong electric fields of amplitude 1.3 times coercive fields for 5 min during diffraction measurements. Berlincourt d_{33} values of the compositions as measured after the diffraction experiments were found to be 77, 149, 109 and 202 pC/N for Sm, Nd, La and Nb-doped PZT, respectively.

The effect of the substitution scheme on the piezoelectric coefficients were also evaluated. The Pb vacancy and Zr or Ti compensated Nb-doped PZT were poled by the application of strong electric fields of amplitude equal to their coercive field for 5 min. The Berlincourt d_{33} values of the Pb vacancy and Zr or Ti compensated Nb-doped PZT after poling were found to be 120 ± 5 pC/N and 134 ± 16 pC/N respectively.

A selected region of the diffraction pattern of the unpoled samples is shown in Figure 3-1. Table 3-1 shows the unit cell parameters and c/a ratios of the doped PZT compositions.

In order to orient the domains in the material, a strong bipolar electric field of triangular waveform with a frequency of 0.05 Hz and amplitude equal to approximately 1.3 times the coercive field of material was applied to each of the doped compositions. Three such triangular waveforms were applied. *In situ* diffraction was performed to capture the structural response of the material to the application of strong fields. The structural changes occurring during the application of strong electric fields become more apparent with the application of each subsequent waveform. Figures 3-2 and 3-3 show portions of the diffraction pattern collected with the scattering vector parallel to the electric field direction during the application of the first and third electric field cycle, respectively. The diffraction patterns show how the nature of the (002) type diffraction peaks change as a function of time in response to the triangular, bipolar electric field waveform applied during the poling cycle.

In the case of the Sm and Nd-doped PZT materials an intensity interchange occurs between the tetragonal (002) and (200) peaks when the electric field changes sign. This can be the result of a change in the volume fraction of the ferroelectric

domains that is brought about by 90° domain wall motion.⁶³ The La and Nb compositions also show an intensity interchange between the tetragonal (002) and (200) reflections. In the case of the La and Nb-doped PZT compositions, an additional peak is observed between the (002) and (200) tetragonal reflections. This can be interpreted to be due to the presence of the rhombohedral phase in addition to the tetragonal phase. Further, an electric field induced phase transformation of the tetragonal phase to the rhombohedral phase is observed in Nb-doped PZT.

A positive d.c. electric field of magnitude 1.3 times the coercive field of the material was applied to each of the four differently doped PZT compositions for 5 min in order to further strengthen the domain alignment in the positive electric field direction. Diffraction patterns of the samples were measured after the application of the d.c. field. The {002} type reflections of these patterns are shown in Figure 3-4 and compared to the patterns from the unpoled (initial) condition. A difference plot highlighting the changes that emerged in each of the doped PZT materials due to the application of strong electric fields is also shown in Figure 3-4. The interchange in the tetragonal (002) and (200) intensities observed in all samples shows that the fraction of 001(c-axis)-type domains grew at the expense of the 100(a-axis) type domain due to 90° domain wall motion.

Subsequently, unipolar square electric fields of frequency 0.02 Hz and subcoercive amplitudes equal to approximately 0.7 times the 1 Hz coercive field of the materials were applied and diffraction data were measured using the stroboscopic approach.^{22,63} The contour plots in Figures 3-5 (a), (b), (c) and (d) show the changes occurring in the {002} diffraction peaks as a function of time during the application of

these subcoercive electric fields. The line plots in Figure 3-6 show the difference in the structure between the zero field and positive subcoercive field state. For all the samples, no change is observed in the {002} reflections during the first 25 s of the waveform as the electric field amplitude is zero during this portion of the waveform. After the electric field is applied, the intensity of the tetragonal (002) reflection increases and there is a corresponding decrease in the intensity of the (200) reflection in all four differently doped materials. The change in intensities between the positive and zero polarity of the electric field implies that there is motion of the 90° walls separating these domains. In the case of the La-doped sample, there is no change in the volume fraction of the rhombohedral phase between the zero and positive polarity states of the subcoercive electric field. The rhombohedral phase fraction of the Nb-doped sample increases during the positive polarity state of the subcoercive electric field. This is indicative of interphase boundary motion during the application of subcoercive electric fields in Nb-doped PZT. Notably, interphase boundary motion in Nd doped PZT 50:50 occurs during both strong and weak field conditions.

Peak center positions were obtained by curve fitting to a Gaussian triplet as shown in Figure 3-7. The shift in the (200)_R peak to lower 2θ positions during the positive state of the electric field is indicative of a large strain in the (200)_R lattice plane ($\epsilon_{33,(200)R}$). It is given by Eq. 3-4.

$$\epsilon_{33,(200)R} = \frac{d_1 - d_0}{d_0} \quad (3-4)$$

In Eq. 3-4, d_0 and d_1 are the d spacing of the (200)_R lattice plane during the off and positive polarity of the subcoercive electric field respectively. The electric field induced

strain coefficient in the rhombohedral peak ($d_{33,(200)R}$) can then be calculated as per Eq. 3-5.

$$d_{33,(200)R} = \frac{\varepsilon_{33,(200)R}}{E_0} \quad (3-5)$$

E_0 is the amplitude of the subcoercive field. In Nb-doped PZT, $d_{33,(200)R}$ is found to be 950 ± 22 pm/V.

3.4 Discussion

As the d_{33} values of the Pb vacancy and Zr or Ti compensated Nb-doped PZT were found to be 120 ± 5 pC/N and 134 ± 16 pC/N respectively, there is no statistically significant difference in the d_{33} values resulting from these two different substitution schemes. Thus, the data suggests that Pb vacancies are not a necessary criterion for softening in PZT.

The {002} reflections of the four unpoled PZT compositions show that various soft dopants have distinctive influences on c and a-axis distortion and phase. These structural parameters, coupled with interaction among grains and domains, local texture and internal stresses in ceramics, affect the overall intrinsic and extrinsic strain response in piezoelectric ceramics.^{34,35} The four soft doped PZT based ceramics showed Berlincourt d_{33} values that varied from 77 pC/N (in Sm-doped PZT) to 202 pC/N (in Nb-doped PZT). *In situ* diffraction experiments during the application of strong and weak subcoercive electric fields show that the differently doped materials display four distinctive strain mechanisms which are outlined in Sections 3.4.1 to 3.4.4. A summary of the strain mechanisms displayed by the dopants is given in Table 3-2.

3.4.1 90° Domain Wall Motion

The intensity interchange between the tetragonal (002) and (200) peaks was used to infer the motion of 90° domain walls. Sm, Nd, La and Nb-doped PZT all show 90° domain reorientation during both strong and weak electric field cycling. 90° domain wall motion leads to a change in the volume fraction of the c(001)-type domains. This effect is known to increase the extrinsic strain response and hence results in materials with higher d_{33} ^{22,51} which is characteristic of soft ferroelectrics.

3.4.2 Coexistence of mixed ferroelectric phases

In the La and Nb-doped compositions, two ferroelectric phases coexist. In the Nb-doped composition, an electric field dependent interphase boundary motion between the ferroelectric tetragonal phase to the ferroelectric rhombohedral phase was observed. This was evidenced by the appearance of a (200) rhombohedral peak together with a corresponding decrease in the intensity of the {200} tetragonal peaks. Diffraction patterns recorded after the application of electric fields show that the rhombohedral phase formed during the application of strong electric fields, remains in the material when the electric field is removed after poling. Some differences were observed in the rhombohedral phases of the La and Nb-doped samples. Under strong bipolar electric field amplitudes, a volume fraction of the tetragonal material is transformed to the rhombohedral phase in Nb-doped PZT, whereas the volume fraction of the rhombohedral phase remains roughly the same even under strong bipolar electrical field loading in La-doped PZT. This indicates that Nb-doped PZT may be closer in proximity to the rhombohedral-tetragonal MPB as the energy barrier for the phase transition is smaller in the case of the Nb-doped material. As Nb is a B-site substituent and the compensation for aliovalent doping in Nb-doped PZT was by Zr and

Ti vacancies, the Nb-doped PZT composition could be closer to the MPB than the La-doped composition.

3.4.3 Interphase Boundary Motion During Subcoercive Electric Field Application

The volume fraction of the tetragonal and rhombohedral phases remains constant during subcoercive cycling in La-doped PZT. This suggests that the weak electric fields applied during this experiment are insufficient to overcome the phase transition energy barrier present in this material. On the other hand, the volume fraction of the rhombohedral phase increases during the positive polarity of the subcoercive electric field waveform in Nb-doped PZT. This indicates that the interphase boundary between the tetragonal and rhombohedral phases moves during subcoercive electric field cycling in Nb-doped PZT. It has been hypothesized^{21,27,64,65,66} and also directly demonstrated²⁷ that interphase boundary contributes to an increase in piezoelectric coefficients. The present results further demonstrate a measureable contribution of interphase boundary motion to the piezoelectric coefficients in ceramics.

3.4.4 Strain in the Rhombohedral (200) Lattice Plane

There is a sizeable shift in the (200)_R peak of Nb-doped PZT which is indicative of the large strain in the rhombohedral (200) lattice plane in Nb-doped PZT. This equates to a high $d_{33,(200)R}$ of 950 pm/V. As large strain coefficients of individual lattice planes contribute to the total strain response of the material, the high $d_{33,(200)R}$ contributes to an increase in the piezoelectric coefficient of Nb-doped PZT. It has been previously shown that the (00l) planes of the rhombohedral phase strain significantly more than other planes. For example, Du et al.⁶⁷ demonstrated that the piezoelectric coefficients are orientation dependent in PZT through phenomenological calculation. As a result of this orientation dependence, they suggest that the effective d_{33} can be

enhanced by a factor of 4 when the [001] orientation is favored in epitaxial thin films. The rhombohedral phase of $\text{Pb}(\text{Mg}_{1/3}\text{Nb}_{2/3})\text{O}_3\text{-PbTiO}_3$ (PMN-PT), $\text{Pb}(\text{Zn}_{1/3}\text{Nb}_{2/3})\text{O}_3\text{-PbTiO}_3$ (PZN-PT), $\text{Pb}(\text{Sc}_{1/2}\text{Nb}_{1/2})\text{O}_3\text{-PbTiO}_3$ (PSN-PT) and $\text{Pb}(\text{Yb}_{1/2}\text{Nb}_{1/2})\text{O}_3\text{-PbTiO}_3$ (PYbN-PT) single crystals have also been shown to have high piezoelectric coefficients when measured along the $\langle 001 \rangle$ direction even though $\langle 111 \rangle$ is the polar direction.^{68,69,70} The $(200)_R$ peak in La-doped PZT does not strain under the application of an electric field. Hence, $d_{33,(200)R}$ in La-doped PZT is zero. Thus, there is no contribution from $d_{33,(200)R}$ to the piezoelectric coefficient in La-doped PZT.

3.5 Conclusions

In contrast to prior-held assumptions, the results suggest that an increase in Pb vacancies is not a necessary criterion for softening. While different soft dopants are known to increase the piezoelectric coefficient, this work has uniquely shown that these different dopants do so by activating distinctive strain mechanisms. The present work alternatively suggests that the value of piezoelectric coefficient depends on the number and magnitude of the strain mechanisms in play.

Nb-doped PZT exhibits all four strain mechanisms and, as a result, Nb-doped PZT has the highest d_{33} (202 pC/N). Although Nd doping gives rise only to one strain mechanism (90° domain wall motion) it has the next highest d_{33} (149 pC/N). It is suggested that this is because the magnitude of 90° domain wall motion that occurs in Nd-doped PZT is large relative to the other doped compositions. La-doped PZT exhibits two strain mechanisms (90° domain wall motion and the coexistence of ferroelectric phases). It has the third highest d_{33} (109 pC/N). Sm-doped PZT exhibits only 90° domain wall motion. It is suggested that the extent of 90° domain wall motion in Sm-

doped PZT is lesser than that in Nd doped PZT. Sm doped PZT has the lowest d_{33} (77 pC/N).

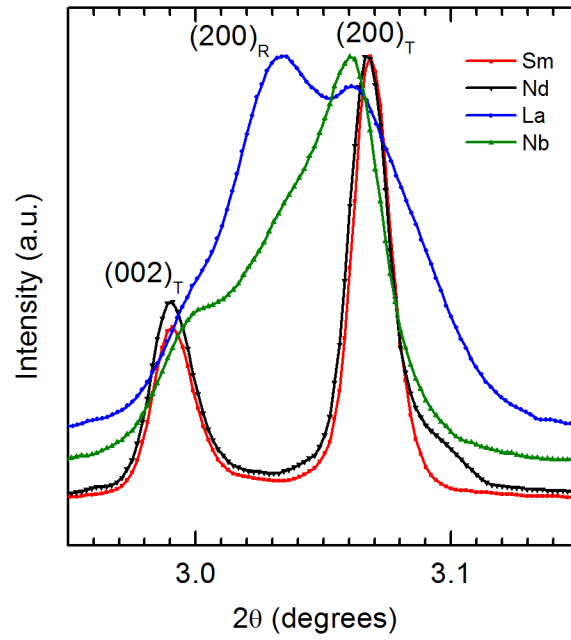


Figure 3-1. Diffraction patterns showing the (002) and (200) reflections of 2 at. % Sm, Nd, La and Nb doped PZT 50:50 before the application of an electric field.

Table 3-1. Lattice parameters, phases present and coercive fields of the various doped PZT 50:50 compositions. The c lattice parameter is not calculated for La-doped PZT 50:50 as the (200)_T peak is not sufficiently resolved.

Dopant	c (Å)	a (Å)	c/a	phase	E _c (kV/mm)
Sm	4.138(±0.005)	4.033(±0.005)	1.026(±0.001)	<i>P4mm</i>	2.68
Nd	4.138(±0.003)	4.035(±0.003)	1.026(±0.001)	<i>P4mm</i>	2.40
La	-	4.036(±0.007)	-	<i>P4mm</i> <i>R3m</i>	2.41
Nb	4.126(±0.006)	4.043(±0.009)	1.021(±0.003)	<i>P4mm</i> <i>R3m</i>	2.04

Table 3-2. Strain mechanisms in soft doped PZT 50:50 compositions. The checks and crosses denote the strain mechanisms present and absent respectively.

	Sm ($d_{33} = 77$ pC/N)	Nd ($d_{33} = 149$ pC/N)	La ($d_{33} = 109$ pC/N)	Nb ($d_{33} = 202$ pC/N)
90° domain wall motion	✓	✓	✓	✓
Coexistence of ferroelectric phases	×	×	✓	✓
Interphase boundary motion	×	×	×	✓
Strain in (200) _R	×	×	×	✓

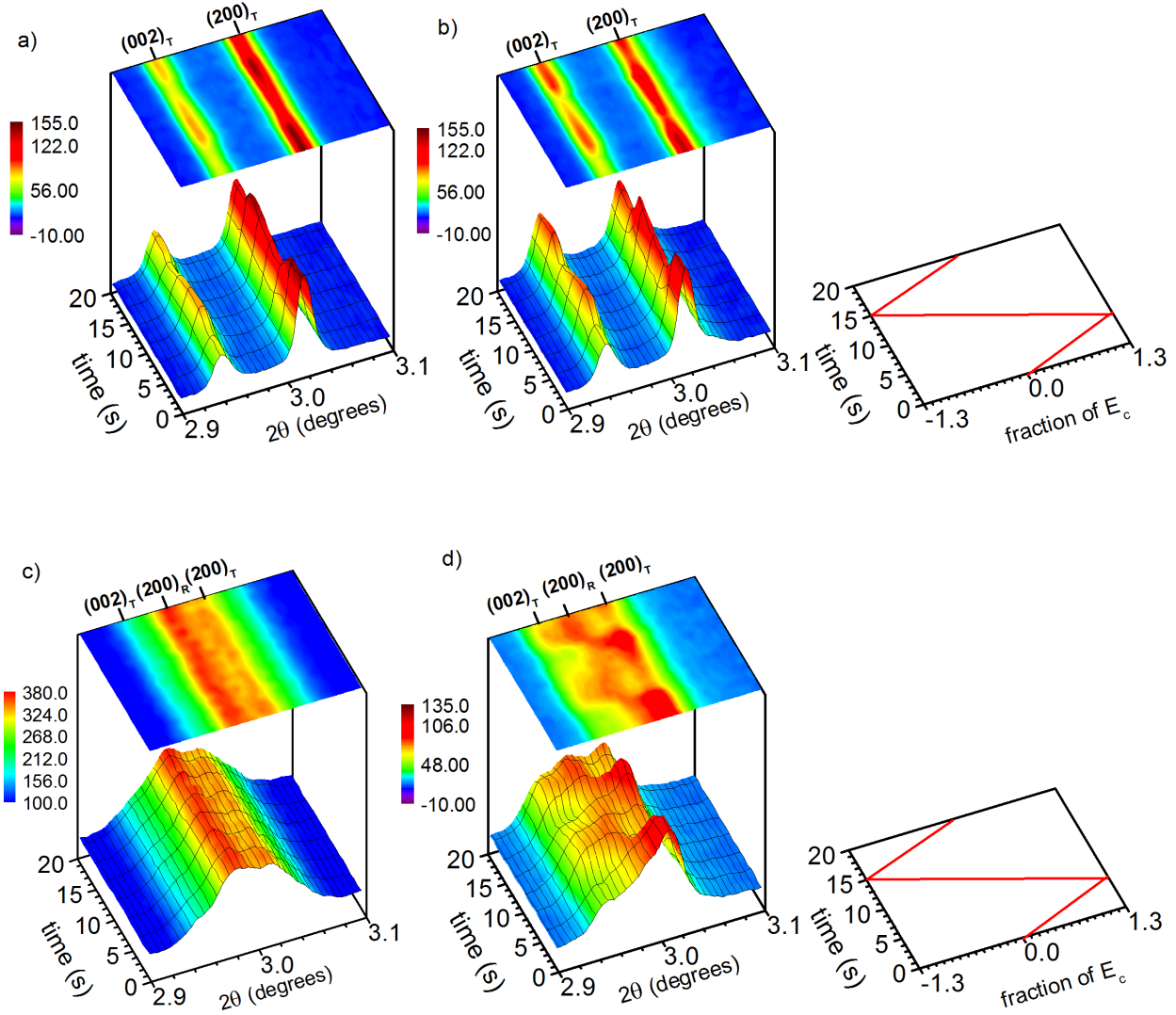


Figure 3-2. Time resolved diffraction patterns measured *in situ* during the application of the first strong bipolar electric field of triangular waveform, frequency 0.05 Hz and amplitude equal to 1.3 times the coercive field (E_c) to a) Sm b) Nd c) La and d) Nb doped PZT 50:50. Intensity interchange between the tetragonal (002) and (200) diffraction peaks due to a change in volume fraction of 90° domains can be observed in a), b), c) and d). Additionally, the appearance of the rhombohedral (200) peak between the tetragonal (002) and (200) peaks is observed in d).

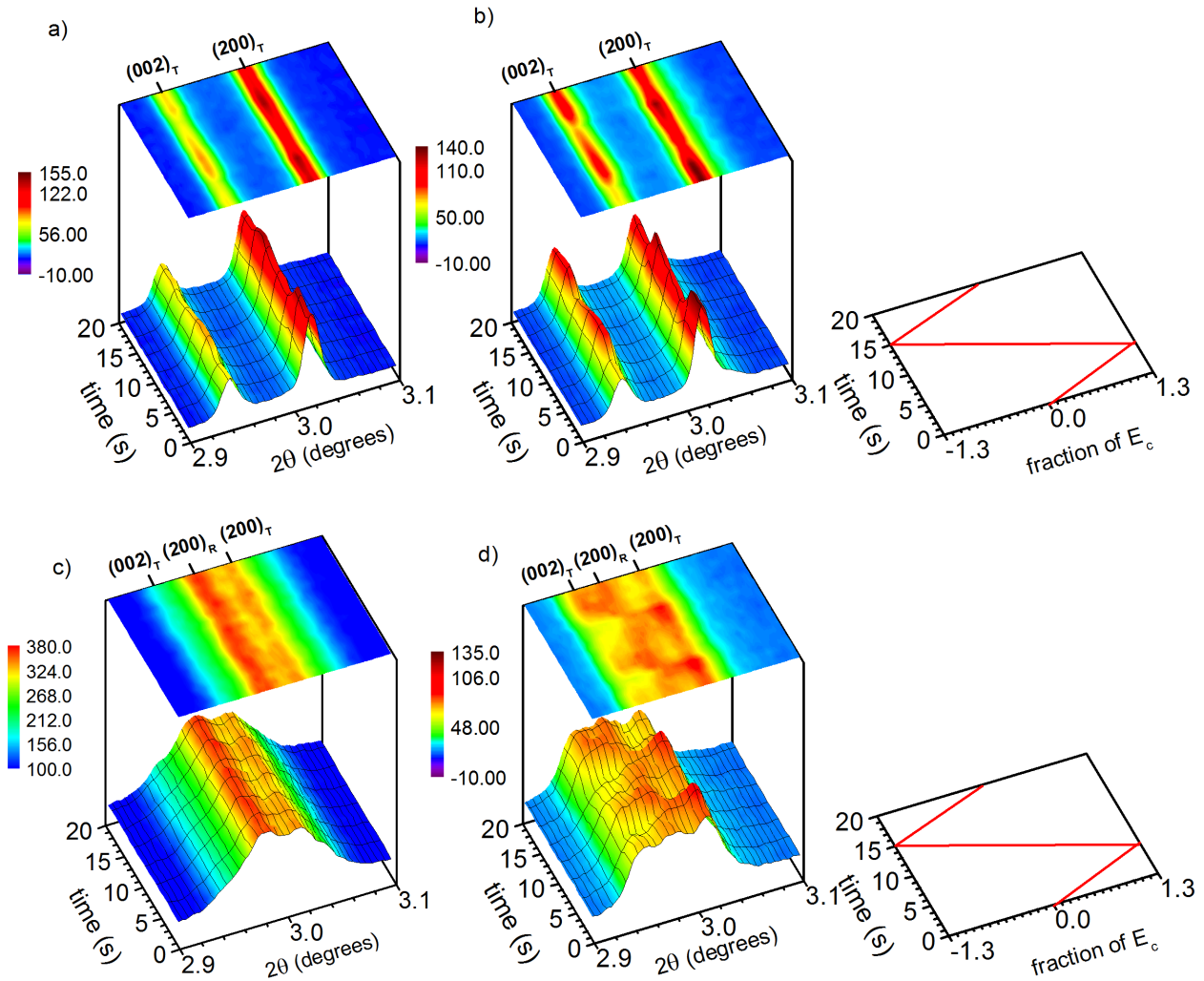


Figure 3-3. Time resolved diffraction patterns measured *in situ* during the application of the third strong bipolar electric field of triangular waveform, frequency 0.05 Hz and amplitude equal to 1.3 times the coercive field (E_c) to a) Sm b) Nd c) La and d) Nb doped PZT 50:50. Intensity interchange between the tetragonal (002) and (200) diffraction peaks due to a change in volume fraction of 90° domains can be observed in a), b), c) and d). Additionally, the appearance of the rhombohedral (200) peak between the tetragonal (002) and (200) peaks is observed in d).

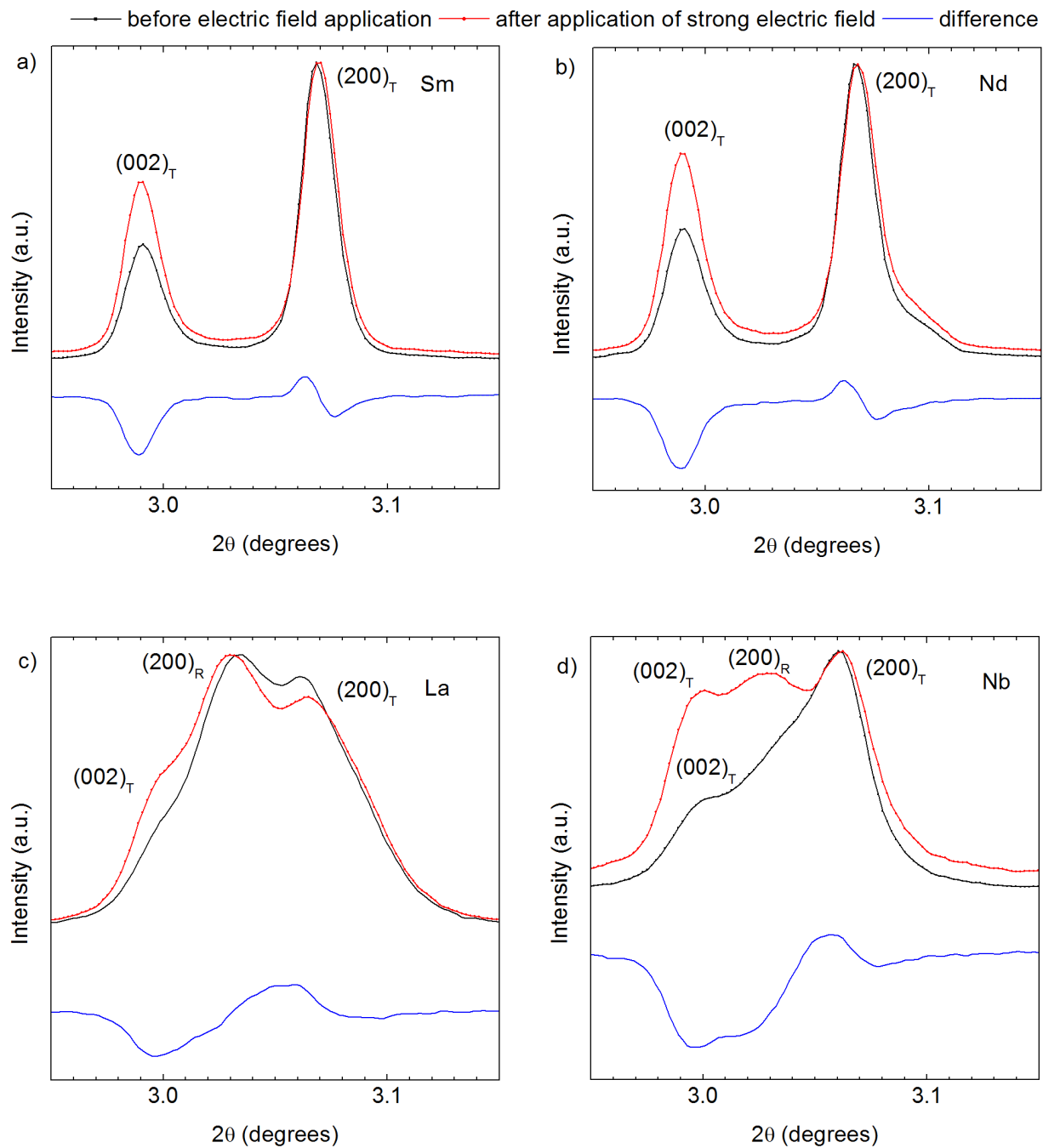


Figure 3-4. Selected region of the diffraction patterns showing the {002} type reflections of a) Sm b) Nd c) La and d) Nb doped PZT 50:50 before and after poling.

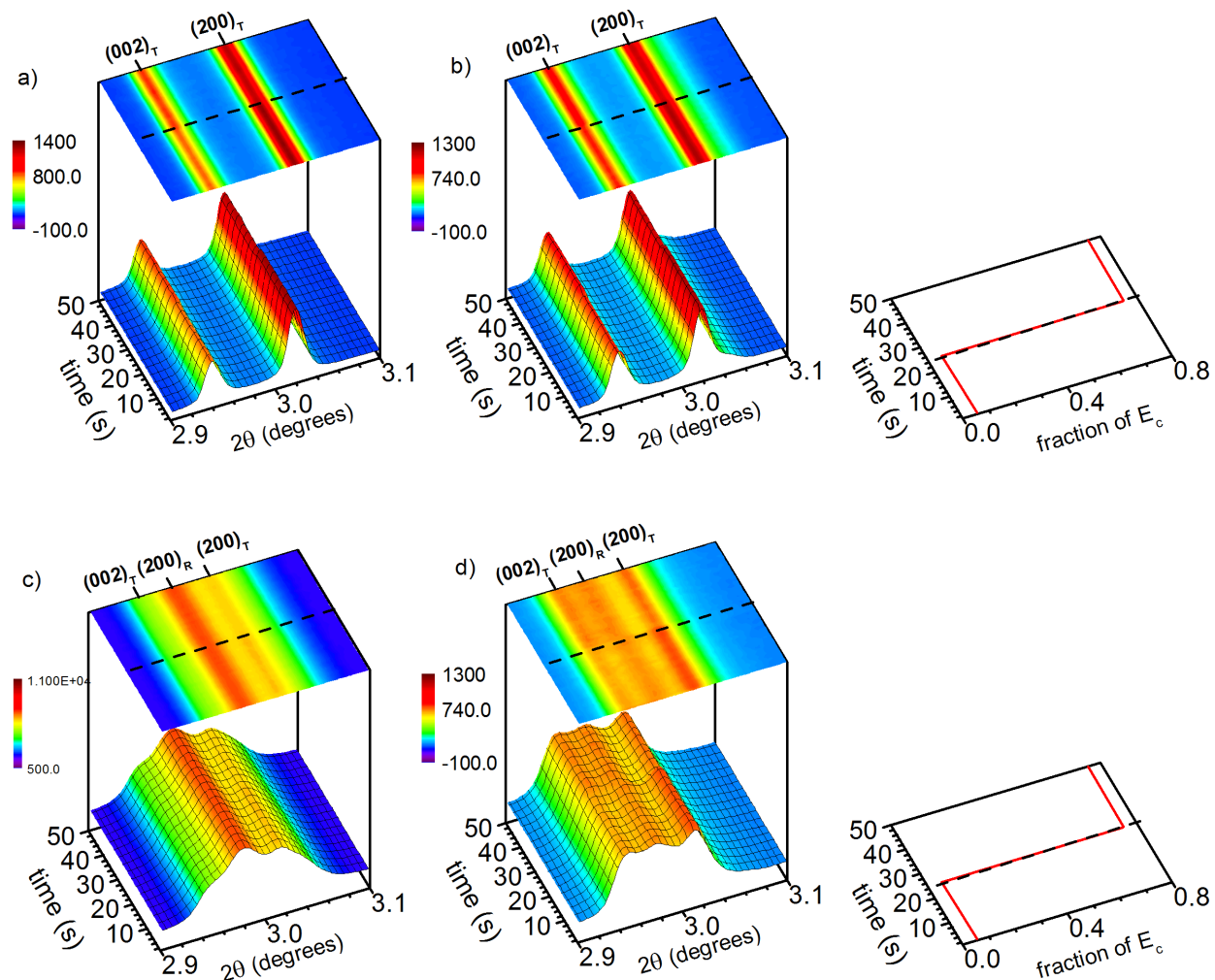


Figure 3-5. Time resolved diffraction patterns measured *in situ* during the application of weak subcoercive electric fields of square waveform, frequency 0.02 Hz and amplitude equal to 0.7 times the coercive field (E_c) to a) Sm b) Nd c) La and d) Nb doped PZT 50:50. Intensity interchange between the tetragonal (002) and (200) diffraction peaks due to an increase in volume fraction of 90° domains during the positive polarity of the electric field can be observed in a), b), c) and d). Additionally, an increase in intensity of the rhombohedral (200) peak is observed in d) during the positive polarity of the electric field. The dashed line on the diffraction contour plots indicate the time at which the amplitude of the electric field changes. The arrows on the plot of the electric field waveform also correspond to this time.

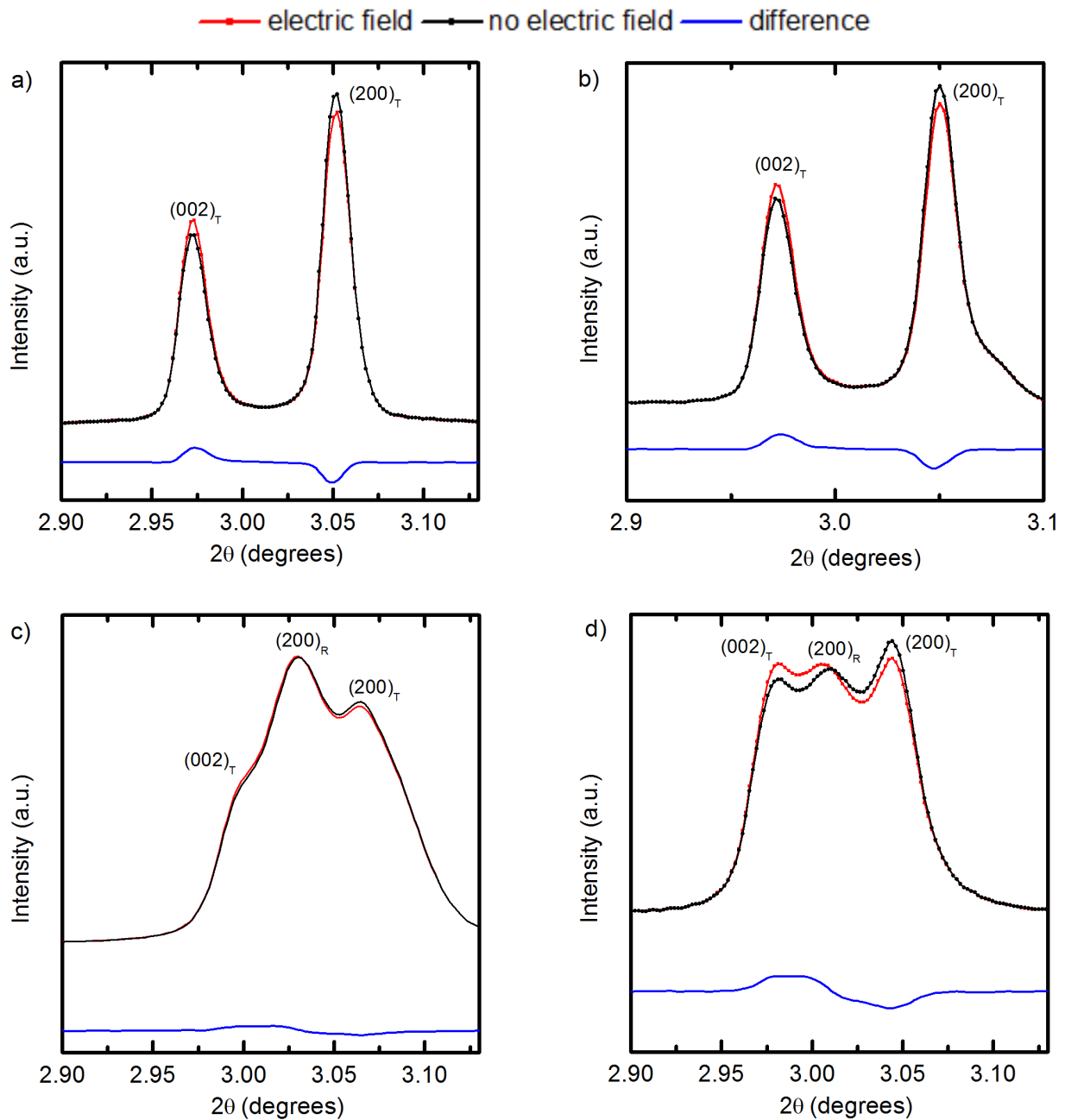


Figure 3-6. Selected region of the diffraction pattern showing the {002} type reflections for a) Sm b) Nd c) La and d) Nb doped PZT 50:50. The behavior of the {002} type reflections when no electric field is applied on the doped PZT compositions is compared to its behavior during the application of a weak, unipolar square electric field waveform of positive polarity, frequency 0.02 Hz and amplitude equal to $0.7E_c$ (subcoercive).

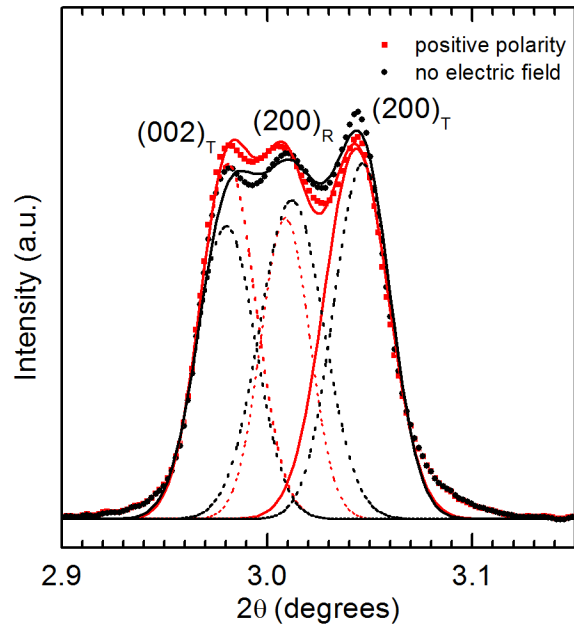


Figure 3-7. Gaussian fits to the {002} reflections in Nb-doped PZT. The (002)_R reflection shifts to higher 2θ value due to strain in the (002)_R during the application of a weak, subcoercive electric field of positive polarity. Cyclic, unipolar square waveforms were used for this measurement.

CHAPTER 4 COOPERATIVE STRAIN ACCOMMODATION AND HIGH TEMPERATURE PIEZOELECTRIC COEFFICIENTS IN SOFT DOPED PZT

It is well established that the value of the piezoelectric coefficient reaches a maximum around the morphotropic phase boundary.¹⁶ As outlined in section 1.7.1 several mechanisms have been proposed to explain the enhanced piezoelectric coefficient of PZT at the MPB. In this work, results are shown in the classic PZT system that evidence unexpectedly high piezoelectric coefficient values at elevated temperatures for Zr:Ti ratios far away from the MPB. Specifically, it is shown that incorporation of 2 at% Sm into the crystal structure of PZT alters its ferroelectric to paraelectric phase transition character and gives rise to high temperature piezoelectric coefficients up to 915 pm/V, values that are approximately twice those measured in other donor substitution schemes (e.g., 477 pm/V for Nb and 435 pm/V for La). High-resolution X-ray diffraction from a synchrotron source is used to study the structural changes that occur during the ferroelectric to paraelectric phase transitions of doped PZT. These results show that the cubic phase begins to form approximately 50°C below the Curie temperature in Sm-doped PZT, whereas Nb, the cubic phase forms at the Curie temperature in and La-doped PZT. The effect of thermal cycling on the temperature-dependent piezoelectric coefficients of these doped PZT compositions is also studied, and provides insight into the nature of the origin of the effect.

4.1 High Piezoelectric Coefficients in PZT

A piezoelectric material is one that generates a voltage in response to a mechanical strain and vice versa. This electromechanical coupling effect makes piezoelectric materials the pervasive electroactive material used in the transducer industry.¹¹ The solid solution of lead zirconate titanate (PZT), $\text{PbZr}_{(1-x)}\text{Ti}_x\text{O}_3$,^{15,71} has

been the most commonly used commercial piezoelectric material for the last 50 years due to the high piezoelectric coefficients.^{11,72} A large body of work has been aimed at understanding the origin of the high piezoelectric response in PZT. It is generally accepted that high piezoelectric properties are obtained in PZT by donor doping^{16,41,62} and by using a Zr:Ti ratio in the region of the morphotropic phase boundary (MPB).^{16,73}

In the present work, the effect of three donor dopants on the temperature dependent piezoelectric coefficient of tetragonal PZT is studied. The dopants studied are Sm and La (A-site dopants), and Nb (B-site dopant). These dopants are known as donor dopants and yield a ferroelectric behavior classified as "soft" as described in Section 1.9. We show that, unlike the other dopants studied, Sm alters the ferroelectric tetragonal to paraelectric cubic phase transition characteristics in PZT. It also gives rise to a piezoelectric coefficient approximately double that of La and Nb-doped PZT.

4.2 Experimental

PZT 50:50, PZT 45:55, and PZT 40:60 compositions were doped with either 2 atomic percent of Sm, La or Nb. The chemical formulae of the doped materials are $\text{Pb}_{0.97}\text{Sm}_{0.02}\text{Zr}_{0.5}\text{Ti}_{0.5}\text{O}_3$, $\text{Pb}_{0.97}\text{Sm}_{0.02}\text{Zr}_{0.45}\text{Ti}_{0.55}\text{O}_3$, $\text{Pb}_{0.97}\text{Sm}_{0.02}\text{Zr}_{0.4}\text{Ti}_{0.6}\text{O}_3$, $\text{Pb}_{0.97}\text{La}_{0.02}\text{Zr}_{0.5}\text{Ti}_{0.5}\text{O}_3$, $\text{Pb}_{0.97}\text{La}_{0.02}\text{Zr}_{0.45}\text{Ti}_{0.55}\text{O}_3$, $\text{Pb}_{0.97}\text{La}_{0.02}\text{Zr}_{0.4}\text{Ti}_{0.6}\text{O}_3$, $\text{PbZr}_{0.485}\text{Ti}_{0.485}\text{Nb}_{0.02}\text{O}_3$, $\text{PbZr}_{0.439}\text{Ti}_{0.536}\text{Nb}_{0.02}\text{O}_3$, and $\text{PbZr}_{0.385}\text{Ti}_{0.585}\text{Nb}_{0.02}\text{O}_3$. Disc shaped pellets, with 10 mm diameter and 1.5 mm thickness, of all the compositions were produced using the conventional solid state synthesis techniques outlined in section 2.1. Silver paste was applied to the flat surfaces as electrodes, and the samples were then fired at 550°C for 30 min. The samples were electrically poled to saturation by applying an electric field just below the breakdown field of the material. The poled disc samples were used for both d_{33} and $\epsilon_{r,33}$ measurements. All samples were aged for

at least one week at room temperature prior to the measurements in order to mitigate the potential effects of initial aging on ferroelectric behavior.⁷⁴

The temperature dependant d_{33} was measured using a custom built apparatus based on Doppler vibrometry.^{45,46} A sinusoidal voltage of ± 10 V at a frequency of 1 kHz was used as an input signal. $\epsilon_{r,33}$ was measured by an LCR meter using a small input voltage of frequency 1 kHz. This is a typical frequency at which piezoelectrics are used for several applications such as actuation, transduction and vibration control. {Mokry, #437} The sample was placed in a furnace and heated at a ramp rate of $\approx 2^\circ\text{C}/\text{min}$ during both the d_{33} and $\epsilon_{r,33}$ measurements.

For the high resolution XRD measurements, the sintered disc shaped pellets were crushed into a fine powder. The powder was annealed at 600°C for 3 h in a closed alumina crucible to alleviate residual intragranular stresses. High resolution XRD patterns were measured on beamline 11-BM of the Advanced Photon Source at Argonne National Laboratory. A monochromatic X-ray beam with a wavelength of 0.412956 \AA and a 2θ range of 0° - 20° with a 2θ step size of 0.0001° . The sample powders were packed into a 0.3 mm diameter quartz capillary and spun at 60 Hz about the axis of the capillary to increase powder averaging. The samples were heated from room temperature to 500°C at a ramp rate of $2^\circ\text{C}/\text{min}$. XRD patterns were measured for 30 min at six fixed temperatures on cooling in the following order: 500°C , 360°C , 332°C , 308°C , 290°C and 250°C .

4.2 Variation of Piezoelectric and Dielectric Properties as a Function of Temperature in Sm, La and Nb doped PZT

The measurements of d_{33} , $\epsilon_{r,33}$ in all compositions as a function of temperature are shown in Figure 4-1. For all Zr:Ti ratios, the d_{33} of the Sm, La and Nb-doped

increases with increasing temperature until $\approx 250^\circ\text{C}$. Above this temperature, the behavior of the Sm-doped compositions differs greatly from that of the La and Nb-doped compositions. In the La and Nb doped compositions, the increase in d_{33} with temperature continues more rapidly after $\approx 250^\circ\text{C}$, until the maximum d_{33} is reached. The Sm-doped compositions show a stronger temperature dependence of d_{33} from $\approx 250^\circ\text{C}$ until the maximum d_{33} value is reached than that demonstrated by the La and Nb-doped compositions. For each respective Zr:Ti ratio, the maximum d_{33} observed in Sm modified PZT is roughly twice that observed in either the La or the Nb modified materials.

The effects of thermal history on this behavior were also explored. Heating the PZT compositions from room temperature to depoling temperature is referred to here as a thermal cycle. After thermal cycling, Sm doped PZT 50:50 was again poled to saturation and its d_{33} behavior as a function of temperature determined for a second time. As shown in Figure 4-2, the maximum d_{33} observed during the second thermal cycle is 583 pm/V. This is ≈ 332 pm/V lower than that obtained during the first thermal cycle. However, it is still higher than the maximum d_{33} observed in La doped PZT 50:50 (435 pm/V) and Nb doped PZT 50:50 (475 pm/V) during the first thermal cycle. After the completion of the second thermal cycle, Sm-doped PZT 50:50 was poled to saturation for a third time and its d_{33} behavior as a function of temperature was again measured. The maximum d_{33} observed during the third thermal cycle is 438 pm/V. The maximum d_{33} observed during the third thermal cycle is ≈ 477 pm/V lower than that observed during the first thermal cycle. This value is still higher than the maximum d_{33} observed in

La-doped PZT 50:50 and is approximately equal to the maximum d_{33} observed in Nb-doped PZT 50:50 during the first thermal cycle.

4.3 Temperature Dependent Structural Changes in Sm, La and Nb doped PZT

To obtain an insight into the structural changes taking place in the materials as a function of temperature, high resolution synchrotron XRD patterns of the Sm, La and Nb doped PZT 50:50 were measured at 500°C, 360°C, 332°C, 308°C, 290°C and 250°C. A selected region of the XRD patterns containing the (002) and (200) reflections of the materials are shown in Figure 4-3. With increasing temperature, the (002) and (200) reflections of the ferroelectric tetragonal phase become closer together and finally merge into a single (002) reflection above the Curie temperature.¹⁶ At 332°C, some extra intensity is observed between the (002) and (200) reflections in the Sm doped composition. This is highlighted using a magnified view in Figure 4-4.

The data presented in Figure 4-4 suggests that a single tetragonal phase insufficiently describes the diffraction pattern of Sm doped PZT 50:50 at 332°C due to the presence of an additional polymorph. In addition to the tetragonal phase, the other phases that have been previously observed in the PZT phase diagram are rhombohedral, monoclinic and cubic.⁷³ From the phase diagram, it can be seen that for PZT 50:50 the rhombohedral phase becomes less favorable at high temperatures. This reduces the probability that the second polymorph detected at 332°C is rhombohedral. It is also unlikely that the second polymorph is monoclinic because the symmetry of ferroelastic crystal structures tend to increase with increasing temperature. As the extra intensity at 332°C appears between the (002) and (200) peaks and the rhombohedral and monoclinic phases have been eliminated as unlikely, the extra intensity may

suggest the presence of a cubic phase in addition to the tetragonal phase. The implications of a coexisting cubic phase are further explored in Section 4.4.

In order to quantify the phase fraction of the cubic phase present in $\text{Pb}_{0.97}\text{Sm}_{0.02}\text{Ti}_{0.5}\text{Zr}_{0.5}\text{O}_3$ at 332°C, crystallographic refinement of the diffraction patterns was undertaken using the Rietveld refinement program GSAS.⁷⁶ In all the refinements, 12 background parameters in the shifted Chebyshev model were used. A combination of profile functions 3 and 4 were utilized. Profile function 4 includes the Stephens model for asymmetry⁷⁷ which was used to model the asymmetric peak shapes particularly in the refinements using the tetragonal space group. The parameters refined were the 2θ zero, scale factor, lattice parameters, atomic positions in the tetragonal phase, and isotropic displacement parameters. For all refinements, Zr and Ti were constrained to the same atomic position and displacement parameter. In addition, Sm and Pb were both constrained to the (0,0,0) atomic position, and the same isotropic displacement parameter. Sections of the measured and modeled diffraction pattern resulting from the final refined values of $\text{Pb}_{0.97}\text{Sm}_{0.02}\text{Ti}_{0.5}\text{Zr}_{0.5}\text{O}_3$ to a mixed phase model consisting of both the tetragonal $P4mm$ and cubic $Pm\bar{3}m$ phases at 332°C are shown in Figure 4-5. Using the phase fraction calculation described by Hill et al.⁷⁸, it was found that the phase fraction of the cubic phase in $\text{Pb}_{0.97}\text{Sm}_{0.02}\text{Ti}_{0.5}\text{Zr}_{0.5}\text{O}_3$ at 332°C is 31%. A summary of the refinement results is available in Table 4-1.

At 250°C and 290°C, the diffraction patterns were successfully modeled using a single tetragonal phase. The diffraction patterns recorded at 308°C and 332°C were modeled using different combinations of cubic and tetragonal phases as the asymmetry in the 002 and 200 reflections indicated the presence of a mixed phase. The diffraction

patterns collected at 360°C and 500°C were modeled using a cubic phase as no peak splitting was observed in the {00 l } type reflections.

4.4 Discussion

Sm doping results in high temperature piezoelectric coefficients that are extremely large. At temperatures above 250°C, the d_{33} of Sm-doped PZT shows a stronger temperature dependence than the d_{33} of La and Nb-doped PZT. The maximum d_{33} observed in the Sm-doped PZT compositions is approximately double that obtained by the other donor dopants, La and Nb. Previous explanations for the origin of very high piezoelectric coefficients at room temperature include: i) the existence of a lower symmetry monoclinic Cm phase¹⁷ or the presence of monoclinic symmetry within microdomains²⁴ and ii) the presence of ferroelectric nanodomains.⁷⁹ However, these effects are present in PZT materials with compositions at the MPB (Ti content \approx 47-50%) between the tetragonal and rhombohedral phases. As Sm doping gives rise to extremely high d_{33} values in PZT materials across a range of Zr:Ti ratios from 50:50 to 40:60, it is unlikely that MPB-related phenomena can fully account for the origin of the anomalously high d_{33} observed in the Sm PZT compositions.

The temperature dependence of d_{33} from \approx 250°C until the temperature at which the maximum d_{33} value is reached is greater in all the PZT compositions in this study than in the commercial composition used in the work done by Anton et al.⁴⁷ Once the values of d_{33} begin to drop, the rate of its decay is also greater in the PZT compositions used in this work. The d_{33} decays from its maximum value to zero over a temperature range of \approx 50°C in the commercial composition used by Anton et al.⁴⁷ In the present work, the decay takes place over a temperature range of approximately 3°C to 15°C and resembles the decay shown by BiNaTiO₃ in Anton et. al's work.⁴⁷ Less temperature

dependence in d_{33} during depoling has been associated with the existence of additional domain structures such as low symmetry nanopolar domains in PZT.⁷⁹ However, in the present work, the PZT compositions closer to the MPB (PZT 50:50) do not show a less rapid decay in temperature dependent d_{33} during depoling when compared to the compositions further away from the MPB (PZT 45:55 and PZT 40:60). This indicates that the presence of nanodomain structures may not be a sufficient explanation for the temperature dependent depoling behavior.

The contributions to piezoelectric and dielectric properties of polycrystalline ferroelectrics can be divided into two categories: intrinsic and extrinsic. The intrinsic response of a material is due to lattice and ionic displacements in the ferroelectric crystal and originates from the piezoelectric and dielectric responses of single domains. The extrinsic contributions to the material response are attributed to the presence of defect dipole, domain walls and other crystalline effects not associated with a perfect crystal.^{5,80} The total response of the material is determined by both the intrinsic and extrinsic responses. The intrinsic d_{33} and $\epsilon_{r,33}$ are related through the coefficient of electrostriction (Q_{11}) and spontaneous polarization (P_s) as per Eq. 4-1.²

$$d_{33} = 2\epsilon_{r,33}Q_{11}P_s \quad (4-1)$$

A peak in the d_{33} occurs at lower temperatures than the peak in $\epsilon_{r,33}$ for all the compositions. This implies that, for all the PZT compositions, the increase in d_{33} with increasing temperature is not due to an increase in intrinsic $\epsilon_{r,33}$. Also, the maximum value of $\epsilon_{r,33}$ in the Sm-doped compositions is smaller than the maximum $\epsilon_{r,33}$ values of the La and Nb-doped compositions across all the Zr to Ti ratios. From this, it may be inferred that the rapid increase in the temperature dependent d_{33} of the Sm-doped

composition above $\approx 250^\circ\text{C}$ is not due its intrinsic $\epsilon_{r,33}$ values increasing more rapidly with temperature relative to the La and Nb modified compositions.

The possibility that the valence of Sm changes from +3 to +2 at high temperatures is now considered. Sm^{+3} is a donor dopant. In its +2 state, Sm is an isovalent dopant. A major effect of isovalent doping is enhancement in permittivity.⁸¹ No atypical enhancement in permittivity is observed at temperatures above $\approx 250^\circ\text{C}$. Donor doping compensates for *p*-type conductivity usually assumed for PZT materials.⁸² As a consequence, if the valence of Sm changes from +3 to +2, it should result in an increase in conductivity and dielectric loss tangent. Figure 4-6 shows the dielectric loss tangent as a function of temperature for Sm, La and Nb-doped PZT. No increase in loss tangent that would indicate the presence of Sm^{+2} is observed. Furthermore, Sm^{+2} is unstable.⁸³ Thus, it is unlikely that the valence of Sm changes from +3 to +2 at high temperatures.

Extrinsic effects due to 90° domain wall motion are known contribute to enhanced piezoelectric coefficients at room temperature²² and have been shown to contribute up to 70% of d_{33} in PZT.^{22,51} They are now considered as a possible explanation for the behavior of the high temperature d_{33} in Sm-doped PZT. Tetragonal PZT has two types of domain walls: 180° and 90° walls. It has been shown that the major extrinsic contribution to the piezoelectric coefficient under weak external driving fields, such as those applied during the measurement of d_{33} is from the motion of 90° domain walls. Due to the considerably steeper free energy wells, 180° walls can be considered as idle under weak fields and are therefore not able to induce sizeable changes in piezoelectric properties.¹ When the temperature increases, the energy

available for 90° domain wall motion increases exponentially according to the Arrhenius equation. As a result, it is possible that 90° domain wall motion increases rapidly at temperatures above the energy threshold of $\approx 250^\circ\text{C}$.

With increasing temperature, the c/a ratio of PZT has been known to decrease.¹⁶ This change in the structure may also facilitate domain wall mobility. As domain wall motion in the tetragonal ferroelectric phase causes strain in the material, the strain could also increase rapidly with temperature. Given that d_{33} is the strain in the material due to an applied voltage, it can also increase in the same manner. This strong temperature dependence of d_{33} is present until Sm-doped PZT depoles at temperatures close to the Curie temperature. The lower maximum d_{33} value observed with each subsequent thermal cycle in Figure 4-2 further suggests that the origin of the high temperature dependant d_{33} values observed in Sm-doped PZT is extrinsic in nature.

High piezoelectric coefficients have also been attributed to the coexistence of multiple phases.⁸⁴ The high coefficients in mixed-phase materials have been associated with mechanisms such as interphase boundary motion²⁷ (the motion of the interface between the phases) and the concept that materials containing multiple polymorphs can better accommodate strain by allowing for more overall deformation strain in polycrystalline aggregates.^{14,85} Interphase boundary motion has been shown to be frequency dependent.²⁷ It is unlikely to play a significant role in the kHz frequency range at which the piezoelectric coefficients were measured in this study. Thus, 90° domain wall motion is the most likely extrinsic contribution to the piezoelectric coefficient. From the high resolution XRD results in the present measurements, it is seen that the tetragonal and cubic phases coexist in Sm-doped PZT at temperatures approaching the

phase transition. The coexistence of the polymorphs in the Sm-doped PZT compositions enable them to have a larger capacity to enhance the strain from an increase in 90° domain wall mobility. As La and Nb doping do not result in a mixed phase material at high temperatures, the extent of 90° domain wall motion and the resulting strain is restricted. Consequently, temperature dependant d_{33} in La and Nb-doped PZT does not increase as rapidly as observed in Sm-doped PZT.

The crystallochemical reasons why the phase transition behavior of Sm-PZT may be different from that of Nb and La-doped PZT are now considered. In an ideal cubic perovskite, the ionic radius of the A site atom, r_A , is 1.49 Å. The ionic radius of La is 1.36 Å,⁸⁶ only 5% smaller than the ideal. However, the ionic radius of Sm is 1.24 Å,⁸⁶ which is 35% smaller than the ideal A site radius. The ideal radius of the B site atom in the ideal cubic perovskite structure, r_B , is 0.605 Å. The ionic radius of Nb is 21% smaller than this.⁸⁶ When a dopant atom replaces a host atom of a different size, it induces strain. This strain is known as internal strain or chemical pressure. As the ionic radius of Sm deviates most from the ideal values, the Sm-doped PZT compositions can be considered to have the most chemical pressure. This is relevant because PZT undergoes a phase transition from the tetragonal phase to the cubic phase with an increase in pressure.^{87,88} Ahart et al.¹⁴ suggest that the chemical pressure created due to doping varies monotonically with the pressure needed for phase transformation. For example, Zeches et al.⁸⁹ report the observation of strain induced phase transformation in BiFeO₃ perovskites. Chemical pressure driven phase transformation has been shown through first principle calculations in other materials systems as well.⁹⁰ The large magnitude of chemical pressure caused by Sm doping may cause the characteristics of

the tetragonal ferroelectric to cubic paraelectric phase transition to change and allow for the formation of a mixed tetragonal and cubic phase over a defined temperature range. The homogeneity of the distribution of the dopant in the PZT solid solution may also play a role in the magnitude of chemical pressure generated due to the mismatch in the ionic radii of the host and dopant atom. Moreover, it may affect the presence of two coexisting polymorphs.

For cubic and tetragonal phases to coexist, the phase transition is required to be of the first order. The order of the phase transition can be determined from the variation of inverse susceptibility as a function of temperature by calculation of the slopes of the inverse susceptibility curve in the linear region at the point of divergence. For a first order phase transition, the absolute value of the ratio of the slopes of the right and left regions is 0.25. The variation of inverse dielectric susceptibility as a function of temperature is shown in Figure 4-7, for Sm, La and Nb-doped PZT 50:50. The left and right linear regions at the point of divergence are plotted in Figure 4-8. The ratio of the slopes is given in Table 4-2, where it was found to be approximately 0.5 for all the doped PZT 50:50 compositions. This indicates that the phase transition is second order. The Gibbs free energy function used to compute the order of the phase transition is given in Eq. 4-2.

$$\Delta G = \frac{1}{2}\chi(T - \theta)P^2 + \frac{1}{4}\beta P^4 \quad (4-2)$$

ΔG is the change in Gibb's free energy, χ is dielectric susceptibility, T is temperature, θ is Curie temperature, P is polarization and β is a constant. However, Eq. 4-2 does not take into account chemical pressure and 90° domain wall motion.

Phenomenological calculations have shown that when extrinsic effects such as domain wall motion are taken into consideration, the nature of the ferroelectric to paraelectric phase transition in PZT is of the first order.⁹¹

These results suggest that cooperative strain accommodation between the tetragonal and cubic polymorphs of Sm-doped PZT gives rise to the strong temperature dependence in its piezoelectric coefficient. This puts forward yet another mechanism that can be exploited to obtain large piezoelectric coefficients in the PZT system. Sm-doped PZT exhibits cooperative strain accommodation and as a result, has piezoelectric coefficients that are two times greater than that of La and Nb-doped PZT.

4.5 Conclusions

The behavior of d_{33} as a function of temperature was studied for Sm, La and Nb-doped PZT across a range of Zr:Ti ratios in order to understand the impact of chemical substitution on the high temperature piezoelectric coefficients of donor doped PZT. It was found that Sm results in high temperature piezoelectric coefficients that are twice those obtained by doping with La and Nb across all the Zr:Ti ratios studied. It is shown that intrinsic ϵ_{r33} and MPB-related effects cannot account for the anomalous behavior demonstrated by the Sm-doped PZT compositions. A theory to explain the origin of the high d_{33} values of Sm-doped PZT is proposed. It is suggested that Sm doping gives rise to the most internal strain or chemical pressure in PZT as, relative to La and Nb, the ionic radius of Sm deviates most from the ideal value for a cubic perovskite. This large internal stress in Sm changes the ferroelectric to paraelectric phase transitions characteristics in Sm-doped PZT and allows for a mixed tetragonal and cubic phase to form at temperatures below the Curie temperature. Due to the presence of the mixed phase, Sm-doped PZT compositions have higher strain accommodation capacities

compared to their La and Nb counterparts. With increasing temperature, the energy available for 90° domain wall motion increases exponentially for all the PZT compositions. However, the Sm-doped PZT compositions have a larger capacity to accommodate strain from an increase in 90° domain wall mobility. Hence, the Sm-doped compositions have high temperature piezoelectric coefficients that are roughly twice those obtained by doping with La and Nb. Thermal cycling studies further reinforce that the origin of the high d_{33} in Sm-doped PZT is extrinsic in nature.

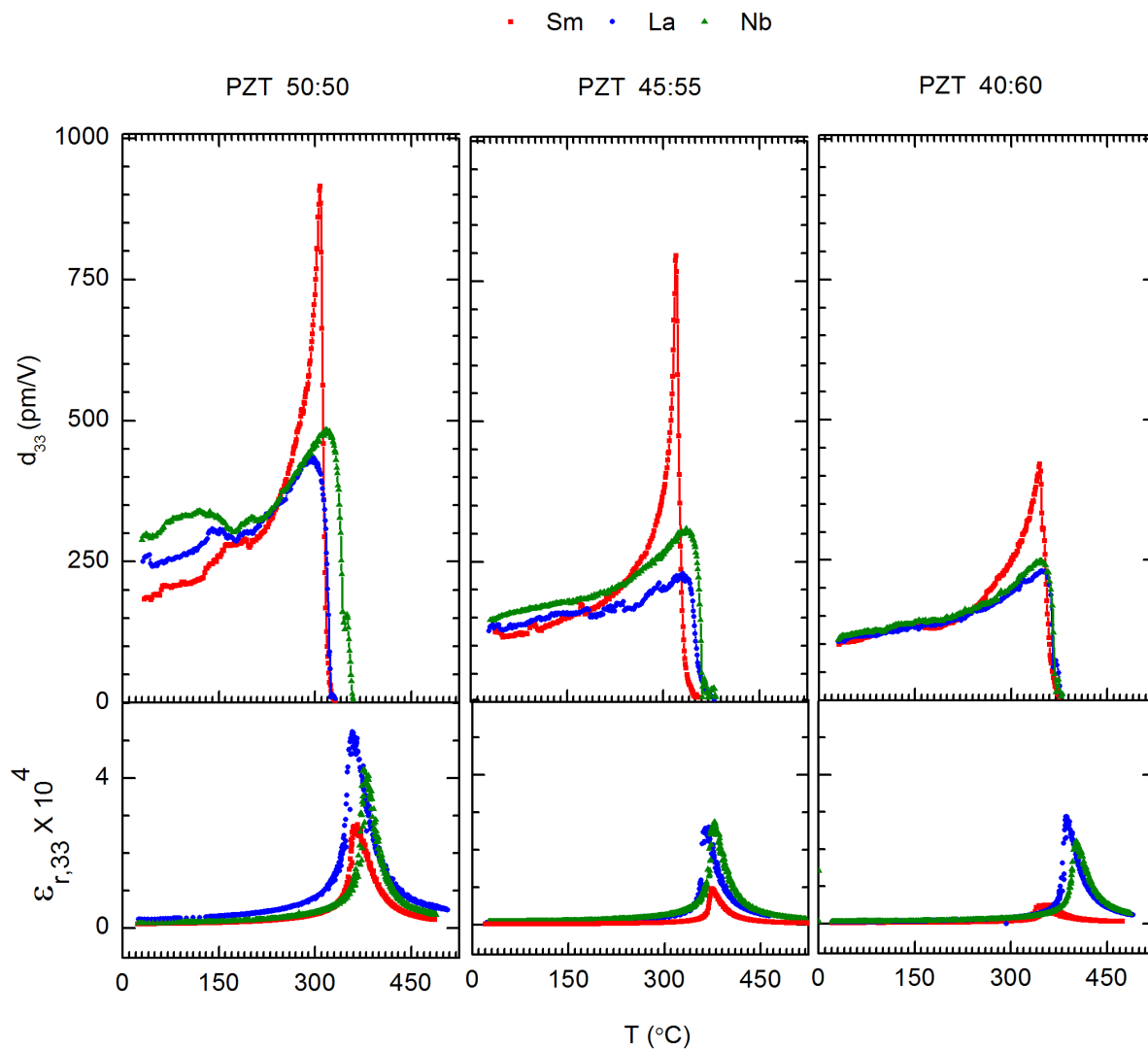


Figure 4-1. Variation of d_{33} and $\epsilon_{r,33}$ as a function of temperature for various PZT compositions.

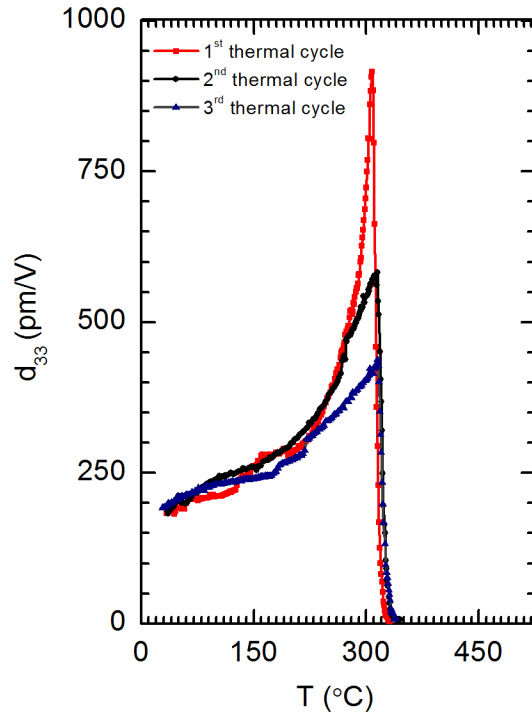


Figure 4-2. Behavior of d_{33} as a function of temperature during the first, second and third thermal cycles for 2 at% Sm PZT 50:50.

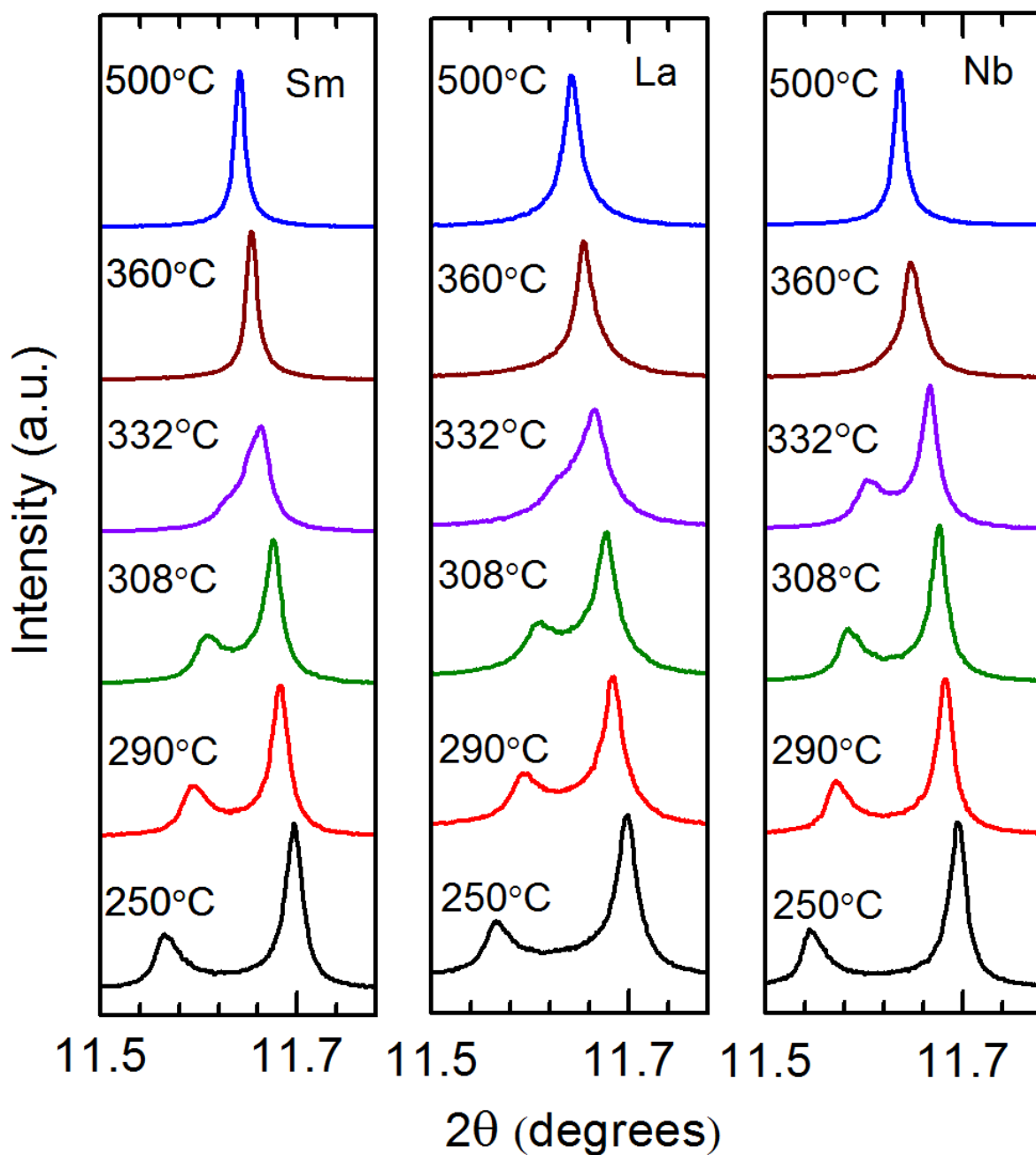


Figure 4-3. Selected regions of high resolution synchrotron XRD patterns showing the (002) and (200) type reflections for Sm, La and Nb-doped PZT 50:50.

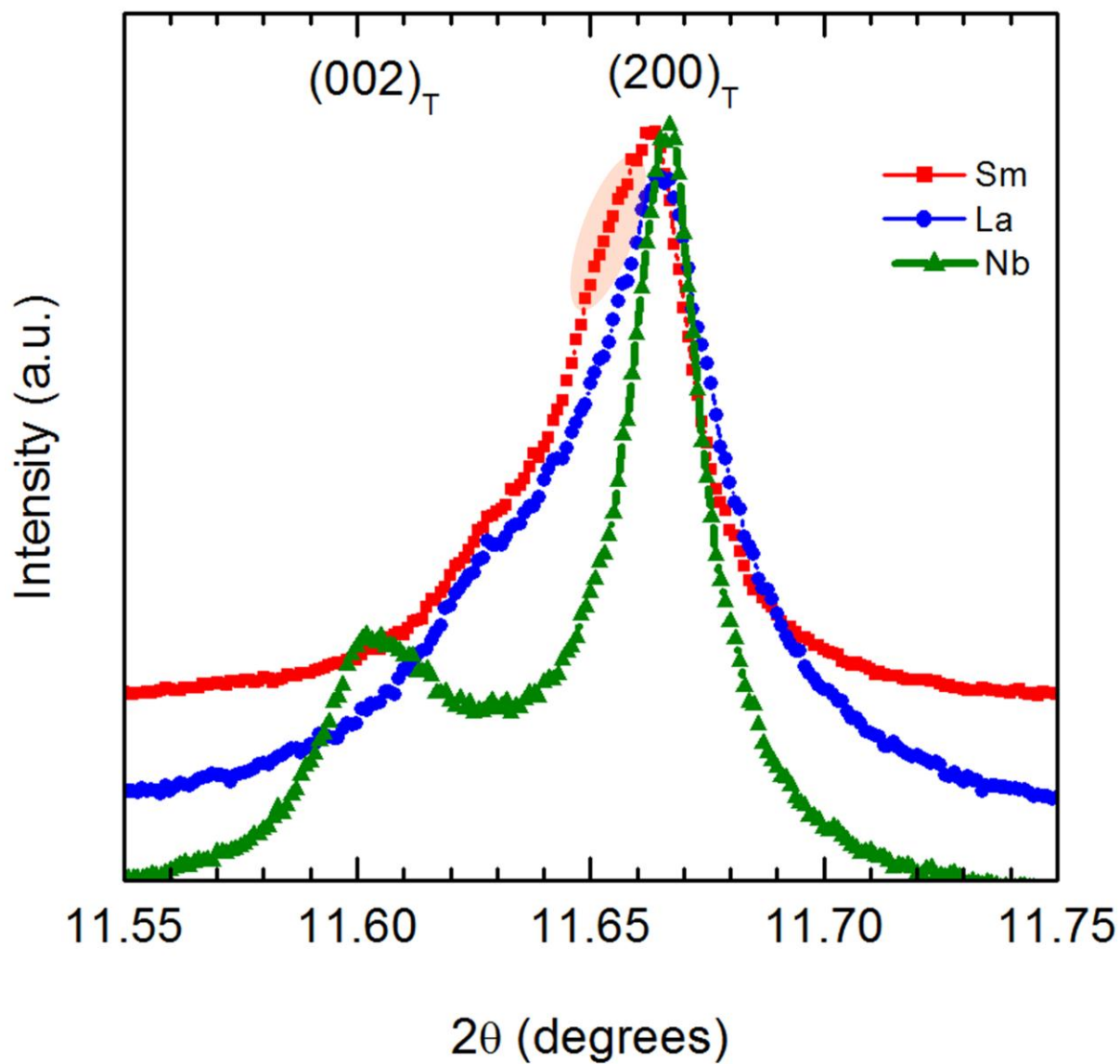


Figure 4-4. Magnified view of the (002) and (200) tetragonal reflections of Sm, La and Nb-doped PZT 50:50 at 332°C. The extra reflection not belonging to the tetragonal phase in Sm-doped PZT is highlighted in pink.

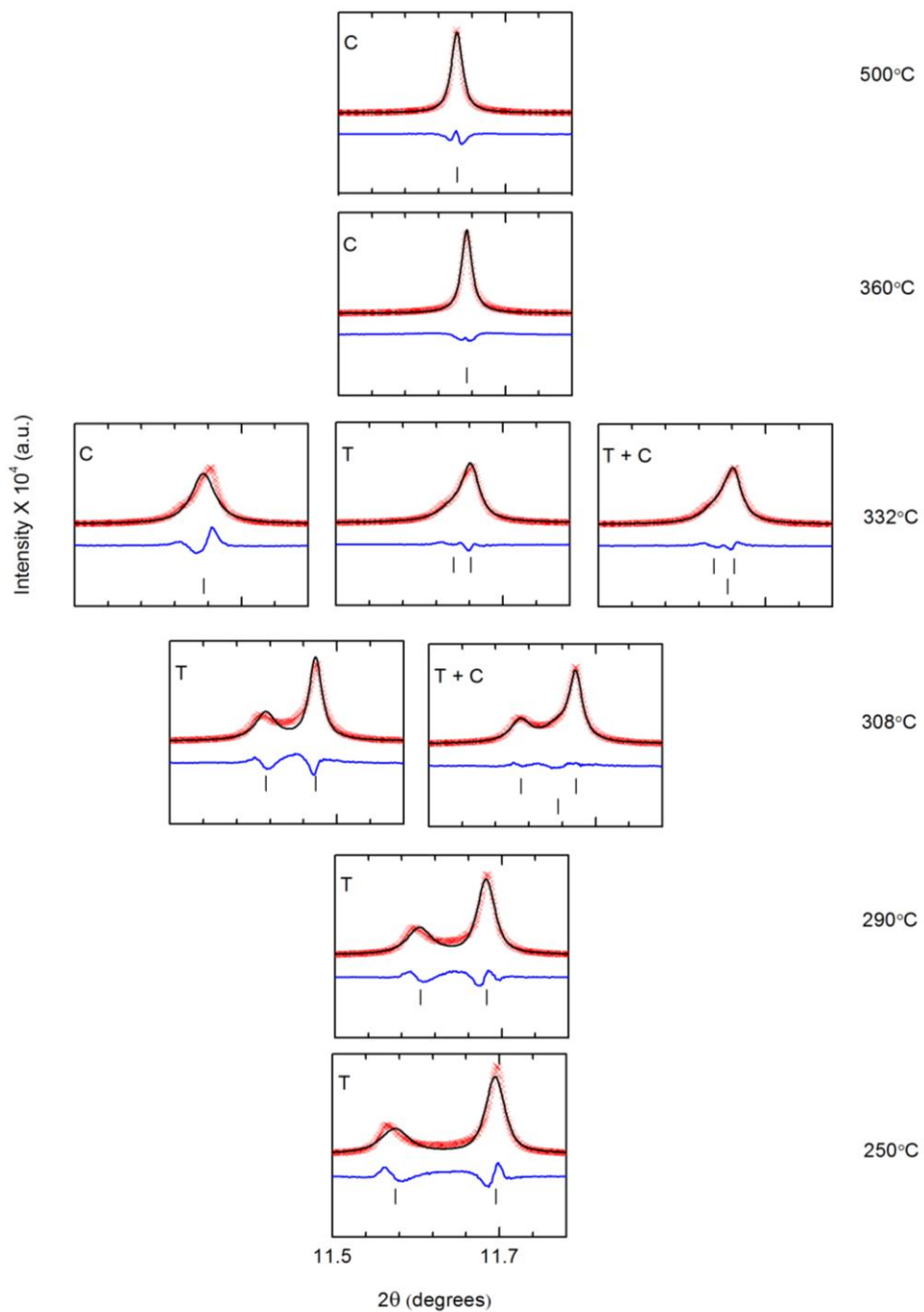


Figure 4-5. Rietveld refinements of 2 at % Sm-doped PZT 50:50 fit to a cubic model (332°C, 360°C, 500°C), tetragonal model (250°C, 290°C, 308°C, 332°C) and a mixed phase model consisting of the tetragonal $P4mm$ and cubic $Pm\bar{3}m$ phases (308°C, 332°C).

Table 4-1. Summary of Rietveld refinement results. The standard deviations for phase fraction are of the order of 0.1%.

Temperature (°C)	Space group	Phase fraction	a (Å)	c (Å)	Criteria of fit
250	<i>P4mm</i>	100%	4.054075(24)	4.095974(32)	$R_p = 9.00\%$ $R_{wp} = 11.20\%$ $\text{Chi}^2 = 2.804$
290	<i>P4mm</i>	100%	4.058846(20)	4.086615(26)	$R_p = 8.43\%$ $R_{wp} = 10.25\%$ $\text{Chi}^2 = 2.388$
308	<i>P4mm</i> <i>Pm$\bar{3}m$</i>	71% 29%	4.060155(15) 4.067567(23)	4.083100(21)	$R_p = 5.40\%$ $R_{wp} = 6.65\%$ $\text{Chi}^2 = 1.005$
332	<i>P4mm</i> <i>Pm$\bar{3}m$</i>	69% 31%	4.065098(15) 4.067787(22)	4.073675(34)	$R_p = 5.70\%$ $R_{wp} = 7.11\%$ $\text{Chi}^2 = 1.176$
360	<i>Pm$\bar{3}m$</i>	100%	4.067774(12)		$R_p = 8.64\%$ $R_{wp} = 10.54\%$ $\text{Chi}^2 = 2.648$
500	<i>Pm$\bar{3}m$</i>	100%	4.072079(10)		$R_p = 7.59\%$ $R_{wp} = 8.8\%$ $\text{Chi}^2 = 1.1901$

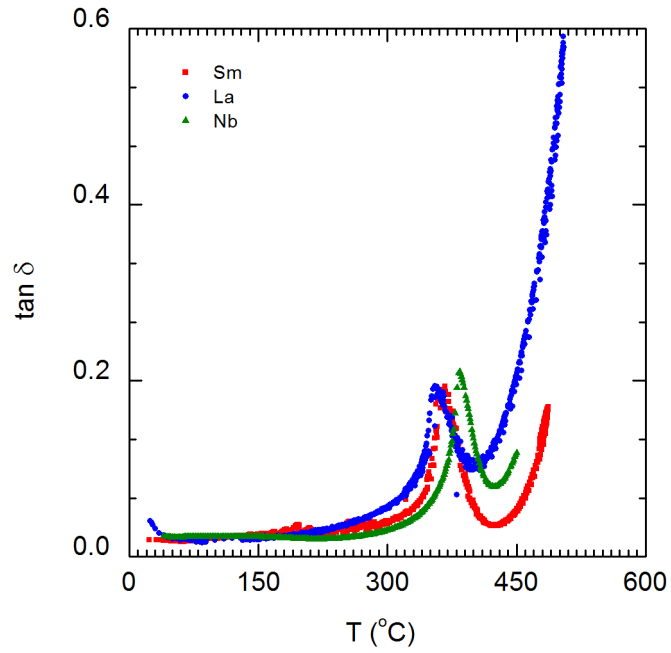


Figure 4-6. Variation of the dielectric loss tangent as a function of temperature for various PZT compositions.

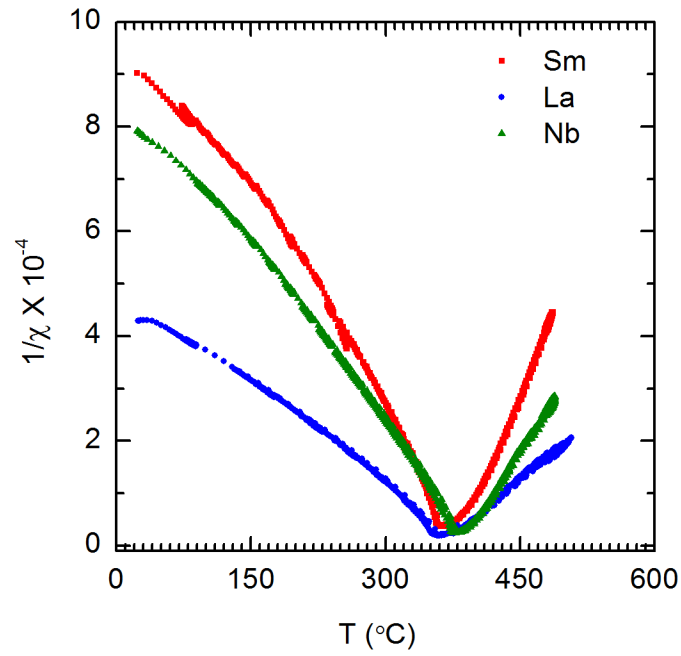


Figure 4-7. Inverse dielectric susceptibility as a function of temperature for 2 at% Sm, La and Nb-doped PZT 50:50.

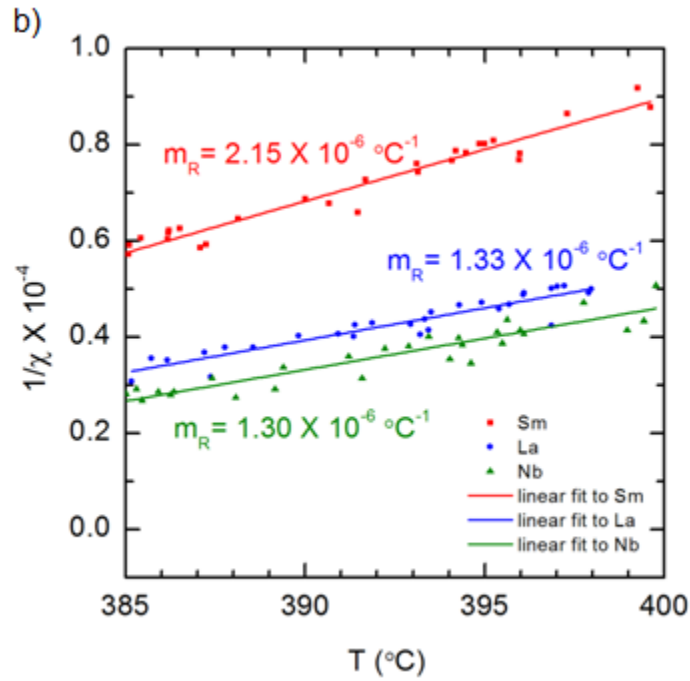
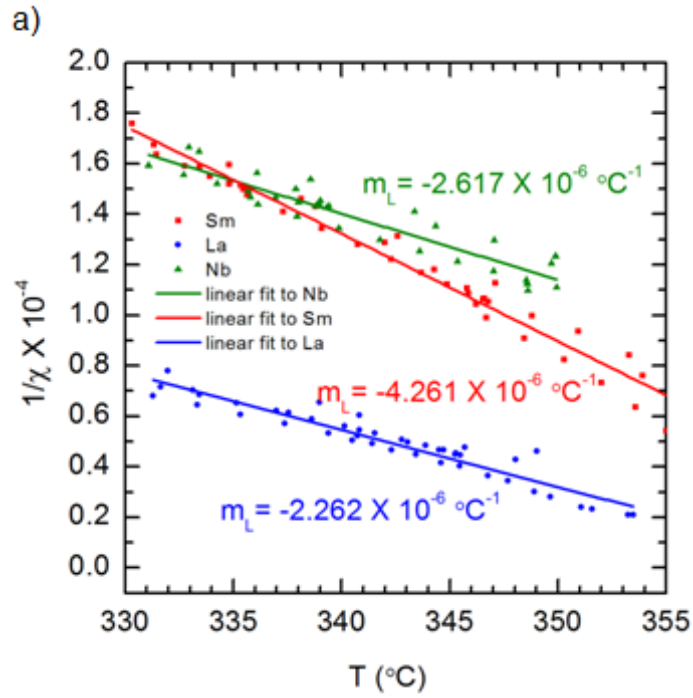


Figure 4-8. Linear fits to the a) left, and b) right linear regions at the point of divergence of inverse susceptibility plotted for 2 at% Sm, La and Nb PZT 50:50.

Table 4-2. Ratio of the slopes of the linear fits to the left and right regions of inverse susceptibility at the point of divergence.

Material	$m_R/-m_L$
2 at % Sm-doped PZT 50:50	0.5
2 at % La-doped PZT 50:50	0.5
2 at % Nb-doped PZT 50:50	0.6

CHAPTER 5 SUMMARY

In this work, new structural insight into the piezoelectric properties of PZT based ceramics was gained using synchrotron X-ray diffraction.

It was found that the soft dopants Sm, Nd, La and Nb have unique or signature effects on the strain mechanisms contributing to the extrinsic piezoelectric response of PZT. All the doped PZT 50:50 compositions show 90° domain reorientation during the application of both large and subcoercive electric fields. Only La and Nb-doped PZT 50:50 PZT show the presence of a mixed tetragonal and rhombohedral phase. Under weak electric fields, the interphase boundary between the tetragonal and rhombohedral phases moves in Nb-doped PZT and shows no response in La-doped PZT. The rhombohedral (200) lattice plane in Nb-doped PZT exhibits very large strains. The corresponding plane in the La-doped composition shows no strain response to electric fields.

Thus far, there has been no definitive information regarding how doping increases the piezoelectric coefficient in PZT. This work shows that different dopants soften PZT via distinctive mechanisms and that the value of the piezoelectric coefficient achieved through chemical substitution depends on the magnitude and number of strain mechanisms that are accessible to the doped material.

The effect of doping schemes on the temperature dependent piezoelectric response was also examined. Sm results in high temperature piezoelectric coefficients that are roughly twice those obtained by doping with La and Nb across all the Zr:Ti ratios studied. It was found that the ferroelectric-paraelectric phase transformation characteristics of PZT based ceramics are influenced by doping. At temperatures

approaching the Curie temperature, Sm-doped PZT 50:50 is composed of a mixed tetragonal and cubic phase whereas La and Nb-doped PZT are composed of a single tetragonal phase. It is hypothesized that the origin of the large piezoelectric coefficient values shown by Sm-doped PZT at high temperatures is extrinsic in nature. Due to the presence of the mixed phase, Sm-doped PZT compositions possess higher strain accommodation capacities when compared to the La and Nb compositions. With increasing temperature, the energy available for 90° domain wall motion increases for all the PZT compositions. However, the Sm-doped PZT compositions have a larger capacity to enhance the strain from an increase in 90° domain wall mobility. Hence, the Sm-doped compositions have high temperature piezoelectric coefficients that are approximately twice those obtained by doping with La and Nb.

PZT has been extensively studied in the past in order to understand the origin of its electromechanical properties. The insight into strain mechanisms developed in this work contributes to the understanding of the enhanced piezoelectric properties of soft doped PZT materials.

PZT ceramics are extensively used in several industries. In recent years, considerable research has been undertaken towards the development of new generations of Pb based and Pb free materials with higher electromechanical properties. The understanding of specific strain mechanisms that have been studied in this dissertation can be exploited in order to facilitate these advancements. By adjusting the composition of the piezoelectric material, an attempt can be made to induce whichever strain mechanisms are required for the purpose of obtaining the optimal longitudinal piezoelectric coefficients in various materials systems. Three of the strain

mechanisms (90° domain wall motion, coexistence of mixed ferroelectric phases and interphase boundary motion) are enhanced close to the MPB. The strain capability of the rhombohedral (200) plane may not be affected by the proximity to an MPB. Strain enhancements due to the coexistence of a mixed phase (only one of the phases needs to be ferroelectric) can be used to enhance the piezoelectric coefficient in systems that are not proximate to a MPB. Thus, this work contributes towards the understanding of the process by which the piezoelectric coefficient is enhanced by softening.

CHAPTER 6 FUTURE WORK

The results presented in the present dissertation reveal new insight into electric-field-induced and temperature dependent strain mechanisms of ferroelectric compositions. Several future areas of study are natural extensions of the present work. These new possible directions of research will enable a better understanding of the strain mechanisms that contribute to softening in donor doped PZT. These research directions are presented in Sections 6.1-6.5.

6.1 Measurement of the Temperature Dependent Crystallographic Response During the In Situ Application of Electric Fields

In the present work, the crystallographic structure of the Sm, La and Nb-doped PZT 50:50 was studied at 6 fixed temperatures. In order to obtain a better understanding of the temperature dependent strain mechanisms in this material, it would be of interest to study the temperature dependent crystallographic response of these compositions during the in situ application of an electric field. If these measurements were carried out across temperatures ranging from room temperature to temperatures above T_c , the effect of the various soft dopants on the depoling behavior of the PZT compositions can also be studied.

6.2 Frequency Dependence of the Piezoelectric Response

The strain mechanisms observed in this study are frequency dependent. It would be beneficial to compare the frequency dependence of the macroscopic polarization, strain, relative permittivity and longitudinal piezoelectric coefficient to the frequency dependence of the strain mechanisms observed using diffraction.

6.3 Effect of Dopant Homogeneity

As a relatively small percent of the A or B-site atoms are dopant atoms (2%), it is possible that the dopants are not homogeneously distributed throughout the PZT solid solution. Dopant homogeneity may affect the phase transformations observed in this work. Namely, the likely strain-driven phase transformation in Sm-doped PZT at high temperatures described in Section 4 and the electric field driven phase transformation in Nb-doped PZT described in Sections 3.4.2 and 3.4.3. It would be valuable to study dopant distribution in the PZT compositions using EDS mapping in a TEM or SEM. The effects of processing time, processing temperature and annealing conditions on dopant homogeneity can also be studied.

6.4 Measurements on Undoped PZT Compositions

It would be beneficial to repeat all the measurements done in this work and suggested for the future work with an undoped PZT composition in order to better compare the effect of soft doping on the strain mechanisms in undoped PZT.

6.5 Effect of the Ionic Radius of the Dopant on the Ferroelectric-Paraelectric Phase Transition

Results discussed in Chapter 4 suggest that the internal strain due the mismatch between the ionic radii of the dopant, Sm and the host, Pb provides an additional driving force for the ferroelectric tetragonal to paraelectric cubic phase transformation in Sm-doped PZT. It would be valuable to ascertain if there are other dopants that can similarly cause the cubic phase to coexist with the tetragonal phase below the Curie temperature. Nd doping on the A-site is an option that can be explored in this regard.

APPENDIX
DETERMINATION OF THE CONTRIBUTION OF 90° DOMAIN WALL MOTION TO
LONGITUDINAL STRAIN

When a poled polycrystalline material is subjected to subcoercive electric field cycles, 90° domain walls in grains of all orientations respond to the applied electric field. The total longitudinal strain in the material due to all the 90° domain wall motion is obtained by projecting the anisotropic strains of all the crystalline orientations to the longitudinal direction and performing a weighted summation of the projected strains as described in Pramanick et al.⁴² The experimental data needed for the determination of the overall contribution of 90° domain walls to the macroscopic longitudinal strain are time-resolved diffraction patterns measured at all angles with respect to the electric field direction. Here, a more efficient method of data measurement that requires a time-resolved diffraction pattern to be taken at only one angle (parallel to the electric field) with respect to the electric field is developed based on known behaviors of domain wall motion.

90° domain wall motion results in a conservative interchange in symmetry dependent reflections. The fraction of c-axis domains that are oriented in a specific sample direction can be calculated from the {002} diffracted intensities by using the equation⁶³

$$\eta_{002} = \frac{\frac{I_{002}}{I_{002}^{\text{unpoled}}}}{\frac{I_{002}}{I_{002}^{\text{unpoled}}} + 2 \left(\frac{I_{200}}{I_{200}^{\text{unpoled}}} \right)} - \frac{1}{3} \quad (\text{A-1})$$

where I_{ijk} is the integrated intensity of the (002) and (200) peaks in both the state of interest and the unpoled state. During the electric field cycling, the fraction of c-axis

domains that are re-oriented in a specific sample direction, $\Delta\eta_{002}$, is expressed relative to the maximum and minimum values through,⁶³

$$\Delta\eta_{002} = \eta_{002}^+ - \eta_{002}^- \quad (\text{A-2})$$

where η_{002}^+ and η_{002}^- are the volume fraction of 002 domains oriented in a particular direction during the positive and negative electric field cycles respectively. As a random distribution of ferroelectric domains contains 1/3 of the 002 domain orientation, the multiple of a random distribution, f , of 002 domains is given by,⁶³

$$f = 3\eta_{002} \quad (\text{A-3})$$

f varies as a function of angle to the electric field, α .⁴² For the purposes of determining $d_{33,90^\circ}$, the values of $f(\alpha)$ are needed across the range $0 < \alpha < \pi/2$.⁴² From known behaviors of domain wall motion,^{42,63,100} it was determined that the following equations can be used to model $f(\alpha)$:

$$f(\alpha) = 1 + A \cos 2\alpha \text{ for } 0 < \alpha < \frac{\pi}{4} \quad (\text{A-4})$$

$$f(\alpha) = 1 + \frac{A(\sqrt{2}-1)}{\sqrt{2}} \cos 2\alpha \text{ for } \frac{\pi}{4} < \alpha < \frac{\pi}{2} \quad (\text{A-5})$$

In the above equations, A is the experimentally determined value of $\Delta\eta_{002}$ at $\alpha = 0$. The relation between f and η_{002} is as given in equation (A-3). Equations (A-1) to (A-5), together with a time-resolved diffraction pattern measured at $\alpha = 0$, enable the calculation of $f(\alpha)$ from $0 < \alpha < \pi/2$. Figure A-1 shows the typical variation of $\Delta\eta_{002}$ as a function of α at various subcoercive electric field amplitudes for a La modified PZT material as measured experimentally. It also shows the values of α as modeled by equations (A-4) and (A-5). As can be seen from Figure A-1, equations (A-4) and (A-5) adequately describe the variation of $\Delta\eta_{002}$ as a function of α .

Let α and β be radial and azimuthal pole figure angles. If G is the volume of orientation space enclosing all possible c-axis directions of domains within the range of $0 < \alpha < \pi/2$ and $0 < \beta < 2\pi$, then,

$$G = \int_{\alpha=0}^{\pi/2} \int_{\beta=0}^{2\pi} \sin \alpha \, d\alpha d\beta \quad (\text{A-6})$$

Integrating f across all possible orientations gives⁹²

$$Z = \frac{1}{G} \int_{\alpha=0}^{\pi/2} \int_{\beta=0}^{2\pi} f(\alpha) \sin \alpha \, d\alpha d\beta \quad (\text{A-7})$$

As α and β are independent variables and G is the surface area of a hemisphere,

$$Z = \frac{1}{2\pi} \left(\int_{\alpha=0}^{\pi/2} f(\alpha) \sin \alpha \, d\alpha \right) \left(\int_{\beta=0}^{2\pi} d\beta \right) \quad (\text{A-8})$$

When Z is axisymmetric, equation (A-8) reduces to,

$$Z = \int_{\alpha=0}^{\pi/2} f(\alpha) \sin \alpha \, d\alpha \quad (\text{A-9})$$

Considering that α varies from 0 to $\pi/2$ (the values of f between π and $\pi/2$ are identical to its values between 0 and $\pi/2$), equation(A-9) further reduces to

$$Z = \int_{\alpha=0}^{\pi} f(\alpha) \sin \alpha \, d\alpha \quad (\text{A-10})$$

For an unpoled sample, i.e., a sample with a random distribution of domains, for all values of α ,

$$f = 1 \quad (\text{A-11})$$

Using (A-11) in (A-10) gives,

$$Z = \int_{\alpha=0}^{\pi/2} \sin \alpha \, d\alpha \quad (\text{A-12})$$

Integrating equation (A-12) gives,

$$Z = 1 \quad (\text{A-13})$$

Equating the right hand side (RHS) of equation (A-10) to the RHS of equation (A-13) gives,

$$\int_{\alpha=0}^{\pi/2} f \sin \alpha \, d\alpha = 1 \quad (\text{A-14})$$

As the total volume of domains is a constant, any function $f(\alpha)$ used to model domain orientations as a function of α has to obey equation (A-14).

To check the validity of using equations (A-4) and (A-5) to model $f(\alpha)$, equations (A-4) and (A-5) are substituted for $f(\alpha)$ in equation (A-14). If the evaluation of the integral on the left hand side (LHS) of (A-14) yields 1, then (A-4) and (A-5) follow conservation of domain volumes.

Substituting for f in (A-14) using equations (A-4) and (A-5) gives,

$$\int_{\alpha=0}^{\pi/4} (1 + A \cos 2\alpha) \sin \alpha \, d\alpha + \int_{\alpha=\pi/4}^{\pi/2} \left(1 + \frac{A(\sqrt{2}-1)}{\sqrt{2}} \cos 2\alpha\right) \sin \alpha \, d\alpha \quad (\text{A-15})$$

Integrating equation (A-15) gives,

$$1 - \frac{1}{\sqrt{2}} + \frac{A(\sqrt{2}-1)}{3} + \frac{1}{\sqrt{2}} - \frac{A\sqrt{2}(\sqrt{2}-1)}{3\sqrt{2}} \quad (\text{A-16})$$

Simplifying (A-16) gives the LHS of (A-14) to be 1. As the LHS of (A-14) equals the RHS of (A-14), when $f(\alpha)$ is given by (A-4) and (A-5), these equations are valid models to describe $f(\alpha)$ from 0 to $\pi/2$.

The variation of $\Delta\eta_{002}$ as a function of α was calculated for K350 using equations (A-4) and (A-5) and is shown in Figure A-2. The extent of 90° domain switching that occurs can be quantified and used to determine the longitudinal strain in the material due to 90° domain switching, ε_{90° , according to the equation⁴²

$$\varepsilon_{90^\circ} = \frac{c-a}{a} \int_0^{\pi/2} \Delta f(\alpha) \cos^2 \alpha \sin \alpha \, d\alpha \quad (\text{A-17})$$

where c and a are unit cell parameters, and Δf is difference between the initial and final MRD values of 002 domains oriented at a particular angle, α . Let $f^+(\alpha)$ be the MRD of the 002 domains in a poled sample subjected to the positive polarity of a subcoercive

bipolar electric field cycle. Let $f^-(\alpha)$ be the MRD of 002 domains in a poled sample subjected to the negative polarity of a subcoercive bipolar electric field. Then,

$$\varepsilon_{90^\circ} = \frac{c-a}{a} \left(\int_0^{\pi/2} f^+(\alpha) \cos^2 \alpha \sin \alpha \, d\alpha - \int_0^{\pi/2} f^-(\alpha) \cos^2 \alpha \sin \alpha \, d\alpha \right) \quad (\text{A-18})$$

Using (A-4) and (A-5) to substitute for $f^+(\alpha)$ and $f^-(\alpha)$ in (A-18) gives,

$$\begin{aligned} \varepsilon_{90^\circ} = & \frac{c-a}{a} \left(\int_0^{\pi/4} (1 + A^+ \cos 2\alpha) \cos^2 \alpha \sin \alpha \, d\alpha + \right. \\ & \int_{\pi/4}^{\pi/2} \left(1 + \frac{A^+ \sqrt{2}-1}{\sqrt{2}} \cos 2\alpha \right) \cos^2 \alpha \sin \alpha \, d\alpha - \\ & \int_0^{\pi/4} (1 + A^- \cos 2\alpha) \cos^2 \alpha \sin \alpha \, d\alpha - \\ & \left. \int_{\pi/4}^{\pi/2} \left(1 + \frac{A^- \sqrt{2}-1}{\sqrt{2}} \cos 2\alpha \right) \cos^2 \alpha \sin \alpha \, d\alpha \right) \quad (\text{A-19}) \end{aligned}$$

$$\Delta\eta_{002(\alpha=0)} = A^+ - A^- \quad (\text{A-20})$$

Integrating equation (A-19) and substituting for A^+ and A^- using (A-20) gives,

$$\varepsilon_{90^\circ} = 3 \frac{c-a}{a} \left\{ \frac{\Delta\eta_{002}}{15} \left(\frac{\sqrt{2}+1}{\sqrt{2}} \right) - \frac{\Delta\eta_{002}}{15\sqrt{2}} \left(\frac{\sqrt{2}-1}{\sqrt{2}} \right) \right\} \quad (\text{A-21})$$

Equation (A-21) was used to calculate ε_{90° from a single time resolved diffraction pattern measured at $\alpha = 0$. $\Delta\eta_{002}$ was obtained from the integrated (002) and (200) peak intensities as per equations (A-1) and (A-2). The modeled values of $\Delta\eta_{002}$ were also numerically integrated according to Equation (A-16) and as described in Pramanick et al.,⁹³ this value equals that obtained by using equation (A-20), providing additional validity to equation (A-20).

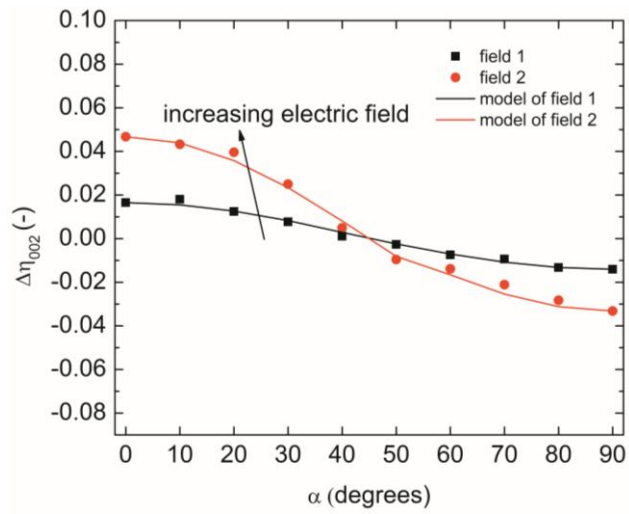


Figure A-1. Experimentally determined and modeled values of $\Delta\eta_{002}$ as a function of α at two subcoercive electric field amplitudes.

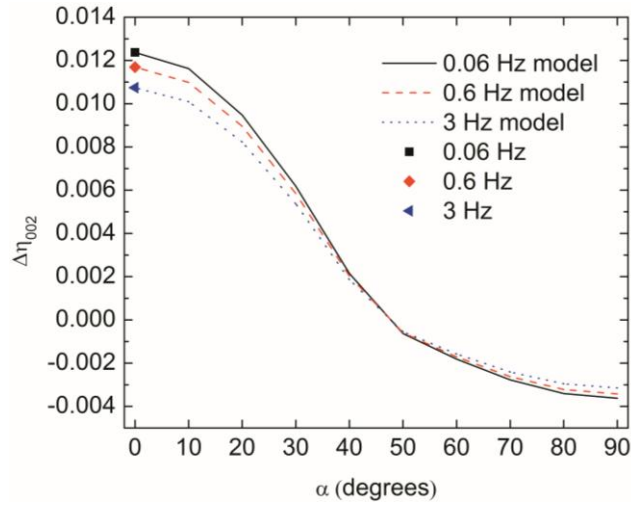


Figure. A-2. Variation of $\Delta\eta_{002}$ as a function of α for K350. The lines represent modeled values and the symbols represent experimentally measured data

LIST OF REFERENCES

- ¹Q. M. Zhang, H. Wang, N. Kim, and L. E. Cross, "Direct Evaluation of Domain Wall and Intrinsic Contributions to the Dielectric and Piezoelectric Response and Their Temperature Dependence on Lead Zirconate Titanate Ceramics," *J. Appl. Phys.*, **75** 454-9 (1994).
- ²N. Setter, *ABC of Piezoelectricity*. EPFL, Lausanne, Switzerland, 2002.
- ³M. W. Barsoum, *Fundamentals of Ceramics*. Taylor and Francis Group, New York, USA, 2003.
- ⁴D. Damjanovic, "Ferroelectric, Dielectric and Piezoelectric Properties of Ferroelectric Thin Films and Ceramics," *Rep. Prog. Phys.*, **61** [9] 1267-324 (1998).
- ⁵C. A. Randall, N. Kim, J.-P. Kucera, W. Cao, and T. R. Shrout, "Intrinsic and Extrinsic Size Effects in Fine-Grained Morphotropic-Phase-Boundary Lead Zirconate Titanate Ceramics," *J. Am. Ceram. Soc.*, **81** [3] 677-88 (1998).
- ⁶R. J. Nelmes and W. F. Kuhs, "The Crystal Structure of Tetragonal PbTiO₃ at Room Temperature and at 700 K," *Solid State Comm.*, **54** [8] 721-3 (1985).
- ⁷G. Bertotti and I. D. Mayergoyz, *The Science of Hysteresis*. Academic Press, Oxford, UK, 2006.
- ⁸M. E. Lines and A. M. Glass, *Principles and Applications of Ferroelectrics and Related Materials*. Oxford University Press, Oxford, UK, 2001.
- ⁹J. Fousek and V. Janovec, "The Orientation of Domain Walls in Twinned Ferroelectric Crystals," *J. Appl. Phys.*, **40** [1] 135-42 (1969).
- ¹⁰L. E. Cross, "Ferroelectric Ceramics: Tailoring Properties for Specific Applications," in *Ferroelectric Ceramics: Tutorial Reviews, Theory, Processing, and Applications*. Birkhäuser, University of California, USA, 1–86 (1993).
- ¹¹G. H. Haertling, "Ferroelectric Ceramics: History and Technology," *J. Am. Ceram. Soc.*, **82** [4] 797-818 (1999).
- ¹²J. F. Scott, "Applications of Modern Ferroelectrics," *Science*, **315** 954-9 (2007).
- ¹³D. Damjanovic and R. Newnham, "Electrostrictive and Piezoelectric Materials for Actuator Applications," *J. Intel. Mat. Syst. Str.*, **3** [2] 190-208 (1992).
- ¹⁴M. Ahart, M. Somayazulu, R. E. Cohen, P. Ganesh, P. Dera, H.-k. Mao, R. J. Hemley, Y. Ren, P. Liermann, and Z. Wu, "Origin of Morphotropic Phase Boundaries in Ferroelectrics," *Nature*, **451** 545-8 (2008).

- ¹⁵G. Shirane and A. Takeda, "Phase Transitions in Solid Solutions of Lead Zirconate and Lead Titanate (I) Small Concentrations of Lead Titanate," *J. Phys. Soc. Jpn.*, **7** [1] 5-11 (1952).
- ¹⁶B. Jaffe, W. Cook, and H. Jaffe, *Piezoelectric Ceramics*. Academic Press, San Diego, USA, 1971.
- ¹⁷B. Noheda, D. E. Cox, G. Shirane, J. A. Gonzalo, L. E. Cross, and S. E. Park, "A Monoclinic Ferroelectric Phase in the $\text{Pb}(\text{Zr}_{1-x}\text{Ti}_x)\text{O}_3$ solid solution," *Appl. Phys. Lett.*, **74** [14] 2059-61 (1999).
- ¹⁸D. Damjanovic, "Lead-Based Piezoelectric Materials" in *Piezoelectricity and Acoustic Materials for Transducer Applications*. A. Safari and E. K. Akdoğan (eds) Springer, New York, USA, 2008.
- ¹⁹E. Sawaguchi, "Antiferroelectricity and Ferroelectricity in Lead Zirconate," *J. Phys. Soc. Jpn.*, **7** [3] 336-7 (1952).
- ²⁰B. Jaffe, R. S. Roth, and S. Marzullo, "Piezoelectric Properties of Lead Zirconate-Lead Titanate Solid-Solution Ceramics," *J. Appl. Phys.*, **25** [6] 809-10 (1954).
- ²¹X. L. Zhang, Z. X. Chen, L. E. Cross, and W. A. Schulze, "Dielectric and Piezoelectric Properties of Modified Lead Titanate Zirconate Ceramics from 4.2 to 300 K," *J. Mater. Sci.*, **18** [4] 968-72 (1983).
- ²²A. Pramanick, D. Damjanovic, J. E. Daniels, J. C. Nino, and J. L. Jones, "Origins of Electro-Mechanical Coupling in Polycrystalline Ferroelectrics during Subcoercive Electrical Loading," *J. Am. Ceram. Soc.*, **94** [2] 293-309 (2011).
- ²³V. A. Isupov, "Phase Coexistence in Lead Zirconate Titanate Solid Solutions," *Phys. Solid State*, **43** [12] 2262-6 (2001).
- ²⁴K. A. Schönau, L. A. Schmitt, M. Knapp, H. Fuess, R.-A. Eichel, H. Kungl, and M. J. Hoffmann, "Nanodomain Structure of $\text{Pb}(\text{Zr}_{1-x}\text{Ti}_x)\text{O}_3$ at its Morphotropic Phase Boundary: Investigations from Local to Average Structure," *Phys. Rev. B*, **75** [18] 184117 (2007).
- ²⁵E. I. Bondarenko, V. Y. Topolov, and A. V. Turik, "The Role of 90° Domain Wall Displacements in Forming Physical Properties of Perovskite Ferroelectric Ceramics," *Ferroelectrics Lett.*, **13** [1] 13-19 (1991).
- ²⁶D. Damjanovic and M. Demartin, "Contribution of the Irreversible Displacement of Domain Walls to the Piezoelectric Effect in Barium Titanate and Lead Zirconate Titanate Ceramics," *J. Phys.: Condens. Matter*, **9** 4943-53 (1997).

- ²⁷J. L. Jones, E. Aksel, G. Tutuncu, T.-M. Usher, J. Chen, X. Xing, and A. J. Studer, "Domain Wall and Interphase Boundary Motion in a Two-Phase Morphotropic Phase Boundary Ferroelectric: Frequency Dispersion and Contribution to Piezoelectric and Dielectric Properties," *Phys. Rev. B*, **86** [2] 024104 (2012).
- ²⁸M. J. Haun, E. Furman, S. J. Jang, and L. E. Cross, "Thermodynamic Theory of the Lead Zirconate-Titanate Solid Solution System, V: Theoretical Calculations," *Ferroelectrics*, **99** [1] 63-86 (1989).
- ²⁹L. Bellaiche, A. Garcia, and D. Vanderbilt, "Finite-Temperature Properties of $\text{Pb}(\text{Zr}_{1-x}\text{Ti}_x)\text{O}_3$ Alloys from First Principles," *Phys. Rev. Lett.*, **84** [23] 5427-30 (2000).
- ³⁰G. Sághi-Szabó and R. E. Cohen, "Long-Range Order Effects in $\text{Pb}(\text{Zr}_{1/2}\text{Ti}_{1/2})\text{O}_3$," *Ferroelectrics*, **194** [1] 287-98 (1997).
- ³¹K. Carl and K. H. Härdtl, "Electrical After-Effects in $\text{Pb}(\text{Ti}, \text{Zr})\text{O}_3$ ceramics," *Ferroelectrics*, **17** [1] 473-86 (1977).
- ³²M. Budimir, D. Damjanovic, and N. Setter, "Piezoelectric Anisotropy-Phase Transition Relations in Perovskite Single Crystals," *J. Appl. Phys.*, **94** [10] 6753-61 (2003).
- ³³Y. Ishibashi and M. Iwata, "Morphotropic Phase Boundary in Solid Solution Systems of Perovskite-Type Oxide Ferroelectrics," *Jpn. J. Appl. Phys.*, **37** L985-7 (1998).
- ³⁴J. L. Jones, A. Pramanick, J. C. Nino, S. M. Motahari, E. Üstündag, M. R. Daymond, and E. C. Oliver, "Time-Resolved and Orientation-Dependent Electric-Field-Induced Strains in Lead Zirconate Titanate Ceramics," *Appl. Phys. Lett.*, **90** [17] 172909 (2007).
- ³⁵D. A. Hall, A. Steuwer, B. Cherdhirunkorn, P. J. Withers, and T. Mori, "Micromechanics of Residual Stress and Texture Development due to Poling in Polycrystalline Ferroelectric Ceramics," *J. Mech. Phys. Solids*, **53** [2] 249-60 (2005).
- ³⁶M. Davis, D. Damjanovic, D. Hayem, and N. Setter, "Domain Engineering of the Transverse Piezoelectric Coefficient in Perovskite Ferroelectrics," *J. Appl. Phys.*, **98** [1] 014102 (2005).
- ³⁷H. Fu and R. E. Cohen, "Polarization Rotation Mechanism for Ultrahigh Electromechanical Response in Single-Crystal Piezoelectrics," *Nature*, **403** 281-3 (2000).
- ³⁸Y. Ishibashi and M. Iwata, "Phenomenological Theory of Morphotropic Phase Boundary with Monoclinic Phase in Solid-Solution Systems of Perovskite-Type Oxide Ferroelectrics," *Jpn. J. Appl. Phys.*, **44** [5A] 3095-8 (2005).

- ³⁹A. J. Bell, "Factors Influencing the Piezoelectric Behaviour of PZT and other "Morphotropic Phase Boundary" Ferroelectrics," *J. Mater. Sci.*, **41** 13-25 (2006).
- ⁴⁰M. Budimir, D. Damjanovic, and N. Setter, "Piezoelectric Response and Free-Energy Instability in the Perovskite Crystals BaTiO₃, PbTiO₃, and Pb(Zr,Ti)O₃," *Phys. Rev. B*, **73** [17] 174106 (2006).
- ⁴¹T. J. Boyle, P. G. Clem, B. A. Tuttle, G. L. Brennecke, J. T. Dawley, M. A. Rodriguez, T. D. Dunbar, and W. F. Hammetter, "Lanthanide Series Doping Effects in Lead Zirconate Titanate (PLnZT) Thin Films," *J. Mater. Res.*, **17** [4] 871-8 (2002).
- ⁴²U. Robels and G. Arlt, "Domain Wall Clamping in Ferroelectrics by Orientation of Defects," *J. Appl. Phys.*, **73** 3454 (1993).
- ⁴³J. Lacey and S. Trolier-McKinstry, "Hard and Soft Lead Zirconate Titanate Thin Films Deposited on Flat and Curved Surfaces by Pulsed Laser Deposition," 687-690 in *Proceedings of the Applications of Ferroelectrics, ISAF*, (1996).
- ⁴⁴J. Herbert and A. Moulson, *Electroceramics: Materials, Properties, Applications*. Chapman and Hall, Great Britain, (1993).
- ⁴⁵T. Leist, J. Chen, W. Jo, E. Aulbach, J. Suffner, and J. Rödel, "Temperature Dependence of the Piezoelectric Coefficient in BiMeO₃-PbTiO₃ (Me = Fe, Sc, (Mg_{1/2}Ti_{1/2})) Ceramics," *J. Am. Ceram. Soc.*, **95** [2] 711-5 (2012).
- ⁴⁶K. M. Rittenmyer and P. S. Dubbelday, "Direct Measurement of the Temperature-Dependent Piezoelectric Coefficients of Composite Materials by Laser Doppler Vibrometry," *J. Acoust. Soc. Am.*, **91** [4] 2254-60 (1992).
- ⁴⁷E.-M. Anton, W. Jo, D. Damjanovic, and J. Rödel, "Determination of Depolarization Temperature of (Bi_{1/2}Na_{1/2})TiO₃-Based Lead-Free Piezoceramics," *J. Appl. Phys.*, **110** [9] 094108 (2011).
- ⁴⁸R. E. Eitel, S. J. Zhang, T. R. Shrout, C. A. Randall, and I. Levin, "Phase Diagram of the Perovskite System (1-x)BiScO₃-xPbTiO₃," *J. Appl. Phys.*, **96** [5] 2828-31 (2004).
- ⁴⁹J. L. Jones, "The Use of Diffraction in the Characterization of Piezoelectric Materials," *J. Electroceram.*, **19** [1] 69-81 (2007).
- ⁵⁰J. E. Daniels, J. L. Jones, and T. R. Finlayson, "Characterization of Domain Structures from Diffraction Profiles in Tetragonal Ferroelastic Ceramics," *J. Phys. D: Appl. Phys.*, **39** [24] 5294-9 (2006).

- ⁵¹A. Pramanick, "On the Correlation of Dynamic Electric Field Induced Structural Changes and Piezoelectricity in Ferroelectric Ceramics," Department of Materials Science and Engineering, PhD, University of Florida, Gainesville, (2009).
- ⁵²J. Wang, B. H. Toby, P. L. Lee, L. Ribaud, S. M. Antao, C. Kurtz, M. Ramanathan, R. B. Von Dreele, and M. A. Beno, "A Dedicated Powder Diffraction Beamline at the Advanced Photon Source: Commissioning and Early Operational Results," *Rev. Sci. Instrum.*, **79** [8] 085105 (2008).
- ⁵³A. I. Kingon and S. Srinivasan, "Lead Zirconate Titanate Thin Films Directly on Copper Electrodes for Ferroelectric, Dielectric and Piezoelectric Applications," *Nat. Mater.*, **4** [3] 233-7 (2005).
- ⁵⁴I. I. Naumov, L. Bellaiche, and H. Fu, "Unusual Phase Transitions in Ferroelectric Nanodisks and Nanorods," *Nature*, **432** 737-40 (2004).
- ⁵⁵F. R. Cruickshank, "Ferroelectric Materials and their Applications," *J. Modern Optics*, **39** [5] 1162-3 (1992).
- ⁵⁶I. Grinberg, V. R. Cooper, and A. M. Rappe, "Relationship Between Local Structure and Phase Transitions of a Disordered Solid Solution," *Nature*, **419** 909-11 (2002).
- ⁵⁷H. Jaffe and D. A. Berlincourt, "Piezoelectric Transducer Materials," *Proceedings of the IEEE*, **53** [10] 1372-86 (1965).
- ⁵⁸T. R. Shrout, "Innovations in Piezoelectric Materials for Ultrasound Transducers," 1-4 in *Proceedings of the Applications of Ferroelectrics, 17th IEEE International Symposium, ISAF* (2008).
- ⁵⁹G. H. Haertling and C. E. Land, "Hot-Pressed (Pb,La)(Zr,Ti)O₃ Ferroelectric Ceramics for Electrooptic Applications," *J. Am. Ceram. Soc.*, **54** [1] 1-11 (1971).
- ⁶⁰W. Zhu, I. Fujii, W. Ren, and S. Trolier-McKinstry, "Domain Wall Motion in A and B Site Donor-Doped Pb(Zr_{0.52}Ti_{0.48})O₃ Films," *J. Am. Ceram. Soc.*, **95** [9] 2906-13 (2012).
- ⁶¹D. Viehland, "Effect of Uniaxial Stress upon the Electromechanical Properties of Various Piezoelectric Ceramics and Single Crystals," *J. Am. Ceram. Soc.*, **89** [3] 775-85 (2006).
- ⁶²R.-A. Eichel, "Defect Structure of Oxide Ferroelectrics-Valence State, Site of Incorporation, Mechanisms of Charge Compensation and Internal Bias Fields," *J. Electroceram.*, **19** [1] 11-23 (2007).

- ⁶³J. L. Jones, M. Hoffman, J. E. Daniels, and A. J. Studer, "Direct measurement of the domain switching contribution to the dynamic piezoelectric response in ferroelectric ceramics," *Appl. Phys. Lett.*, **89** [9] 092901 (2006).
- ⁶⁴Y. Saito, H. Takao, T. Tani, T. Nonoyama, K. Takatori, T. Homma, T. Nagaya, and M. Nakamura, "Lead-Free Piezoceramics," *Nature*, **432** 84-87 (2004).
- ⁶⁵D. Damjanovic, "Contributions to the Piezoelectric Effect in Ferroelectric Single Crystals and Ceramics," *J. Am. Ceram. Soc.*, **88** [10] 2663-76 (2005).
- ⁶⁶B. Kim, P. Tong, D. Kwon, J. M. S. Park, and B. G. Kim, "Temperature-Dependent Neutron Diffraction Study of Phase Separation at Morphotropic Phase Boundary in (1-x)BiScO₃-xPbTiO₃," *J. Appl. Phys.*, **105** [11] 114101 (2009).
- ⁶⁷X.-h. Du, J. Zheng, U. Belegundu, and K. Uchino, "Crystal Orientation Dependence of Piezoelectric Properties of Lead Zirconate Titanate near the Morphotropic Phase Boundary," *Appl. Phys. Lett.*, **72** [19] 2421-3 (1998).
- ⁶⁸S. E. Park and T. R. Shrout, "Relaxor Based Ferroelectric Single Crystals for Electro-Mechanical Actuators," *Mater. Res. Innov.*, **1** [1] 20-5 (1997).
- ⁶⁹S.-E. Park and T. R. Shrout, "Ultrahigh Strain and Piezoelectric Behavior in Relaxor Based Ferroelectric Single Crystals," *J. Appl. Phys.*, **82** [4] 1804-11 (1997).
- ⁷⁰E. M. Sabolsky, A. R. James, S. Kwon, S. Trolier-McKinstry, and G. L. Messing, "Piezoelectric Properties of <001> Textured Pb(Mg_{1/3}Nb_{2/3})O₃-PbTiO₃ Ceramics," *Appl. Phys. Lett.*, **78** [17] 2551-3 (2001).
- ⁷¹G. Shirane, K. Suzuki, and A. Takeda, "Phase Transitions in Solid Solutions of Lead Zirconate and Lead titanate (II) X-ray Study," *J. Phys. Soc. Jpn.*, **7** [1] 12-18 (1952).
- ⁷²W. Jiang, R. Zhang, B. Jiang, and W. Cao, "Characterization of Piezoelectric Materials with Large Piezoelectric and Electromechanical Coupling Coefficients," *Ultrasonics*, **41** [2] 55-63 (2003).
- ⁷³B. Noheda, D. E. Cox, G. Shirane, R. Guo, B. Jones, and L. E. Cross, "Stability of the Monoclinic Phase in the Ferroelectric Perovskite PbZr_{1-x}Ti_xO₃," *Phys. Rev. B*, **63** [1] 014103 (2000).
- ⁷⁴S. Li, W. Cao, and L. E. Cross, "The Extrinsic Nature of Nonlinear Behavior Observed in Lead Zirconate Titanate Ferroelectric Ceramic," *J. Appl. Phys.*, **69** [10] 7219-24 (1991).

- ⁷⁵P. Mokřý, M. Kodejška, and J. Václavík, "Recent Trends in Application of Piezoelectric Materials to Vibration Control," in *Recent Advances in Mechatronics*. Springer, Berlin, Germany, 2010, pp. 251-256.
- ⁷⁶A. C. Larson and R. B. von Dreele, "General Structure Analysis System," Los Alamos National Laboratory Report No. LAUR 86-748 (2004).
- ⁷⁷P. Stephens, "Phenomenological Model of Anisotropic Peak Broadening in Powder Diffraction," *J. Appl. Crystallogr.*, **32** [2] 281-9 (1999).
- ⁷⁸R. J. Hill and C. J. Howard, "Quantitative Phase Analysis from Neutron Powder Diffraction Data using the Rietveld Method," *J. Appl. Crystallogr.*, **20** [6] 467-74 (1987).
- ⁷⁹M. Hinterstein, K. A. Schönau, J. Kling, H. Fuess, M. Knapp, H. Kungl, and M. J. Hoffman, "Influence of Lanthanum Doping on the Morphotropic Phase Boundary of Lead Zirconate Titanate," *J. Appl. Phys.* **108** 024110 (2010).
- ⁸⁰D.-J. Kim, J.-P. Maria, A. I. Kingon, and S. K. Streiffer, "Evaluation of Intrinsic and Extrinsic Contributions to the Piezoelectric Properties of $\text{Pb}(\text{Zr}_{1-x}\text{T}_x)\text{O}_3$ Thin Films as a Function of Composition," *J. Appl. Phys.*, **93** [9] 5568-75 (2003).
- ⁸¹D. A. Berlincourt, C. Cmolik, and H. Jaffe, "Piezoelectric Properties of Polycrystalline Lead Titanate Zirconate Compositions," *Proc. IRE*, **48** [2] 220-9 (1960).
- ⁸²S. Iakovlev, C.-H. Solterbeck, and M. Es-Souni, "Doping and Thickness Effects on Dielectric properties and Subswitching Behavior of Lead Titanate thin films," *Appl. Phys. Lett.*, **81** [10] 1854-6 (2002).
- ⁸³G. Adachi, N. Imanaka, Z. C. Kang (eds.) *Binary Rare Earth Oxides*. Kluwer Academic Publishers, Dordrecht, The Netherlands, 2004.
- ⁸⁴X. Ren, "Large Electric-Field-Induced Strain in Ferroelectric Crystals by Point-Defect-Mediated Reversible Domain Switching," *Nat. Mater.*, **3** [2] 91-4 (2004).
- ⁸⁵J. Y. Li, R. C. Rogan, E. Üstündag, and K. Bhattacharya, "Domain Switching in Polycrystalline Ferroelectric Ceramics," *Nat. Mater.*, **4** [10] 776-81 (2005).
- ⁸⁶R. D. Shannon and C. T. Prewitt, "Effective Ionic Radii in Oxides and Fluorides," *Acta Crystallogr. B*, **25** [5] 925-46 (1969).
- ⁸⁷G. Burns and B. A. Scott, "Raman Studies of Underdamped Soft Modes in PbTiO_3 ," *Phys. Rev. Lett.*, **25** [3] 167-70 (1970).

- ⁸⁸Z. Wu and R. E. Cohen, "Pressure-Induced Anomalous Phase Transitions and Colossal Enhancement of Piezoelectricity in PbTiO_3 ," *Phys. Rev. Lett.*, **95** [3] 037601 (2005).
- ⁸⁹R. J. Zeches, M. D. Rossell, J. X. Zhang, A. J. Hatt, Q. He, C.-H. Yang, A. Kumar, C. H. Wang, A. Melville, C. Adamo, G. Sheng, Y.-H. Chu, J. F. Ihlefeld, R. Erni, C. Ederer, V. Gopalan, L. Q. Chen, D. G. Schlom, N. A. Spaldin, L. W. Martin, and R. Ramesh, "A Strain-Driven Morphotropic Phase Boundary in BiFeO_3 ," *Science*, **326** 977-80 (2009).
- ⁹⁰J. Zhu, F. Liu, G. B. Stringfellow, and S.-H. Wei, "Strain-Enhanced Doping in Semiconductors: Effects of Dopant Size and Charge State," *Phys. Rev. Lett.*, **105** [19] 195503 (2012).
- ⁹¹W. Cao and L. E. Cross, "Theory of Tetragonal Twin Structures in Ferroelectric Perovskites with a First-Order Phase Transition," *Phys. Rev. B*, **44** [1] 5-12 (1991).
- ⁹²J. L. Jones, E. B. Slamovich, and K. J. Bowman, "Domain Texture Distributions in Tetragonal Lead Zirconate Titanate by X-ray and Neutron Diffraction," *J. Appl. Phys.*, **97** 034113 (2005).
- ⁹³A. Pramanick, A. D. Prewitt, M. A. Cottrell, W. Lee, A. J. Studer, K. An, C. R. Hubbard, and J. L. Jones, "*In Situ* Neutron Diffraction Studies of a Commercial, Soft Lead Zirconate Titanate Ceramic: Response to Electric Fields and Mechanical Stress," *Appl. Phys. A* **99** [3] 557-64 (2010).

BIOGRAPHICAL SKETCH

Shruti Banavara Seshadri earned a Bachelor of Engineering degree in Chemical Engineering from Rashtreeya Vidyalaya College of Engineering and MS and PhD degrees in Materials Science and Engineering from the University of Florida. Prior to starting her PhD work, Shruti studied the kinesin-microtubule self-assembly system with Prof. Henry Hess at the University of Florida. She also researched the synthesis of gold nanoparticles and the quantification of order in nanoparticle arrays with Prof. Venugopal Santhanam at the Indian Institute of Science. She was the 2009 USA winner of the Institute of Materials Minerals and Mining Young Person's Lecture Competition for her talk "Lessons from nature: making materials by self-assembly". Shruti won the Alec Courtelis Award in 2012 for academic excellence and contributions to the Department of Materials Science and Engineering. The scientific publications that have influenced Shruti the most are *The Origin of Species* by Charles Darwin and A. Raj, A. van Oudenaarden, "Nature, Nurture, or Chance: Stochastic Gene Expression and Its Consequences," *Cell*, **135**[2] 216-226.2008.